

# P-model v1.0: An optimality-based light use efficiency model for simulating ecosystem gross primary production

Benjamin D. Stocker<sup>1,2,3</sup>, Han Wang<sup>4</sup>, Nicholas G. Smith<sup>5</sup>, Sandy P. Harrison<sup>6</sup>, Trevor F. Keenan<sup>7,8</sup>, David Sandoval<sup>9</sup>, Tyler Davis<sup>9,10</sup>, and I. Colin Prentice<sup>9</sup>

<sup>1</sup>CREAF, Campus UAB, 08193 Bellaterra, Catalonia, Spain

<sup>2</sup>Earth System Science, Stanford University, Stanford, 94305-4216, California, USA

<sup>3</sup>Institute of Agricultural Sciences, Department of Environmental Systems Science, ETH, Universitätsstrasse 2, 8092 Zürich, Switzerland

<sup>4</sup>Department of Earth System Science, Tsinghua University, Haidian, Beijing, 100084, China

<sup>5</sup>Department of Biological Sciences, Texas Tech University, Box 43131 Lubbock, TX 79409, USA

<sup>6</sup>Geography and Environmental Science, Reading University, Reading, RG6 6 AH, UK

<sup>7</sup>Earth and Environmental Sciences Area, Lawrence Berkeley National Lab, Berkeley, CA 94709, USA

<sup>8</sup>Department of Environmental Science, Policy and Management, UC Berkeley, Berkeley, CA 94720, USA

<sup>9</sup>AXA Chair of Biosphere and Climate Impacts, Department of Life Sciences, Imperial College London, Silwood Park Campus, Ascot, Berkshire, SL5 7PY, UK

<sup>10</sup>Center for Geospatial Analysis, The College of William & Mary, Williamsburg, VA, 23185, USA.

**Correspondence:** B. D. Stocker (bestocke@ethz.ch)

## Abstract.

Terrestrial photosynthesis is the basis for vegetation growth and drives the land carbon cycle. Accurately simulating gross primary production (GPP, ecosystem-level apparent photosynthesis) is key for satellite monitoring and Earth System Model predictions under climate change. While robust models exist for describing leaf-level photosynthesis, predictions diverge due to uncertain photosynthetic traits and parameters which vary on multiple spatial and temporal scales. Here, we describe and evaluate a gross primary production (GPP, photosynthesis per unit ground area) model, the P-model, that combines the Farquhar-von Caemmerer-Berry model for  $C_3$  photosynthesis with an optimality principle for the carbon assimilation-transpiration trade-off, and predicts a multi-day average light use efficiency (LUE) for any climate and  $C_3$  vegetation type. The model builds on the theory developed in Prentice et al. (2014) and Wang et al. (2017a) and is extended to include low temperature effects on the intrinsic quantum yield and an empirical soil moisture stress factor. The model is forced with site-level data of the fraction of absorbed photosynthetically active radiation (fAPAR) and meteorological data and is evaluated against GPP estimates from a globally distributed network of ecosystem flux measurements. Although the P-model requires relatively few inputs, the  $R^2$  for predicted versus observed GPP based on the full model setup is 0.75 (8-day mean, 126 sites) – similar as comparable satellite data-driven GPP models but without predefined vegetation type-specific parameters. The  $R^2$  is reduced to 0.70 when not accounting for the reduction in quantum yield at low temperatures and effects of low soil moisture on LUE. The  $R^2$  for the P-model-predicted LUE is 0.32 (means by site) and 0.48 (means by vegetation type). Applying this model for global-scale simulations yields a total global GPP of 106-122 GtC yr<sup>-1</sup> (mean of 2001-2011), depending on the fAPAR forcing data. The

P-model provides a simple but powerful method for predicting – rather than prescribing – light use efficiency and simulating terrestrial photosynthesis across a wide range of conditions. The model is available as an R package (*rpmodel*).

20 Copyright statement.

## 1 Introduction

Realistic, reliable and robust estimates of terrestrial photosynthesis are required to understand variations in the carbon cycle, monitor forest and cropland productivity, and predict impacts of global environmental change on ecosystem function (Prentice et al., 2015). Understanding how photosynthetic rates depend on temperature, humidity, solar radiation, CO<sub>2</sub> and soil moisture is at the core of this challenge. Process-based Dynamic Vegetation Models (DVMs) and Earth System Models (ESMs) in use today almost always use some form of the Farquhar-von Caemmerer-Berry (FvCB) model for C<sub>3</sub> photosynthesis (Farquhar et al., 1980; von Caemmerer and Farquhar, 1981), in combination with stomatal conductance ( $g_s$ ) models (Ball et al., 1987; Leuning, 1995; Medlyn et al., 2011), that couple water and carbon fluxes at the leaf surface.

The FvCB model describes the instantaneous saturating relationship between leaf-internal CO<sub>2</sub> concentrations ( $c_i$ ) and assimilation ( $A$ ), and how this relationship depends on absorbed photosynthetically active radiation (APAR). It simulates  $A$  as the minimum of a light-limited and a Rubisco-limited assimilation rate,  $A_J$  and  $A_C$  respectively:

$$A = \min(A_J, A_C) \quad (1)$$

Although the FvCB model is standard for leaf-scale photosynthesis, and its environmental responses at time scales of minutes to hours, DVMs and ESMs using FvCB produce divergent results for ecosystem-level fluxes and their response to environment at longer time scales (Rogers et al., 2017). This is due to assumptions that have to be made about photosynthetic parameters that are not predicted by the FvCB model: stomatal conductance ( $g_s$ ) and the maximum rates of Rubisco carboxylation ( $V_{\text{cmax}}$ ) and electron transport ( $J_{\text{max}}$ ) for ribulose-1,5-bisphosphate (RuBP) regeneration, which together determine the relationship between  $c_i$  and  $A$ . Common approaches for determining the values of  $V_{\text{cmax}}$  and  $J_{\text{max}}$  in DVMs and ESMs are to prescribe fixed values per plant functional type (PFT) and attempt to simulate the distribution of PFTs in space, or to use empirical relationships between leaf N and  $V_{\text{cmax}}$  and simulate leaf N internally or prescribe it per PFT (Smith and Dukes, 2013; Rogers, 2014).

While the FvCB model describes a non-linear relationship between instantaneous assimilation and absorbed light, ecosystem production, integrated over weeks to months, scales proportionally with absorbed photosynthetically active radiation (APAR) (Monteith, 1972; Medlyn, 1998). This observation underlies the general light use efficiency (LUE) model which describes ecosystem-level photosynthesis (gross primary production, GPP) as the product of APAR and LUE:

$$\text{GPP} = \text{PAR} \cdot f\text{APAR} \cdot \text{LUE} , \quad (2)$$

where PAR is the incident photosynthetically active radiation and fAPAR is the fraction of PAR that is absorbed by green tissue. The LUE model is the basis for observation-driven GPP models that use fAPAR and PAR based on remote sensing data and combine this with different approaches for simulating LUE (Running et al., 2004; Zhang et al., 2017a; Field et al., 1995), and for some forest growth models (Landsberg and Waring, 1997). Other remote sensing data-based models (Jiang and Ryu, 2016) apply the FvCB model in combination with vegetation cover and type data and prescribed  $V_{\text{cmax}}$  for a set of PFTs.

Here, we describe a model, referred to as the *P-model*, that unifies the FvCB and LUE models following the theory developed by Prentice et al. (2014) and Wang et al. (2017a). The model assumes an optimality principle that balances the C cost (per unit of assimilation) of maintaining transpiration and carboxylation ( $V_{\text{cmax}}$ ) capacities. It thus predicts how the ratio of leaf-internal to ambient  $\text{CO}_2$  ( $c_i : c_a = \chi$ ) acclimates to the environment, given temperature ( $T$ ), water vapour pressure deficit ( $D$ ), atmospheric pressure ( $p$ ) and ambient  $\text{CO}_2$  concentration ( $c_a$ ) (Prentice et al., 2014). The P-model also assumes that the photosynthetic machinery tends to coordinate  $V_{\text{cmax}}$  and  $J_{\text{max}}$  in order to operate close to the intersection of the light-limited and Rubisco-limited assimilation rates (*Coordination Hypothesis*, Chen et al. (1993); Maire et al. (2012)) under mean daytime environmental conditions. By further assuming equality in the marginal cost and benefit of  $J_{\text{max}}$ , daily-to-monthly average assimilation rates can then be described as fractions of absorbed PAR, i.e. as a LUE model (Eq. 2) (Wang et al., 2017a).

Thus, the P-model embodies an optimality-based theory for predicting the acclimation of leaf-level photosynthesis to its environment and for simulating LUE. In combination with prescribed PAR and remotely sensed fAPAR, it estimates GPP across diverse environmental conditions (Wang et al., 2017a). Its prediction for acclimating photosynthetic parameters reduces the number of prescribed (and temporally fixed) values and avoids the distinction of model parameterisation by vegetation types or biomes (apart from a distinction between the  $\text{C}_3$  and  $\text{C}_4$  photosynthetic pathways). The P-model has a further advantage over other data-driven GPP models ((Running et al., 2004; Zhang et al., 2017a), and empirically upscaled GPP estimates (Jung et al., 2011) in that it accounts for the influence of changing  $\text{CO}_2$ , and that it uses first principles (rather than imposed functions) to represent effects of  $T$ ,  $D$  and  $p$  (Sect. 2). The theory underlying the P-model regarding the water-carbon tradeoff has been described by Prentice et al. (2014) and applied by Keenan et al. (2017) to simulate how changes in primary production have driven the terrestrial C sink over past decades; and by Smith et al. (2019) to explain variations in observed  $V_{\text{cmax}}$ . Wang et al. (2017a) complemented the theory by including effects of limited electron transport capacity ( $J_{\text{max}}$ ) and predicted variations in observed  $\chi$  across environmental gradients. To resolve model biases under conditions of low soil moisture, (Stocker et al., 2019) further applied an empirical stress function to reduce LUE under dry soil conditions.

The purpose of this paper is (i) to provide a full documentation of the model implementation and reference for open-source software (*rpmodel* R package, available on CRAN); (ii) to provide an evaluation of model-predicted LUE and GPP against GPP derived from eddy covariance flux measurements (FLUXNET 2015 Tier 1 dataset); (iii) to apply this model for global-scale simulations and compare spatial patterns and global totals of simulated GPP with other estimates with global coverage; and (iv) to introduce a robust and pragmatic solution to resolving model bias under dry and cold conditions. With (iv) we do not aim at extending the theoretical basis for the P-model (Prentice et al., 2014; Wang et al., 2017a), but to include environmental controls in the LUE model that serve to make the model applicable as a remote sensing data-driven GPP model for a wide range of conditions and vegetation types. The evaluation focuses on different components of variability (spatial, annual, seasonal,

daily anomalies) (Secs. 4.6 - 4.2). We further address uncertainties associated with the fAPAR forcing (Sect. 4.4) and the uncertainties in the evaluation data by using GPP data derived from different flux decomposition methods (Sect. 4.5). The use of continuous GPP measurements, rather than experimentally disturbed measurements, makes it challenging to assess modelled GPP under extreme environmental conditions. We therefore make a further evaluation of simulated GPP during the course of soil moisture drought events (*fLUE droughts*, Sect. 4.3).

## 2 Theory

The theory underlying the P-model has been described by Wang et al. (2017a) and the derivation of equations is given therein. It is presented here again for completeness.

### 2.1 Balancing carbon and water costs

The P-model centres around a prediction for the optimal ratio of leaf-internal to ambient CO<sub>2</sub> concentration  $c_i : c_a$  (termed  $\chi$ ) that balances the costs associated with maintaining the transpiration stream and the cost of maintaining a given carboxylation capacity. The optimal balance is achieved when the two marginal costs are equal:

$$a \frac{\partial(E/A)}{\partial\chi} = -b \frac{\partial(V_{\text{cmax}}/A)}{\partial\chi} . \quad (3)$$

Here,  $a$  and  $b$  are the respective unit costs.  $b$  is assumed to be constant, and  $a$  to scale linearly with the temperature-dependent viscosity of water  $\eta(T)$ , calculated following Huber et al. (2009). Below, we introduce  $\beta = b/a'$ , with  $a = \eta^* a'$  and  $\eta^* = \eta(T)/\eta(25^\circ\text{C})$ . The optimal  $\chi$  solves the above equation. We use Fick's law (Fick, 1855) to express transpiration and assimilation as a function of stomatal conductance  $g_s$ :

$$E = 1.6g_s D \quad (4)$$

and

$$A = g_s c_a (1 - \chi) , \quad (5)$$

and use the Rubisco-limited assimilation rate from the FvCB model:

$$A = A_C = V_{\text{cmax}} m_C , \quad (6)$$

with

$$m_C = \frac{c_i - \Gamma^*}{c_i + K} , \quad (7)$$

where  $c_i$  is given by  $c_a \chi$ .  $K$  is the effective Michaelis-Menten coefficient for Rubisco-limited assimilation (Sect. B3), and  $\Gamma^*$  is the photorespiratory compensation point in the absence of dark respiration (Sect. B1). The optimal  $\chi$  can be derived as

$$\chi = \frac{\Gamma^*}{c_a} + \left(1 - \frac{\Gamma^*}{c_a}\right) \frac{\xi}{\xi + \sqrt{D}} , \quad (8)$$

with

$$110 \quad \xi = \sqrt{\frac{\beta(K + \Gamma^*)}{1.6\eta^*}} . \quad (9)$$

(See Appendix F1 for intermediate steps.) Because both terms in Eq. 3 are divided by  $A$ , the solution is independent of whether the Rubisco-limited rate  $A_C$  or the light-limited rate  $A_J$  (see below) are followed. With this prediction for  $\chi$ , we can use the *Coordination Hypothesis* (Chen et al., 1993; Haxeltine and Prentice, 1996; Maire et al., 2012) and the light-limited assimilation rate from the FvCB model to write

$$115 \quad A_J = \varphi_0 I_{\text{abs}} m , \quad (10)$$

with

$$m = \frac{c_i - \Gamma^*}{c_i + 2\Gamma^*} . \quad (11)$$

$I_{\text{abs}}$  is the amount of absorbed light and  $\varphi_0$  is the intrinsic quantum yield efficiency. This equation has the form of a LUE model (Eq. 2) in that  $A_J$  scales linearly with  $I_{\text{abs}}$ . Using Eqs. 9 and 8,  $m$  can be expressed directly as

$$120 \quad m = \frac{c_a - \Gamma^*}{c_a + 2\Gamma^* + 3\Gamma^* \sqrt{\frac{1.6\eta^* D}{\beta(K + \Gamma^*)}}} . \quad (12)$$

The unit cost ratio  $\beta$  has been estimated by Wang et al. (2017a) to 240 based on global leaf  $\delta^{13}\text{C}$  data and a simplified version of the P-model (assuming  $\Gamma^* = 0$  and neglecting the  $J_{\text{max}}$  limitation). Here, we re-estimated  $\beta$  to 146 based on the full version of the model using the same global leaf  $\delta^{13}\text{C}$  dataset. This is more strictly consistent with the model formulation implemented here. The value for  $\beta$  used here is 146.0 (unitless). Eq. 12 provides the basis for predicting  $\text{CO}_2$  assimilation rates in the form of a LUE model (Eq. 2) where LUE is a function of  $T$  and  $p$  (both affecting  $\Gamma^*$ ,  $K$ , and  $\eta^*$ ; see Secs. B1 and B3),  $D$ , and  $c_a$ .

The prediction of optimal  $\chi$  has a number of corollaries (see Appendix C). An estimate for stomatal conductance ( $g_s$ ) and the intrinsic water use efficiency ( $\text{iWUE} = A/g_s$ ) directly follow from the optimal water-carbon balance (Eq. 3). By assuming  $A_J = A_C$ , we can further derive  $V_{\text{cmax}}$ , as well as dark respiration ( $R_d$ ), which is a function of  $V_{\text{cmax}}$  (see Secs. C3 and C4).

## 2.2 Introducing $J_{\text{max}}$ limitation

130 Eq. 10 assumes that the light response of  $A$  is linear up to the coordination point. In reality, rates saturate towards high light levels because the electron transport rate  $J$ , necessary for the regeneration of ribulose-1,5,- biphosphate (RuBP) tends towards a maximum  $J_{\text{max}}$ . To account for this effect, Eq. 10 can be modified, following the formulation by Smith (1937), using a non-rectangular hyperbola relationship between  $A_J$  and  $I_{\text{abs}}$  to allow for the effect of finite  $J_{\text{max}}$ :

$$A_J = \varphi_0 I_{\text{abs}} m \underbrace{\frac{1}{\sqrt{1 + \left( \frac{4 \varphi_0 I_{\text{abs}}}{J_{\text{max}}} \right)^2}}}_L \quad (13)$$

135 In this equation  $A_J$  is no longer linear with respect to  $I_{\text{abs}}$  and thus does not have the form of a LUE model. However,  $J_{\text{max}}$  is assumed here to acclimate on longer time scales to  $I_{\text{abs}}$ , so that the marginal gain in assimilation  $A$  per unit change in  $J_{\text{max}}$  is equal to the unit cost ( $c$ ) of maintaining  $J_{\text{max}}$ .

$$\frac{\partial A}{\partial J_{\text{max}}} = c \quad (14)$$

The unit cost  $c$  is assumed to include the maintenance of light-harvesting complexes and various proteins involved in the electron transport chain. The cost of maintaining a given  $J_{\text{max}}$  is thus assumed to scale linearly with  $J_{\text{max}}$  and that this proportionality is constant ( $c$  is constant). By taking the derivative of Eq. 13 with respect to  $J_{\text{max}}$  and re-arranging terms (see Appendix F2 for intermediate steps), we obtain the  $J_{\text{max}}$  limitation factor  $L$  in Eq. 13 as:

$$L = \sqrt{1 - \left(\frac{c^*}{m}\right)^{2/3}}, \quad (15)$$

with  $c^* = 4c$ . Note that  $L$  is independent of  $I_{\text{abs}}$ . Hence,  $A_J$  is again a linear function of absorbed light. The cost factor  $c^*$  is estimated from published values of  $J_{\text{max}}:V_{\text{cmax}} = 1.88$  at 25°C. (Kattge and Knorr, 2007) and  $\chi = 0.8$  (Lloyd and Farquhar, 1994) at  $c^* = 0.41$  (Wang et al., 2017a). The revised LUE model thus becomes

$$A = \varphi_0 I_{\text{abs}} m', \quad (16)$$

with

$$m' = m \sqrt{1 - \left(\frac{c^*}{m}\right)^{2/3}}. \quad (17)$$

150 Wang et al (2017a) showed that this formulation of  $J_{\text{max}}$  costs leads to a realistic dependence of the  $J_{\text{max}}:V_{\text{cmax}}$  ratio on growth temperature.

As shown by Smith et al. (2019), an alternative approach can be used to introduce the effects of  $J_{\text{max}}$  limitation, replacing Eq. 13 by the more widely used one-parameter family of saturation curves following Farquhar and Wong (1984). This alternative is described in Appendix F3 and implemented as an optional method in the R package *rpmodel*.

## 155 3 Methods

### 3.1 The light use efficiency model

$A$  is commonly expressed in  $\text{mol m}^{-2} \text{s}^{-1}$ . For further model description and evaluation, we refer to ecosystem-scale quantities in mass units of assimilated C and model GPP ( $\text{g C m}^{-2} \text{d}^{-1}$ ) following Eq. 2 with

$$\text{fAPAR} \cdot \text{PPFD} \triangleq I_{\text{abs}} \quad (18)$$

$$160 \quad \text{LUE} \triangleq \varphi_0(T) \beta(\theta) m' M_C \quad (19)$$

Here,  $M_C$  is the molar mass of carbon (12.0107 g mol<sup>-1</sup>) to convert from molar units to mass units, and PPFD is the photosynthetic photon flux density per square metre, integrated over a day (mol m<sup>-2</sup> d<sup>-1</sup>). fAPAR is unitless and integrates across the canopy, i.e., from fluxes per unit leaf area to fluxes per unit ground area. LUE is in units of g C mol<sup>-1</sup>. The intrinsic quantum yield parameter  $\varphi_0$  is modelled as temperature-dependent, and an additional (unitless) empirical soil moisture stress factor  $\beta(\theta)$  is included for modelling LUE.

### 3.1.1 Temperature dependence of the intrinsic quantum yield of photosynthesis

The temperature dependence of the intrinsic quantum yield ( $\varphi_0(T)$ , mol mol<sup>-1</sup>) is modelled following the temperature dependence of the maximum quantum yield of photosystem II in light-adapted leaves, determined by Bernacchi et al. (2003) as

$$\varphi_0(T) = \frac{a_L b_L}{4} (0.352 + 0.022 T - 0.00034 T^2) \quad (20)$$

where  $a_L$  is the leaf absorptance, and  $b_L$  is the fraction of absorbed light that reaches photosystem II. The factor 1/4 is introduced here as the equation given by Bernacchi et al. (2003) applies to electron transport rather than C assimilation. Here,  $(a_L b_L / 4)$  is treated as a single calibratable parameter (see Section 3.3) and is henceforth referred to as  $\widehat{c}_L \equiv a_L b_L / 4$ . (All calibratable parameters are thereafter indicated by a hat over the symbol.) This temperature dependence was not accounted for in earlier P-model publications (Keenan et al., 2017; Wang et al., 2017a). To test the effect of this temperature dependence on simulated GPP, we conducted alternative simulations, where a constant  $\widehat{\varphi}_0$  was calibrated instead (Sect. 3.2). Note, that  $\varphi_0$  includes the factor  $a_L$  for incomplete leaf absorptance, which is commonly quantified separately from the quantum yield efficiency. In other vegetation models,  $a_L$  is commonly ascribed a value of 0.72-0.88 (Rogers et al., 2017). Values of  $\varphi_0$  used here are accordingly lower than values for the intrinsic quantum yield reported from experimental studies (Long et al., 1993; Singaas et al., 2001). Furthermore, within-canopy reflection and reabsorption mean that leaf-level absorptance is not equivalent to canopy-level absorptance, thus  $\varphi_0$  should be regarded as canopy-scale *effective* value of intrinsic quantum yield. It is treated here as a calibratable parameter, which may vary according to the fAPAR forcing data set used.

### 3.1.2 Soil moisture stress

$\beta(\theta)$  is an empirical soil moisture stress function. We use results by Stocker et al. (2018) to fit this function based on two general patterns. First, the functional form of  $\beta(\theta)$  is approximated by a quadratic expression that approaches 1 for soil moisture above a certain threshold  $\theta^*$  and held constant at 1 for soil moisture values above this threshold. Here  $\theta$  is the plant-available soil water, expressed as a fraction of available water holding capacity, and  $\theta^*$  is set to 0.6. The general form is:

$$\beta = \begin{cases} q(\theta - \theta^*)^2 + 1, & \theta \leq \theta^* \\ 1, & \theta > \theta^* \end{cases} \quad (21)$$

Second, the sensitivity of  $\beta(\theta)$  to extreme soil dryness ( $\theta \rightarrow 0$ ) is related to the mean aridity, quantified as the mean annual ratio of actual over potential evapotranspiration (AET/PET) (Stocker et al., 2018). The decline in  $\beta(\theta)$  with drying soils is

steep in dry climates and less steep in less dry climates. In equation 21, the sensitivity parameter  $q$  is defined by the maximum  $\beta$  reduction at low soil moisture  $\beta_0 \equiv \beta(\theta = \theta_0)$ , leading to  $q = (\beta_0 - 1)/(\theta^* - \theta_0)^2$ . Note that  $q$  has a negative value.  $\beta_0$  is modelled as a linear function of the mean aridity, :

$$\beta_0 = \hat{a}_\theta + \hat{b}_\theta(\text{AET}/\text{PET}) \quad (22)$$

195  $\hat{a}_\theta$  and  $\hat{b}_\theta$  are treated as calibratable parameters.

Soil moisture ( $\theta$ ), AET, and PET are simulated using the SPLASH model (Davis et al., 2017), which treats soil water storage as a single bucket and calculates potential evapotranspiration based on Priestley and Taylor (1972). The only difference to the model version described by (Davis et al., 2017) is that we account here for a variable water holding capacity calculated based on soil texture and depth data from SoilGrids (Hengl et al., 2014). A detailed description of the applied empirical functions for  
200 calculating plant-available water holding capacity from texture data is given in Appendix D.

## 3.2 Simulation protocol

### 3.2.1 Site-scale simulations

We conducted multiple sets of site-scale simulations (Tab. 1) to investigate the dependence of model performance on alternative model setups (variable/fixed soil moisture and temperature effects), alternative choices of forcing data (fAPAR), and  
205 alternative observational target data for calibration (GPP based on different flux decompositions). Parameters ( $\hat{c}_L$ ,  $\hat{a}_\theta$ , and  $\hat{b}_\theta$ ) were calibrated and evaluated against the appropriate observational data for each set of simulations separately.

The setup ORG is the P-model in its original form, as described in Wang et al. (2017a). It uses a fixed quantum efficiency of photosynthesis ( $\hat{\varphi}_0$  is calibrated, instead of  $\hat{c}_L$ ), and does not account for soil moisture stress ( $\beta(\theta) = 1$ ). Here, the model is forced with fAPAR data based on MODIS FPAR (MCD15A3H), linearly interpolated 4-daily values to daily values (see  
210 Section 3.4.1), and is calibrated against GPP data from FLUXNET 2015 based on the nighttime partitioning method (NT) (see Section 3.5.1). The simulation set BRC ('Bernacchi') is identical to ORG except that  $\hat{\varphi}_0$  is allowed to vary with temperature following Bernacchi et al. (2003) and Eq. 20, and  $\hat{c}_L$  is calibrated. The full P-model setup (FULL) includes the soil moisture stress function described above, and  $\hat{c}_L$ ,  $\hat{a}_\theta$ , and  $\hat{b}_\theta$  are calibrated simultaneously.

All additional simulations account for both temperature and soil moisture effects. The simulation set FULL\_FPARitp also  
215 uses MODIS FPAR data for fAPAR, but applies a spline to get daily values. This is to evaluate alternative interpolation methods. The simulation set FULL\_EVI uses MODIS EVI (MOD13Q1), interpolated to daily from 8-daily data, to assess to which the degree the model performance depends on the fAPAR forcing data source. See Section 3.4.1 for more information.

All site-scale simulations were calibrated against GPP data (Sec. 3.3), calculated using the nighttime flux decomposition method (Reichstein et al., 2005). Additional simulation sets FULL\_DT, FULL\_NTsub, and FULL\_Ty were used to investigate  
220 the dependence of model performance on the choice of observational data used for calibration. We used GPP data based on the nighttime decomposition method (Reichstein et al., 2005) for FULL\_NTsub, the daytime decomposition method (Lasslop et al., 2010) for FULL\_DT, and an alternative decomposition method, previously used in Wang et al. (2017a), for FULL\_Ty.



**Table 1.** Model setups. The standard fAPAR data is MODIS FPAR MCD15A3H, where the original data, given at 4-day intervals, is splined to daily values (‘spl.’). Alternative greenness forcing data are based on MODIS EVI MOD13Q1, splined from 8-day intervals to daily, and MODIS FPAR MCD15A3H, linearly interpolated (‘itpl.’) from 4-day intervals to daily. Standard observational GPP data, used for model calibration and evaluation, are from FLUXNET 2015, based on the nighttime flux decomposition method (‘NT’ in the table, variable GPP\_NT\_VUT\_REF in FLUXNET 2015). Alternative GPP data used based on the daytime flux decomposition method (‘DT’ in the table, variable GPP\_DT\_VUT\_REF), and based on an alternative method (Wang et al., 2017a) (‘Ty’ in the table). For setups ORG, BRC, FULL, FULL\_FPARitp, and FULL\_EVI, data used for the model calibration is from all dates where NT data are available. For setups FULL\_DT, FULL\_Ty, and FULL\_NTsub, calibration data are from all dates where data is available for all three methods DT, NT, and Ty. Column  $\varphi_0(T)$  specifies whether the temperature dependence of intrinsic quantum yield is included. Column  $\beta(\theta)$  specifies whether soil moisture stress is included. Columns  $\widehat{\varphi}_0$ ,  $\widehat{c}_L$ ,  $\widehat{a}_\theta$  and  $\widehat{b}_\theta$  provide the calibrated parameter values in each simulation set.

Setup name	fAPAR data	GPP	Calibration set	$\varphi_0(T)$	$\beta(\theta)$	$\widehat{\varphi}_0$	$\widehat{c}_L$	$\widehat{a}_\theta$	$\widehat{b}_\theta$
ORG	FPAR MCD15A3H, spl.	NT	NT data	no	no	0.04998	–	–	–
BRC	FPAR MCD15A3H, spl.	NT	NT data	yes	no	–	0.08179	–	–
FULL	FPAR MCD15A3H, spl.	NT	NT data	yes	yes	–	0.08718	0	0.73300
NULL	FPAR MCD15A3H, spl.	NT	NT data	no	no	0.2475*	–	–	–
FULL_FPARitp	FPAR MCD15A3H, itpl.	NT	NT data	yes	yes	–	0.08486	0.0	0.74704
FULL_EVI	EVI MOD13Q1, spl.	NT	NT data	yes	yes	–	0.13136	0.01000	0.78419
FULL_DT	FPAR MCD15A3H, spl.	DT	NT, DT, Ty	yes	yes	–	0.08604	0.0	0.72735
FULL_Ty	FPAR MCD15A3H, spl.	Ty	NT, DT, Ty	yes	yes	–	0.08701	0.10671	0.68802
FULL_NTsub	FPAR MCD15A3H, spl.	NT	NT, DT, Ty	yes	yes	–	0.08719	0.0	0.73334

\*The value represents the fitted LUE, corresponding to  $(\varphi_0 m' M_C)$  in Eq. 19.

The Ty method estimates a constant monthly background respiration rate fitted to match net ecosystem exchange fluxes of CO<sub>2</sub> from measurements assuming a linear or saturating dependence of GPP on PPFD. Calibration and evaluation of FULL\_DT, FULL\_NTsub, and FULL\_Ty are done only for sites and dates where observational data is available for all three datasets (DT, NT, and Ty), hence the distinction between FULL\_NTsub and FULL.

### 3.2.2 Global simulations

Global simulations were conducted for the setup FULL, using the respectively calibrated parameters from the site-scale simulations. All vegetation is assumed to follow the C<sub>3</sub> photosynthetic pathway and we do not distinguish between croplands and other vegetation. We conducted two simulations with alternative fAPAR forcing data. These are described in Section 3.4.

### 3.3 Model calibration

Calibration was performed only for the model parameters determining the quantum efficiency of photosynthesis ( $\widehat{\varphi}_0$  or  $\widehat{c}_L$ , respectively) and the dependence of the sensitivity of the soil moisture stress function on average aridity (parameters  $\widehat{a}_\theta$  and  $\widehat{b}_\theta$ ). Simulated GPP was calibrated to minimise the root mean square error (RMSE) compared to observed daily GPP (Sect. 3.5). We used Generalised Simulated Annealing from the *GenSA* R package (Yang Xiang et al., 2013) to calibrate model parameters. This algorithm is particularly suited to find global minima of non-linear objective functions in situations where there can be a large number of local minima. To test the robustness of the calibration and evaluation metrics, we additionally performed out-of-sample calibrations for the FULL setup where the training set included data from all but one site. The test dataset, used to calculate  $R^2$  and RMSE, contained only data from that single left-out site.

### 3.4 Forcing data

Unstressed light use efficiency,  $m'$  in Eq. 19, is simulated using monthly mean values for daytime  $T$  and  $D$ ; temporally constant site-specific elevation (used to calculate atmospheric pressure, scaled from sea-level standard pressure of 101325 Pa); and annually varying observed atmospheric  $\text{CO}_2$  (MacFarling Meure et al., 2006), identical across sites. The choice of aggregating to monthly mean values is motivated by the time scale of Rubisco turnover, which limits the rate at which photosynthetic parameters can acclimate to changing environmental conditions (McNevin et al., 2006).

Predicted monthly LUE ( $m'$ ) is multiplied by daily varying  $I_{\text{abs}}$ , and response functions  $\varphi_0(T)$  and  $\beta(\theta)$ , driven by daily varying temperature and soil moisture. This choice is motivated by the known rapid response in stomatal conductance to drying soils (represented by  $\beta(\theta)$ ), and the instantaneous temperature response of the quantum yield efficiency ( $\varphi_0(T)$ ). Simulating GPP as the product of LUE and daily varying PPFD would not be consistent with the non-linear instantaneous response of  $A$  to light (Eq. 10) given the acclimation time scale of photosynthesis ((Suzuki et al., 2001; Maire et al., 2012). We therefore evaluate simulated GPP averaged over 8-day periods. The choice of appropriate model prediction and evaluation time scales is further discussed in Sect. 5.

#### 3.4.1 fAPAR

For site-scale simulations, we used three alternative datasets as model forcing for fAPAR (MODIS FPAR splined, MODIS FPAR linearly interpolated, and MODIS EVI, splined, see Tab. 1). MODIS FPAR data are from the MCD15A3H, Collection 6 dataset (Myneni et al., 2015), given at a resolution of 500 m and 4 days. The data were filtered to remove data points where clouds were present, values equal to 1.00, and outliers (more than three times the inter-quartile range). Filtered values were replaced by the mean value for the respective day-of-year. To obtain daily varying  $I_{\text{abs}}$  (Eq. 18), two alternatives were explored. For the first (used in all setups except FULL\_FPARitp), values were derived using a cubic smoothing spline (function `smooth.spline()` with parameter `spar=0.01` in R (R Core Team, 2016)). For setup FULL\_FPARitp, daily fAPAR values were linearly interpolated to each day. MODIS EVI data is from the MOD13Q1, collection 6 dataset (Didan, 2015), given at a resolution of 250 m and 8 days. This data were filtered based on the summary quality control flag, removing “cloudy”

pixels. Gaps were filled and data was splined to daily values. All fAPAR data were downloaded from Google Earth Engine using the *google\_earth\_engine\_subsets* library (Hufkens, 2017).

265 For global-scale simulations, we used two alternative fAPAR datasets. ‘MODIS FPAR’ is from globally gridded MODIS FPAR data at  $0.5^\circ$  resolution derived at ICDC (<http://icdc.cen.uni-hamburg.de>), based on the MOD15A2H MODIS Terra Leaf Area Index/FPAR 8-Day L4 Global 500m SIN Grid V006 dataset (Myneni et al.). For the present application, 8-daily data is aggregated (mean) to monthly data. ‘fAPAR3g’ is based on AVHRR GIMMS FPAR3g v2 data (Zhu et al., 2013), 15 days,  $1/12^\circ$  resolution and aggregated for the present application to  $0.5^\circ$  and monthly data. For all global P-model simulations, 270 fAPAR is held constant for each day in respective months. Simulations cover years 2000-2016. Due to limited temporal coverage, January 2000 data is taken as February 2000 for simulations driven by MODIS FPAR.

### 3.4.2 Meteorological data

For site-scale simulations, the meteorological forcing data are derived from the FLUXNET 2015 Tier 1 dataset (daily), which provides data from measurements taken and processed along with the  $\text{CO}_2$  flux measurements. The photosynthetic photon flux 275 density PPFD ( $\text{mol m}^{-2} \text{d}^{-1}$ ) is derived from shortwave downwelling radiation as  $\text{PPFD} = 60 \cdot 60 \cdot 24 \cdot 10^{-6} k_{\text{EC}} R_{\text{SW}}$ , where  $k_{\text{EC}} = 2.04 \mu\text{mol J}^{-1}$  (Meek et al., 1984), and  $R_{\text{SW}}$  is incoming shortwave radiation from daily FLUXNET 2015 data (variable name `SW_IN_F`, given in  $\text{W m}^{-2}$ ). The factor  $k_{\text{EC}}$  accounts for the energy content of  $R_{\text{SW}}$  and the fraction of photosynthetically active radiation in total short-wave radiation. Daytime vapour pressure deficit (VPD, or  $D$  in Sect. 2) is calculated from half-hourly FLUXNET 2015 data (variable name `VPD_F`) by averaging over time steps with positive insolation (`SW_IN_F`). 280 Daytime air temperature is taken directly from the FLUXNET 2015 dataset (variable name `T_F_DAY`). This is a simplification, as we are not calculating leaf temperature or VPD at the leaf surface, which are more directly relevant for photosynthesis.

For global-scale simulations, we use daily,  $0.5^\circ$  meteorological forcing from WATCH-WFDEI (Weedon et al., 2014). We use mean daily 2 m air temperature; daily snow and rainfall; shortwave downwelling radiation converted to  $\text{mol photons m}^{-2} \text{d}^{-1}$  by multiplication with  $k_{\text{EC}}$ ; and daily 2 m specific humidity ( $q_{\text{air}}$ ), converted to VPD ( $D$ ) as described in Appendix E. We 285 used daily minimum and maximum air temperatures for each month from CRU TS 4.01 data (Harris et al., 2014) to calculate a respective VPD and use their mean as input to P-model simulations in order to reduce effects of the non-linear dependence of  $D$  on  $T$  ( $\overline{D} = (D(T_{\text{min}}) + D(T_{\text{max}}))/2$ ). All processes that depend on atmospheric pressure use Eq. B10 and the  $0.5^\circ$  resolution elevation map from WATCH-WFDEI (Weedon et al., 2014) to calculate a temporally constant atmospheric pressure for each gridcell.

## 290 3.5 Calibration and evaluation data

### 3.5.1 Data for site-scale simulations

We used data from 59 sites for model calibration and 126 sites for evaluation (Fig. 1, and Tab. A1). The number of valid daily GPP data points used for the calibration set was 162,158 and 241,084 for the evaluation set. The calibration sites were selected based on the apparent reliability of relationships between  $\text{CO}_2$  fluxes, co-located greenness data, measured soil moisture, and

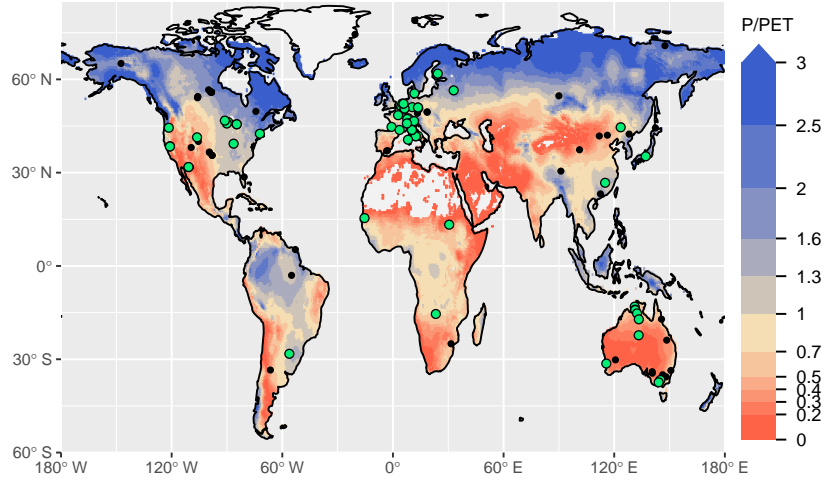


**Figure 1.** Overview of sites selected for model calibration (green dots) and evaluation (black dots). All sites and additional information are listed in Tab. A1. The color key of the map represents aridity, quantified as the ratio of precipitation over potential evapotranspiration from Greve et al. (2014).

295 meteorological variables, emerging from a previous analysis (Stocker et al., 2018). For the evaluation, we used all sites except those classified as croplands or wetlands, and seven sites where  $C_4$  vegetation is mentioned in the site description available through the FLUXNET2015 dataset (AU-How, DE-Kli, FR-Gri, IT-BCi, US-Ne1, US-Ne2, and US-Ne3).

GPP predictions by the P-model are compared to GPP estimates from the FLUXNET 2015 Tier 1 data set (downloaded on 13 November, 2016). We used GPP based on the nighttime partitioning method (Reichstein et al., 2005) (GPP\_NT\_VUT\_REF) and removed data for which more than 50% of the half-hourly data are gap-filled and for which the daytime and nighttime partitioning methods (GPP\_DT\_VUT\_REF and GPP\_NT\_VUT\_REF, respectively) are inconsistent, i.e., the upper and lower 2.5% quantiles of the difference between GPP values quantified by each method. For additional simulation sets, model calibration and evaluation was performed using GPP data based on the daytime partitioning method (GPP\_DT\_VUT\_REF) (Lasslop et al., 2010) with analogous filtering steps, and GPP data based on an alternative method that fits a constant ecosystem respiration rate as the net ecosystem exchange under conditions where PPFD tends to zero (FULL\_Ty, Wang et al. (2017a)). For all calibration and evaluation, we removed data points before the “MODIS era” (before 18th of February, 2000).

### 3.5.2 Data for global-scale simulations

We compare the simulated spatial distribution of GPP from global-scale simulations against seven different remote sensing data-driven GPP estimates with global coverage and two sun-induced fluorescence (SiF) data products. The global GPP estimates are from the following models: MTE (Jung et al., 2011), FLUXCOM (‘RS+METEO’ setup) (Tramontana et al., 2016), MODIS GPP (MOD17A2H collections 55 and 6) (Running et al., 2004; Zhao et al., 2005; Running and Mu, 2015), BESS

(Jiang and Ryu, 2016), BEPS (He et al., 2018; Chen et al., 2016), and VPM (Zhang et al., 2017b). A more detailed description of these models and aggregation to a common grid of  $0.5^\circ$  and monthly resolution can be found in Luo et al. (2018). For sun-induced fluorescence (SiF), we use data from GOME-2A and GOME-2B, based on v.2 (V27) 740 nm terrestrial chlorophyll  
 315 fluorescence data from the MetOp-A and MetOp-B satellites (Joiner et al., 2013, 2016). Data were aggregated to monthly and  $0.5^\circ$  resolution by mean, as further described in Luo et al. (2018).

### 3.6 Evaluation methods

We evaluated both simulated LUE and GPP. The P-model (Sect. 2) predicts variations in LUE across sites (space) and months (monthly  $\text{LUE} = m'$ ), while simulated GPP is affected by the PPFD and fAPAR data used as model forcing (Eq. 19 and  
 320 Sect. 3.4). Conversely, “observed” LUE is calculated as  $\text{LUE}_{\text{obs}} = \text{GPP}_{\text{obs}} / (\text{fAPAR} \cdot \text{PPFD})$  and the evaluation is thus also affected by the PPFD and fAPAR data. The evaluation of LUE tests the added explanatory power of the P-model compared to models that rely on fixed prescribed LUE values. Evaluating GPP facilitates the comparison of the model performance to similar models of terrestrial GPP. Model performance for GPP is benchmarked against a null model (NULL), which assumes a temporally constant and spatially uniform LUE. The LUE for the NULL model is fitted to observed GPP using linearly  
 325 interpolated MODIS FPAR and GPP data from the NT method, see Tab. 1. Thus, while LUE is constant, the NULL model preserves the spatial and temporal patterns in APAR ( $= \text{fAPAR} \cdot \text{PPFD}$ ).

#### 3.6.1 Components of variability

For LUE, we separately analysed spatial (mean annual values by site) and monthly means only for the FULL setup. For GPP, we analyzed spatial, annual, seasonal (mean by day-of-year), 8-daily, and the variability in daily anomalies from the mean  
 330 seasonal cycle for all setups. The seasonal variability was determined for different Koeppen-Geiger climatic zones (see Tab. 2). Information about the association of sites with climatic zones was extracted from Falge et al. (2017). Evaluations were made only for climatic zones with at least three sites. For each component of variability, we calculated the adjusted coefficient of determination ( $R_{\text{adj}}^2$ , thereafter referred to as  $R^2$ ), and the root mean square error (RMSE). Figures showing correlations between simulated and observed values additionally present the mean bias, the slope of the linear regression model, and the  
 335 number of data points ( $N$ ).

#### 3.6.2 Drought response

The bias in GPP (modelled minus observed) was calculated for 20 days before and 80 days after the onset of a drought event as identified by Stocker et al. (2018) for 36 sites. Drought events (fLUE droughts) are periods of consecutive days where soil moisture, separated from other drivers using neural networks, reduces LUE below a given threshold. The data specifying the  
 340 timing and duration of drought events was downloaded from *Zenodo* (Stocker, 2018). We then re-arranged the data to align all drought events at all sites, normalised data to their median value during the ten days before the onset of droughts (normalisation by subtracting median), and computed quantiles per day, where ‘day’ is defined with respect to the onset of each drought event.

**Table 2.** Description of Koeppen-Geiger climate zones and number of sites for which data is available per climate zone and hemisphere. Sites are classified based on Falge et al. (2017), and Beck et al. (2018). Only zones with data from more than three sites are shown.

Code	<i>N</i> north	<i>N</i> south	Description
Aw	–	5	Tropical savannah
BSk	5	–	Arid steppe cold
Cfa	11	–	Warm temperate fully humid with hot summer
Cfb	20	5	Warm temperate fully humid with warm summer
Csa	12	–	Warm temperate with dry and hot summer
Csb	4	–	Warm temperate with dry and warm summer
Dfb	17	–	Cold fully humid with warm summer
Dfc	21	–	Cold fully humid with cold summer

## 4 Results

### 4.1 Calibration results

345 The calibration of model parameters, done with data from all calibration sites simultaneously, yielded values that closely  
 matched the means across parameter values derived from the out-of-sample calibrations (Fig. 2). This confirms the robustness  
 of the calibration and that the model is not overfitted. Similarly for the evaluation metrics, the  $R^2$  and RMSE values reported  
 from evaluations against data from all evaluation sites pooled yielded values that closely match the means across the out-of-  
 sample evaluations (each calculated with data from the single left-out site). This analysis also shows that the distribution of  
 350 the evaluation metrics is skewed, with evaluations against a few sites indicating relatively poor performance ( $R^2$  below 0.5  
 for ZM-Mon, AR-Vir, and FR-Pue), while the most frequent values indicate very good model performance (evaluations at 21  
 sites giving  $R^2$  values of above 0.8). Because the out-of-sample calibrations are computationally very expensive, we performed  
 this analysis only for one setup (FULL) and report evaluation metrics done with pooled data from all evaluation sites for the  
 remainder of the analysis.

### 355 4.2 GPP variability across scales

Tables 3 and 4 provide an overview of model performance ( $R^2$  and RMSE) in simulating GPP at different scales. The ORG  
 setup captures 70% of the variance in observed GPP with data aggregated to 8-day means (33’604 data points). Model per-  
 formance both with respect to explained variance ( $R^2$ ) and the RMSE is improved by including the effects of temperature on  
 quantum yield efficiency in the BRC model setup ( $R^2 = 72\%$ ), and by including the effects of soil moisture stress in the FULL  
 360 model setup ( $R^2 = 75\%$ , Fig. 3). Both the BRC and FULL model setup outperform the NULL model.

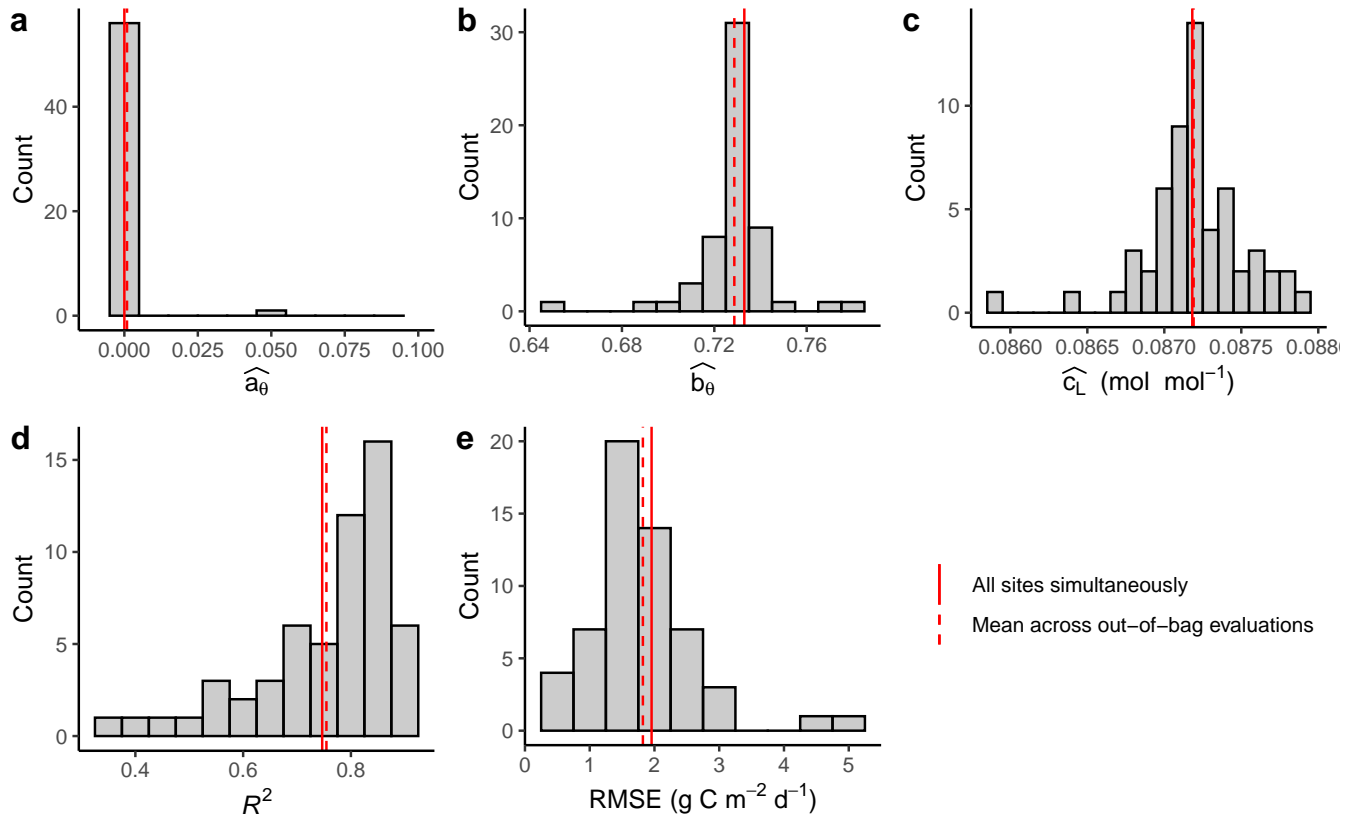


**Figure 2.** Out-of-sample calibration and evaluation results. (a-c) Distribution of parameter values (setup FULL) from calibrations where data from one site was left out for each individual calibration. Parameters  $\hat{a}_\theta$  and  $\hat{b}_\theta$  are unitless. (d, e) Distribution of evaluation metrics calculated on data from the left-out site based on simulations with model parameters calibrated on all other sites' data. Solid red vertical lines represent the parameter values calibrated with data from all sites pooled. These are the values reported in Tabs. 3 and 4 for setup FULL. Dashed red lines represent the mean across values from out-of-bag calibrations and evaluations.

#### 4.2.1 Seasonal variations

Seasonal variations are generally reliably simulated ( $R^2$ : 0.69-0.73 for P-model setups, and  $R^2$ : 0.71 for the NULL model, Fig. 4). Also the NULL model captures most of the seasonal variability, especially in climate zones Dfb and Dfc, and Cfb and Cfa. This indicates that seasonal GPP variations are largely driven by seasonal changes in insolation (PPFD) and vegetation greenness (fAPAR). Accounting for temperature effects on the quantum yield efficiency reduces the overestimation of GPP in spring, except in the case of climate zone Dfb. Observed GPP increases are lagged compared to vegetation greenness, with a delay of up to 2 months at some sites. This lag is clearly visible at almost all sites in Dfb. The early season high bias is largely absent for sites in climate zone Cfb, where observed GPP starts increasing early and the simulations match the observations except at sites CZ-wet, DE-Hai, and FR-Fon, where the simulated start of season is simulated too early.

**Table 3.**  $R^2$  of simulated and observed GPP based on different model setups and for different components of variability.

Setup	8-daily	Spatial	Annual	Seasonal	var(daily)	var(annual)
FULL	0.75	0.69	0.69	0.73	0.27	0.09
BRC	0.72	0.65	0.63	0.72	0.25	0.06
ORG	0.70	0.63	0.60	0.69	0.24	0.05
NULL	0.68	0.65	0.58	0.71	0.21	0.03
FULL_FPARItp	0.73	0.71	0.69	0.74	0.24	0.10
FULL_EVI	0.70	0.58	0.47	0.71	0.27	0.15
FULL_DT	0.64	0.67	0.69	0.64	0.30	0.10
FULL_NTsub	0.66	0.69	0.69	0.66	0.30	0.09
FULL_Ty	0.68			0.68	0.49	

**Table 4.** Root mean square error (RMSE) of simulated and observed GPP based on different model setups and for different components of variability.

Setup	8-daily	Spatial	Annual	Seasonal	var(daily)	var(annual)
FULL	1.96	426.66	398.63	1.84	1.55	166.97
BRC	2.05	454.78	438.14	1.89	1.54	170.54
ORG	2.15	466.19	447.80	1.99	1.54	172.54
NULL	2.19	465.21	465.99	1.94	1.58	173.71
FULL_FPARItp	2.01	427.47	404.98	1.82	1.64	165.51
FULL_EVI	2.13	513.68	526.98	1.91	1.49	159.82
FULL_DT	2.16	411.30	392.34	2.00	1.69	180.75
FULL_NTsub	2.15	426.64	398.60	1.98	1.70	166.97
FULL_Ty	1.92			1.79	1.38	

370 GPP is overestimated during the dry season in climate zones with a marked dry season (Aw, BSk, Csa, and Csb) in model setups that do not account for soil moisture stress (ORG, BRC, NULL). The NULL model has the largest bias. High VPD during dry periods reduces simulated LUE and leads to lower GPP values and a smaller bias in all the P-model setups (ORG, BRC, FULL). The empirical soil moisture stress function applied in setup FULL eliminates the dryness-related bias in zones Aw, Csa, and Csb and substantially reduces this bias for sites in zone BSk. Observations suggest that GPP declines to values  
375 around zero during dry periods at sites in zone BSk (mostly savannah vegetation and grasslands, see Table A1). The remaining bias in the FULL model, which includes the soil moisture stress function, is related to the fact that prescribed fAPAR remains relatively high and that the soil moisture stress function does not decline to zero.



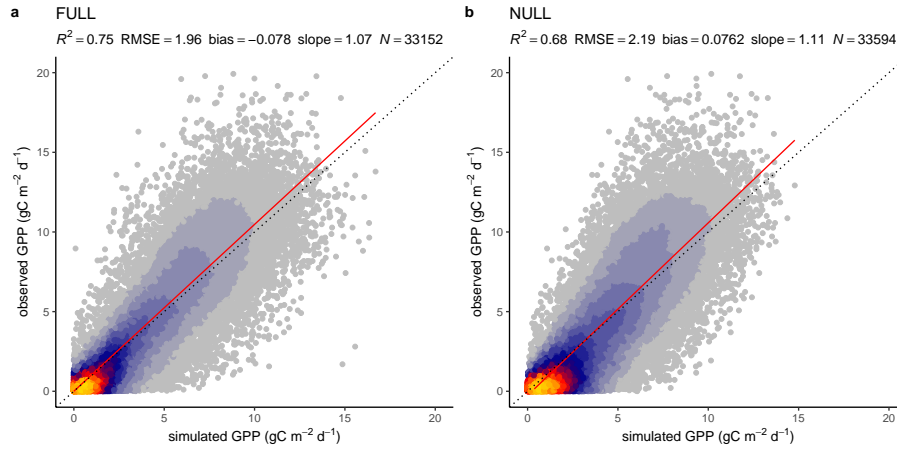


**Figure 3.** Correlation of observed and modelled GPP values of all sites pooled, mean over 8-day periods, for the model setup FULL (a) and NULL (b).

The ORG and BRC models tend to underestimate peak season GPP more strongly compared to the FULL model. This is a direct consequence of the calibration which balances errors across all data points. Across-site average peak-season maximum GPP is accurately captured by the FULL model in most zones (Fig. 4), except for an underestimation of GPP in zones Aw, Cfa, and Cfb, and an overestimation in zone Csa. Site-level evaluations suggests no clear relationship between peak-season underestimation and vegetation type in zone Cfb. The overestimation of peak-season GPP in zone Csa is caused by a high bias at sites with evergreen broadleaved vegetation (FR-Pue, IT-Cp2, IT-Cpz); sites with other vegetation types show no consistent peak season bias.

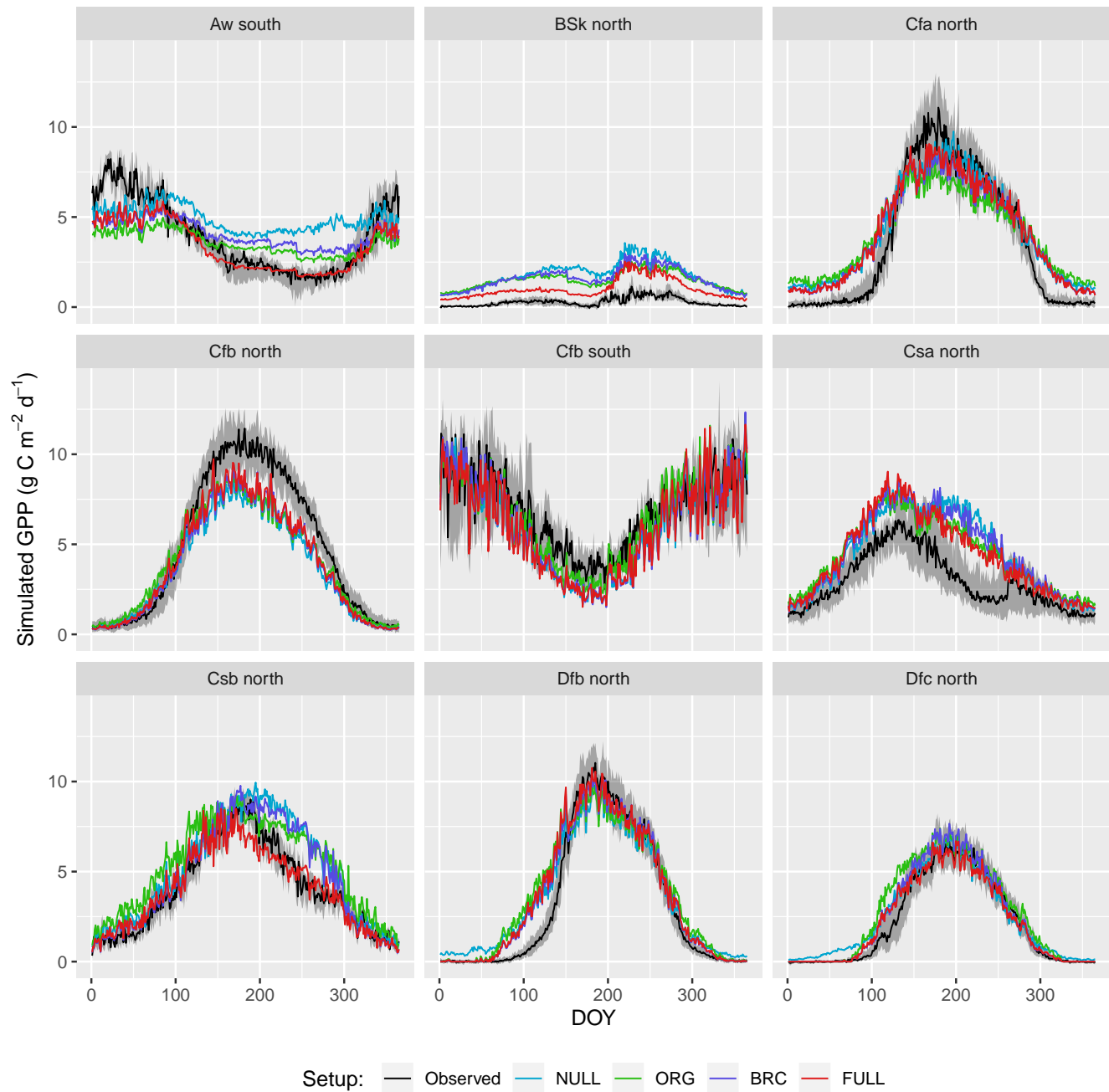


**Figure 4.** Mean seasonal cycle. Observations are given by the black line and grey band, representing the median and 33/66 % quantiles of all data (multiple sites and years) pooled by climate zone. Coloured lines represent different model setups. The annotation above each plot specifies the climate zone (see Tab. 2). Only climate zones are shown here for which data from at least five sites was available.

The  $R^2$  for simulated GPP, aggregated to annual totals, ranges from 0.60 (ORG) to 0.69 (FULL). The NULL model achieves an  $R^2$  of 0.58. Most of the explanatory power of the different models for predicting annual total GPP stems from their power in predicting between-site (“spatial”) variations (Fig. 5). The  $R^2$  for spatial variations ranges from 0.63 (ORG) to 0.69 (FULL), and 0.65 for the NULL model. In contrast, inter-annual variations at a site are poorly simulated ( $R^2$ : 0.05-0.09 for P-model setups, and 0.03 for the NULL model). Inter-annual variations are generally much smaller than between-site (spatial) variations or seasonal variations. Thus, capturing them is challenging. Inter-annual GPP variations are generally better simulated at sites where the variability is high and in particular at dry sites.

### 4.3 Drought response

The P-model setups that do not include the soil moisture stress function (ORG and BRC) systematically overestimate GPP during droughts (Fig. 6). This bias increases sharply at the onset of drought events and continues to increase throughout the drought period. The bias is strongly reduced by applying the empirical soil moisture stress function (Eq. 21) in the FULL model. A small bias remains also in the FULL model. This stems from overestimated values at a few sites (in particular AU-DaP, US-Cop, US-SRG, US-SRM, US-Var, US-Whs, US-Wkg), mostly grasslands and sites in seasonally dry climate zones (Aw, BSk, and Csa, see Fig. 4), where flux measurements indicate an almost complete shut-down of photosynthetic activity during the dry season. In contrast, the fAPAR data (MODIS FPAR) suggest values substantially greater than zero at these sites during these periods. This suggests either contributions to PAR absorption by photosynthetically inactive tissue, underestimation of LUE sensitivity to dry soils at these sites, or an overestimation of the rooting zone moisture availability by the SPLASH model.

### 4.4 Uncertainty from fAPAR input data

Tests of the sensitivity of model performance to alternative fAPAR forcing datasets show that the difference between splined and linearly-interpolated MODIS FPAR is small, with slightly better performance using splined fAPAR data. Model performance is generally better using MODIS FPAR compared to simulations using MODIS EVI. Spatial variations in particular, are better captured using MODIS FPAR (Fig. 5,  $R^2$ : 0.69 for setup FULL) compared to MODIS EVI ( $R^2$ : 0.58). However, the  $R^2$  of inter-annual variations is 0.15 for MODIS EVI and 0.09 for MODIS FPAR. In terms of biases in climate zones, the overestimation of GPP during the dry period in zone BSk is larger when using MODIS EVI than when using MODIS FPAR (Fig. 7, right). The positive spring bias in simulated GPP in zone Dfb is present irrespective of the source of the fAPAR forcing (Fig. 7, left), as is the peak-season bias of GPP in zones BSk, Cfb, and Csb (not shown). Differences between the EVI and FPAR-forced simulations depend on vegetation type. The EVI-forced simulation tends to be low biased in evergreen needle-leaved vegetation, and has generally lower values in all evergreen vegetation types compared to the FPAR-forced simulation. However, there is no general difference in model bias between simulations made with the two forcings in other vegetation types.

## 4.5 GPP target data

The different flux decomposition methods make fundamentally different assumptions regarding the sensitivity of ecosystem respiration to diurnal changes in temperature. This should lead to systematic differences in derived observational GPP values and should affect model-data disagreement.

Model predictions compare better to GPP data based on the flux decomposition method Ty (Wang et al., 2017a) than for GPP data based on the DT and NT methods. For GPP 8-day means, the model achieves an  $R^2$  of 0.68 when compared to GPP Ty (model setup FULL\_Ty), as opposed to 0.64 and 0.66 compared to the DT and NT methods, respectively (FULL\_DT and FULL\_NTsub, Tab. 3, Fig. 8). Spatial and annual correlations are not evaluated for GPP Ty due to missing data. Evaluations presented here rely on dates for which neither the NT, DT, nor Ty method has missing values and thus contain an equal number of data points. Metrics from the NT evaluation, repeated here, are not identical to the ones above and are referred to as ‘NTsub’ in Tables 3 and 4.

We found a systematic low bias of simulated GPP in the peak-season in the climatic zone Cfb (warm temperate, fully humid, warm summer). However, as shown in Fig. 8, this bias does not seem to be affected by the choice of GPP evaluation data.

## 4.6 LUE

The FULL version of the P-model captures 32% of the variability in mean annual LUE across all sites and across the full range of observed mean annual LUE values and vegetation types (Fig. 9). 48% of the observed LUE variation within vegetation types is captured by the model through the relationships with climate, without the need to specify parameters for specific vegetation types.

31% of the variability in monthly mean LUE is captured by the model, with data from all sites and years pooled (Fig. 9). The model overestimates monthly LUE values and underestimates LUE at the lowest and highest end of the LUE range respectively. The low-end overestimation is reflected by the overestimation of GPP in the spring at winter-cold sites (Sect. 4.2.1) and during soil moisture droughts (Sect. 4.3). The underestimation of high monthly values is not clearly linked to any particular vegetation type.

## 4.7 Global GPP

Simulated global total GPP is 106 GtC yr<sup>-1</sup> when using MODIS FPAR and 122 GtC yr<sup>-1</sup> when using fAPAR3g forcing data (mean over years 2001-2011, setup FULL). The spatial pattern of simulated GPP differs substantially between simulations forced by MODIS FPAR and fAPAR3g (Fig. 10). This is most evident in their latitudinal distribution (Fig. 11). The global spatial pattern of fAPAR3g-based GPP simulated by the P-model generally matches the global distribution of the mean across other remote sensing-based GPP models and lies within the range of their estimates for the latitudinal distribution. The MODIS FPAR-forced P-model simulation suggests lower values in the tropics that differ from the fAPAR3g-based estimates by a factor of  $\sim 2$  around the equator. The moderate tropical GPP of the MODIS FPAR-based P-model simulation agrees well with the latitudinal distribution of sun-induced fluorescence (SiF) from GOME-2A and GOME-2B.

## 5 Discussion

The performance of the P-model can be compared to results obtained from other remote-sensing driven GPP models (RS-models). In its FULL setup, the P-model achieves an  $R^2$  of 0.75 and a RMSE of  $1.96 \text{ g C m}^{-2} \text{ d}^{-1}$ , in simulating 8-day mean GPP and evaluated against GPP data (NT method) from 126 sites. This can be compared to predictions from the VPM model ( $R^2$ : 0.74, RMSE:  $2.08 \text{ g C m}^{-2} \text{ d}^{-1}$ , 113 sites, 8-daily, Zhang et al. (2017a)), or BESS ( $R^2$ : 0.67, RMSE:  $2.58 \text{ g C m}^{-2} \text{ d}^{-1}$ , 113 sites, 8-daily, Jiang and Ryu (2016)). The performance of the P-model in simulating *annual* GPP across all 126 sites ( $R^2$ : 0.69) can be compared to results from MODIS GPP (MOD17A2,  $R^2$ = 0.73, 12 sites, Heinsch et al. (2006), and for the updated version MOD17A2H:  $R^2$ = 0.62, 18 sites, Wang et al. (2017b)), or BEPS ( $R^2$ : 0.81, RMSE:  $347 \text{ g C m}^{-2} \text{ d}^{-1}$ , 124 sites (He et al., 2018)). Unfortunately, we cannot present a direct comparison between these models based on data from identical dates and sites. A targeted model intercomparison may address this. While seasonal and spatial variations in GPP are reliably simulated by the P-model, the model's performance in simulating interannual GPP variations is weaker. Similar results regarding relatively poor model performance in explaining interannual variations have been found from previous studies in both empirical (Richardson et al., 2007; Urbanski et al., 2007b) and process model-based (Keenan et al., 2012; Biederman et al., 2016) analyses. This is likely due to lagged effects of climate anomalies expressed through biotic responses (Richardson et al., 2007; Keenan et al., 2012).

The P-model-based estimates of global GPP ( $106 \text{ GtC yr}^{-1}$  when using MODIS FPAR and  $122 \text{ GtC yr}^{-1}$  when using fAPAR3g forcing data, mean over 2001-2011, FULL setup) are within the range of other estimates of global GPP (also means over 2001-2011):  $133 \text{ GtC yr}^{-1}$  for MTE (Jung et al., 2011),  $130 \text{ GtC yr}^{-1}$  for FLUXCOM (Tramontana et al., 2016),  $112 \text{ GtC yr}^{-1}$  for MODIS-55 GPP and  $105 \text{ GtC yr}^{-1}$  for MODIS-6 GPP (Running et al., 2004; Zhao et al., 2005),  $133 \text{ GtC yr}^{-1}$  for BESS (Jiang and Ryu, 2016; Ryu et al., 2011),  $121 \text{ GtC yr}^{-1}$  for BEPS (He et al., 2018; Chen et al., 2016), and  $135 \text{ GtC yr}^{-1}$  for VPM (Zhang et al., 2017b). The P-model results presented here are based on simulations that embody relatively strong simplifying assumptions. In particular, we assumed all vegetation to follow the  $\text{C}_3$  photosynthetic pathway and we made no distinction between croplands and other vegetation, although crops are often more productive (Guanter et al., 2014). Due to the short period for which forcing data and outputs from comparable models are available, we did not analyse temporal trends in global GPP here. Analyses not shown here indicate that the introduction of the  $J_{\text{max}}$  cost factor (not included, e.g., in Keenan et al. (2017)) increases the sensitivity of modelled GPP to  $\text{CO}_2$ . Further evaluation of model behaviour against data from  $\text{CO}_2$  manipulation experiments will be necessary before applying the model to simulate  $\text{CO}_2$ -related trends.

The large spread of tropical GPP estimates is striking. The highest estimate among the other GPP models we used for evaluation here – coming from BESS – is more than 50% higher than MODIS GPP from Collection 6. The fAPAR3g-based P-model tropical GPP estimate falls within the range of other GPP models, while the MODIS FPAR-based estimate is lower than all other models. However, the latter's comparably low tropical GPP agrees well with the latitudinal distribution of SiF (Fig. 11). However, large changes in leaf area index across latitudes, combined with a dependency of the SiF signal on vegetation structure (Zeng et al., 2019) may undermine the validity of SiF as a benchmark for the latitudinal GPP distribution. A lack of

evaluation data from eddy-covariance measurements in dense tropical forests precludes us from drawing conclusions on the accurateness of these diverging tropical GPP estimates.

With a particular focus on soil moisture effects, Stocker et al. (2019) presented global GPP based on the P-model, corresponding to a setup with the soil moisture stress function but without the temperature-dependence of the quantum yield efficiency. They also used a different parametrisation with  $\varphi_0 = 0.0579$ ,  $a_\theta = 0.107$ , and  $b_\theta = 0.478$  for their intermediate model version. Their estimate for global GPP was around 130 PgC yr<sup>-1</sup> for recent years.

The coefficients of determination ( $R^2$ ) of simulated versus observed values are lower for LUE (0.32 for the spatial correlation in the FULL setup, Fig. 9b) than for GPP (0.69 for the spatial correlation in the FULL setup). This is because GPP variations are strongly driven by variations in absorbed light (PPFD-fAPAR), which are observed and used for modelling. In contrast, variations in LUE cannot be observed directly. Using remotely-sensed information for estimating LUE variations, e.g., based on sun-induced fluorescence (Frankenberg et al., 2018; Li et al., 2018; Ryu et al., 2019) or alternative reflectance indices (Gamon et al., 1992, 2016; Badgley et al., 2017), is an active field of research and the separation of remotely sensed signals into contributions by LUE and absorbed light remains challenging (Porcar-Castell et al., 2014; Ryu et al., 2019). Other remote sensing-based GPP models rely on vegetation type-specific model parameters for LUE (Zhang et al., 2017a; Running et al., 2004; Jiang and Ryu, 2016). The P-model in its FULL setup explains 48% of the variations in LUE across sites aggregated to vegetation types without relying on vegetation or biome-type specific parametrisations. In its ORG setup, it explains 12% of the variations (not shown), and 51% of the variations when excluding sites classified as ‘open shrublands’, which tend have a substantially lower LUE than simulated by the P-model (not shown). In spite of this substantial portion of explained variability, the NULL model with its temporally constant and spatially uniform LUE achieves higher  $R^2$  values for GPP than the ORG P-model setup at the spatial, annual, and seasonal scales (Tab. 3). This indicates that the spatial and temporal variations in absorbed light are the main drivers of GPP in LUE-type models and underlines the importance of evaluation against a NULL model benchmark. Taken together, these findings demonstrate that the P-model offers a simple but powerful method for simulating terrestrial GPP using readily available input datasets and a very small number of free (calibratable) parameters. Here, three parameters are calibrated (for the FULL setup). Other model parameters are derived from independent field and laboratory measurements.

Accounting for the temperature-dependence of the quantum yield efficiency ( $\varphi_0$ ) clearly improves model predictions. The parameter  $\varphi_0$  is commonly treated as a constant in global vegetation models (Rogers et al., 2017). Our results indicate potential for improving such models’ photosynthesis routines by accounting for the temperature-dependence of  $\varphi_0$ .

$\varphi_0$  appears as a linear scalar in the LUE model. However, the magnitude of this scalar is uncertain and depends on whether incomplete light absorption by the leaf is included in the definition of  $\varphi_0$  or in fAPAR data. We have used MODIS FPAR and MODIS EVI data to define fAPAR in different model setups. While the two are well correlated, their absolute values differ. Hence, we have calibrated an *apparent* quantum yield efficiency ( $\widehat{\varphi_0}$ ) to GPP data separately for different fAPAR datasets, thereby implicitly distinguishing what components of light absorption factors are contained in the fAPAR data. The leaf absorbance  $a_L$ , which is typically taken to be around 0.8 in global vegetation models (Rogers et al., 2017) is similar to the ratio of fitted  $\widehat{\varphi_0}$  values for simulation FULL and FULL\_EVI, here calculated as 0.67 (Tab. 1).

An improvement in model performance is obtained by accounting for soil moisture stress using an empirical function. However, the use of an empirical function masks underlying processes. Furthermore, the use of an empirical function is not consistent with the optimality approach that underlies the P-model. The bias reduction associated with using an empirical  
520 soil moisture stress function hints at missing factors in the theoretical approach which rests on an assumed constancy of the unit costs of transpiration ( $a$  in Eq. 3). Prentice et al. (2014) provide a definition of  $a$  that is explicit in terms of plant hydraulic traits and physical properties that determine water transport along the plant-soil-atmosphere continuum. In particular,  $a \propto (\Delta\Psi k_s)^{-1}$ , where  $\Delta\Psi$  is the maximum daytime difference in leaf-to-soil water potential and  $k_s$  is the sapwood area-specific permeability. However, large variations in stomatal conductance are known to occur in response to relatively fast soil  
525 dry-downs (time scale of days) (Keenan et al., 2010; Egea et al., 2011; Stocker et al., 2018). This suggests a potential to improve the P-model by allowing the unit cost of transpiration to be a function of rooting-zone moisture availability, and by coupling stomatal conductance with the soil water balance.

Observational uncertainty could affect both parameter calibration and model evaluation. Keenan et al. (2019) found a systematic bias in GPP estimates based on the nighttime partitioning method due to inhibition of leaf respiration in the light (Kok,  
530 1949; Wehr et al., 2016), which affects fluxes unevenly throughout the season and across vegetation types. However, we found no clear difference in model-data agreement, nor in fitted parameters, in comparisons of three alternative GPP datasets that use different approaches to decompose net CO<sub>2</sub> exchange fluxes from eddy covariance measurements into ecosystem respiration and GPP terms.

We have found a consistent early-season high-bias in simulated GPP for numerous sites in regions with deciduous broadleaved  
535 vegetation in temperate and cold climates (in particular US-MMS, IT-Col, US-WCr, US-UMd, US-UMB, and US-Ha1), and also in mixed and needle-leaved stands (in particular US-Syv, US-NR1, FI-Hyy, CA-Qfo, and CA-Man). The temperature-dependence of the intrinsic quantum yield, as introduced in setups BRC and FULL, did not resolve this bias. Additional analyses (not shown) suggested that this bias is not related to soil temperatures. The P-model, as applied here, uses daily air temperature for simulating temperature stress on the intrinsic quantum yield in setups BRC and FULL. A reduction in  
540 the quantum yield efficiency arises from several mechanisms, including increased non-photochemical quenching, a reduction in chlorophyll and absorption by screening pigments (Huner et al., 1993; Oquist and Huner, 2003; Ensminger et al., 2004; Adams et al., 2004; Verhoeven, 2014). These adaptations serve to limit oxidative damage under high light and low temperature conditions, where an imbalance between electron supply and demand exists, arising from an imbalance between temperature-insensitive photochemical rates and temperature-sensitive biochemical rates. The reversion of these adaptations and resumption  
545 of the intrinsic quantum yield efficiency and photosynthesis requires sustained temperatures above a certain critical threshold (Tanja et al., 2003) and exhibits a delay with respect to instantaneous air temperatures (Pelkonen and Hari, 1980; Mäkelä et al., 2004). Approaches accounting for a delayed resumption of photosynthesis after cold periods offer scope for further improvement of the P-model and may be included in global vegetation and Earth system models where this effect is currently not accounted for (Tanja et al., 2003; Rogers et al., 2017).

550 There is a positive bias in simulated GPP during the dry season at a number of sites where the vegetation phenology is influenced by drought. The positive bias is related to the combination of using prescribed fAPAR data, which shows substantial

absorption by non-green vegetation, and insufficient sensitivity of simulated LUE to soil drying. However, GPP is accurately simulated at other sites affected by seasonally recurring water stress. The modelled sensitivity to dry soils is determined by the soil moisture stress function, which depends on the mean aridity of the site as estimated using a fixed depth soil moisture "bucket". Accounting for variability in rooting zone depth, which may also be influenced by local topographical factors and access to groundwater (Fan et al., 2013, 2017) may help to minimise model biases in drought-prone areas.

The current implementation of the P-model involves some simplifications in terms of climate drivers by using average daily meteorological conditions, measured above the canopy, as input. Optimality in balancing carbon and water costs for average daily conditions is not necessarily equivalent to optimality in balancing integrated water and carbon costs over the diurnal cycle. Large variations in ambient conditions over a diurnal cycle, combined with a non-linear dependence of costs on these conditions suggest that the approach of taking average daily conditions may be an over-simplification. Nevertheless, prior evaluations have shown robust and accurate predictions of optimal  $\chi$  across a range conditions (Wang et al., 2017a). Using above-canopy VPD values instead of VPD at the leaf surface for scaling water losses implicitly assumes a perfectly coupled atmospheric boundary layer. Using above-canopy air temperature instead of leaf temperatures introduces a bias when the two become decoupled (Michaletz et al., 2015). The impact of these simplifications may be minor but should be evaluated.

A further simplification is that investment in electron transport capacity (expressed by  $J_{\max}$ ) and investments in the carboxylation capacity (expressed by  $V_{\max}$ ) are coordinated so that for conditions with which the model is forced (here, monthly means of daily averages), photosynthesis operates at the co-limitation point of the light- and Rubisco-limited assimilation rates and an effective linear relationship between absorbed light and mean assimilation emerges. This assumption follows from the *coordination hypothesis* (Chen et al., 1993; Haxeltine and Prentice, 1996), which itself can be understood as an optimality principle (Haxeltine and Prentice, 1996), and is well supported by observations (Maire et al., 2012). However, this coordination is contingent on the time scale at which photosynthetic acclimation occurs, which is not known precisely (Smith and Dukes, 2013; Way and Yamori, 2014). By simulating  $\chi$  using monthly mean meteorological variables, we assume a monthly time scale of acclimation. This is probably a conservative estimate (Smith and Dukes, 2017; Veres and Williams, 1984). Considering the concave relationship of assimilation rates and absorbed light that follows from the FvCB model for a given  $J_{\max}$ , linearly scaling a given monthly LUE term with daily varying absorbed light levels should lead to an overestimation of assimilation rates at high light levels. This overestimation should disappear as the time scale over which light levels are averaged is increased. However, our results do not confirm these expectations (Fig. 12). The fact that the model did not exhibit a systematic error in simulating GPP variations when applied at the daily time scale is probably due to the fact that day-to-day variability in light levels is relatively small compared to the within-day variability and the non-linearity between  $A$  and daily varying light levels does not play an important role.

## 6 Conclusions

The P-model provides a simple, parameter-sparse but powerful method to predict photosynthetic capacity and light use efficiency across a wide range of climatic conditions and vegetation types. It provides a basis for a terrestrial light use efficiency



585 model driven by remotely sensed vegetation greenness. Using optimality principles for the formulation of the P-model reduces its dependence on uncertain or vegetation type-specific parameters and enables robust predictions of GPP and its variations through the seasons, between years, and across space. Further work is required to develop a distinct treatment of  $C_4$  vegetation for global applications and additional evaluations are needed to examine the P-model's sensitivity to increasing  $CO_2$ . We have shown that accounting for the effects of low soil moisture and the reduction in the quantum yield efficiency under low tem-  
590 peratures improves model performance. There is potential to include below-ground water limitation effects in the mechanistic optimality framework of the P-model.

*Code and data availability.* The P-model is implemented as an R package (*rpmodel*) and available through CRAN and Zenodo (Stocker, 2019a). Results shown here correspond to *rpmodel* version v1.0.4. A documentation of the R package is available under <https://stineb.github.io/rpmodel/>. Both site-scale and global simulations shown here are done with the Fortran implementation of the P-model within the SOFUN  
595 modelling framework (version v1.2.0), available on *Zenodo* (Stocker, 2019b). Site-scale forcing data ingest and filtering, model calibration, and evaluation was done using the R package *rsofun* (version v1.0.wrap\_sofun), available on *Zenodo* (Stocker, 2020b). Scripts that implement the workflow (repository *eval\_pmodel* version v2) are available on *Zenodo* (Stocker, 2020a). Model outputs are available on *Zenodo* (Stocker, 2019c).

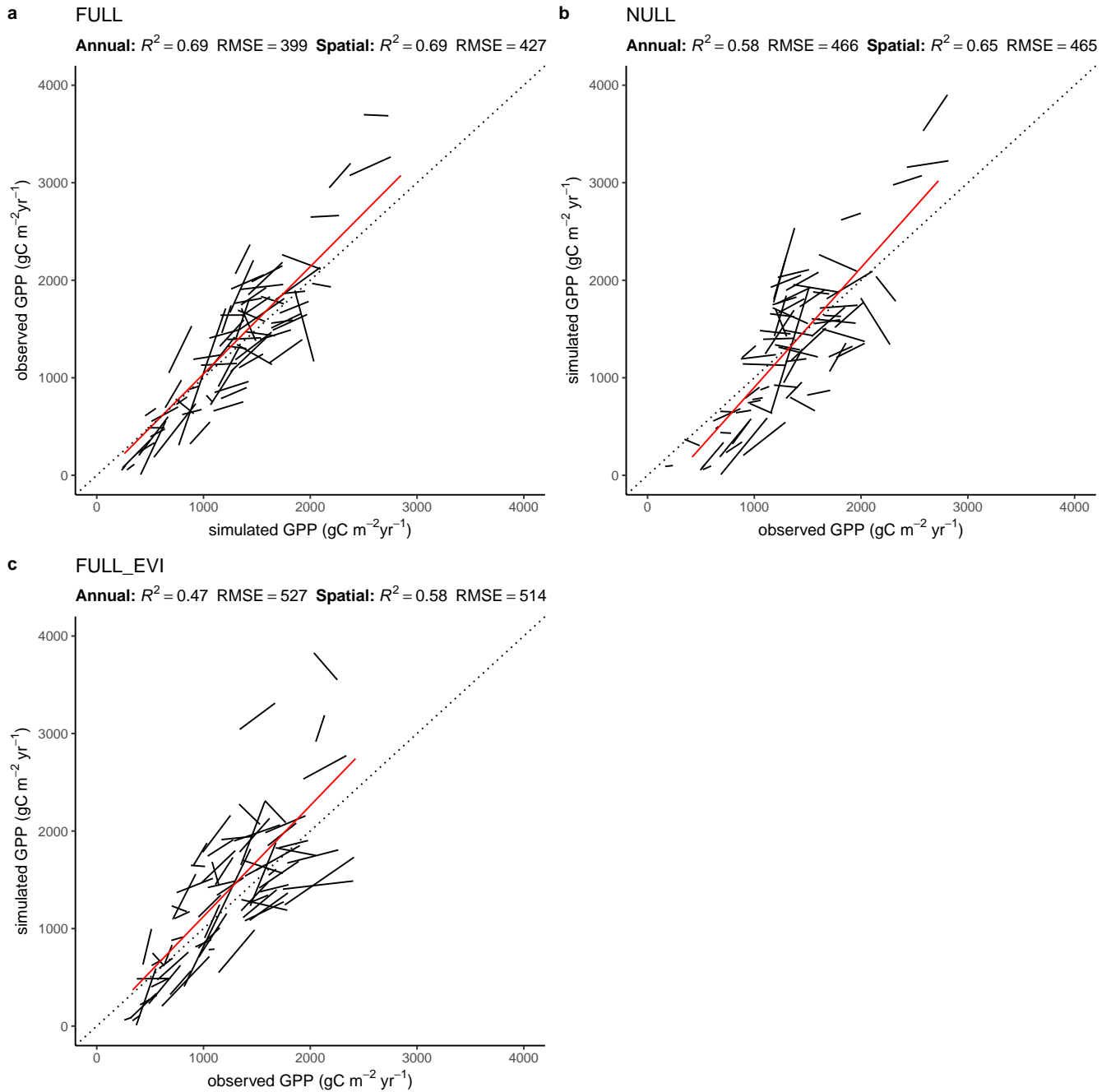


**Figure 5.** Correlation of modelled and observed annual GPP in simulations FULL (a), NULL (b) and FULL\_EVI (c). The red line and text are based on means across years by site and represents spatial (across-site) variations. Black lines and text are based on annual values, one line for each site. Lines represent linear regressions.  $R^2$  and RMSE statistics for annual values (black text) are based on pooled data from all sites. For a perfect fit between modelled and observed annual GPP values, all black lines (representing the linear regression model of annual values for a single site) would lie on the 1:1 line and have a slope of 1. Slopes that deviate substantially from 1, or even are negative, for some sites shows poor model performance in capturing inter-annual variability.

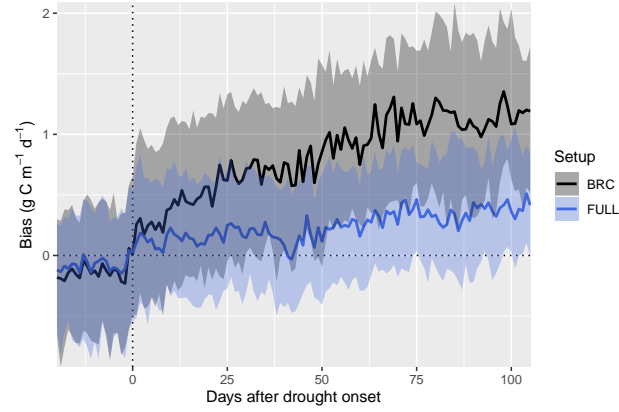


**Figure 6.** Bias in simulated GPP during the course of drought events. Simulated GPP is from a simulation with (FULL) and without (BRC) accounting for soil moisture stress. The timing of drought events is taken from Stocker et al. (2018) and is identified by an apparent soil moisture-related reduction of observed light use efficiency at 36 FLUXNET sites. The bias is calculated as simulated minus observed GPP. Data from multiple drought events and sites are aligned by the date of drought onset and aggregated across all sites and events (lines for medians, shaded ranges from the 33% and 66% quantiles).

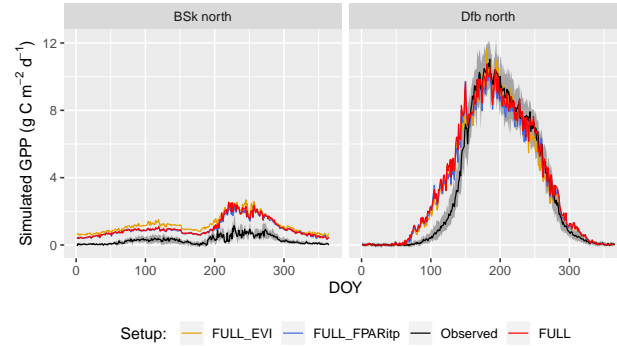


**Figure 7.** Mean seasonal cycle for model setups with different greenness forcing data for two climate zones (BSk and Dfb, both northern hemisphere). Observations are given by the black line and grey band, representing the median and 33/66 % quantiles by day-of-year (DOY) of all data (multiple sites and years) pooled by climate zone. Coloured lines represent model setups, forced with different greenness data. The annotation above each plot specifies the climate zone (see Tab. 2). Climate zones shown here are illustrative examples.

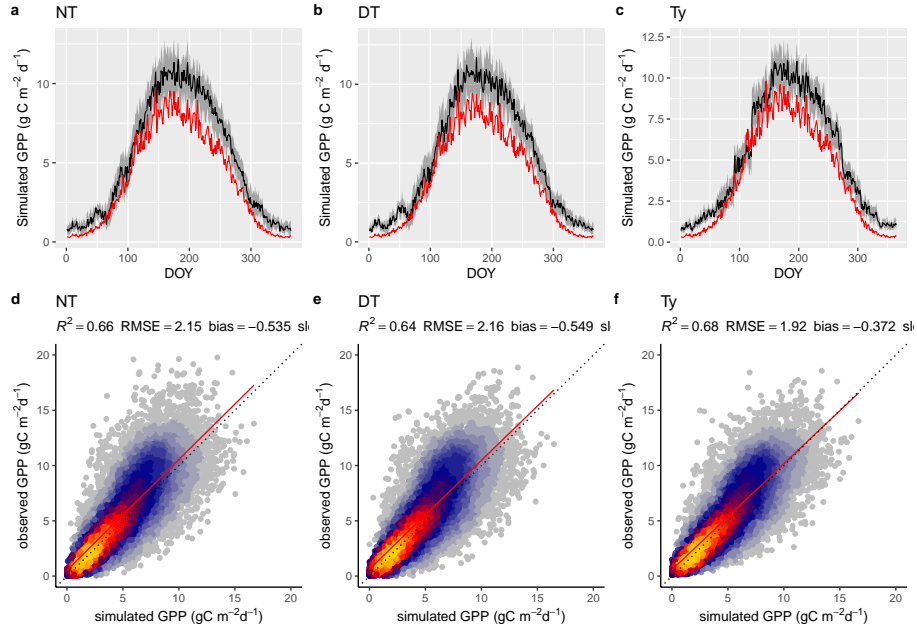


**Figure 8.** Model performance subject to comparison with different flux decomposition methods for GPP. (a-c): Mean seasonal cycle of simulated (red) and observed GPP (black) based on different flux decomposition methods for sites in climate zone Cfb north. The grey band represents the 33/66 % quantiles of observed GPP by day-of-year (DOY). (d-f): Correlation of observed and simulated GPP values of all sites pooled, mean over 8-day periods, all sites pooled. ‘Observed GPP’ refers to the different flux decomposition methods: DT for the daytime method (setup FULL\_DT), NT for the nighttime method (setup FULL\_NTsub) and Ty (setup FULL\_Ty) for the method applied for data used in Wang et al. (2017b). Dotted lines in (d-f) represent the 1:1 relationship, red lines represent the fitted linear regressions.

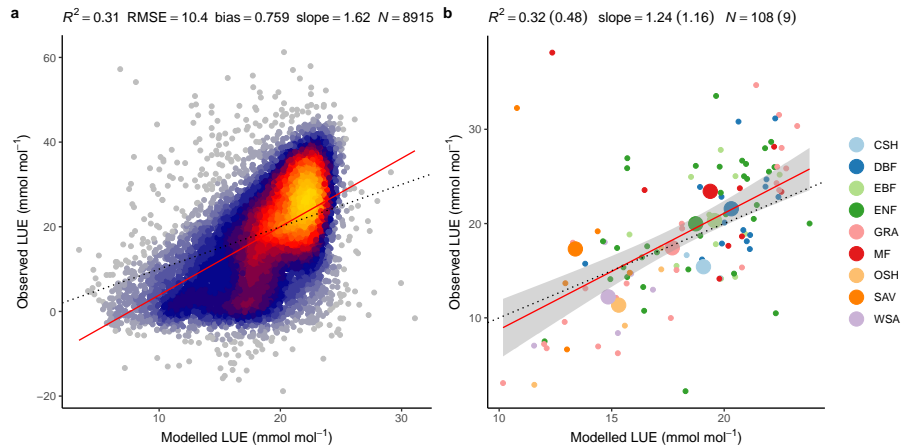


**Figure 9.** Modelled (simulations FULL) versus observed LUE. (a) Mean monthly LUE with data pooled from all sites and available years. (b) Mean annual LUE by site (small dots and color) and vegetation type (large dots and color). ee metrics are given at the top with numbers in brackets referring to the regression of data aggregated by vegetation types and non-bracketed numbers for data aggregated by sites. Dotted lines represent the 1:1 relationship, red lines represent the fitted linear regression to all data in (a) and to mean annual LUE by site in (b). The grey band in (b) represents the 95 % confidence interval of the linear regression. Vegetation types are: closed shrubland (CSH); deciduous broadleaf forest (DBF); evergreen broadleaf forest (EBF); evergreen needleleaf forest (ENF); grassland (GRA); mixed deciduous and evergreen needleleaf forest (MF); open shrubland (OSH); savanna ecosystem (SAV); woody savanna (WSA).

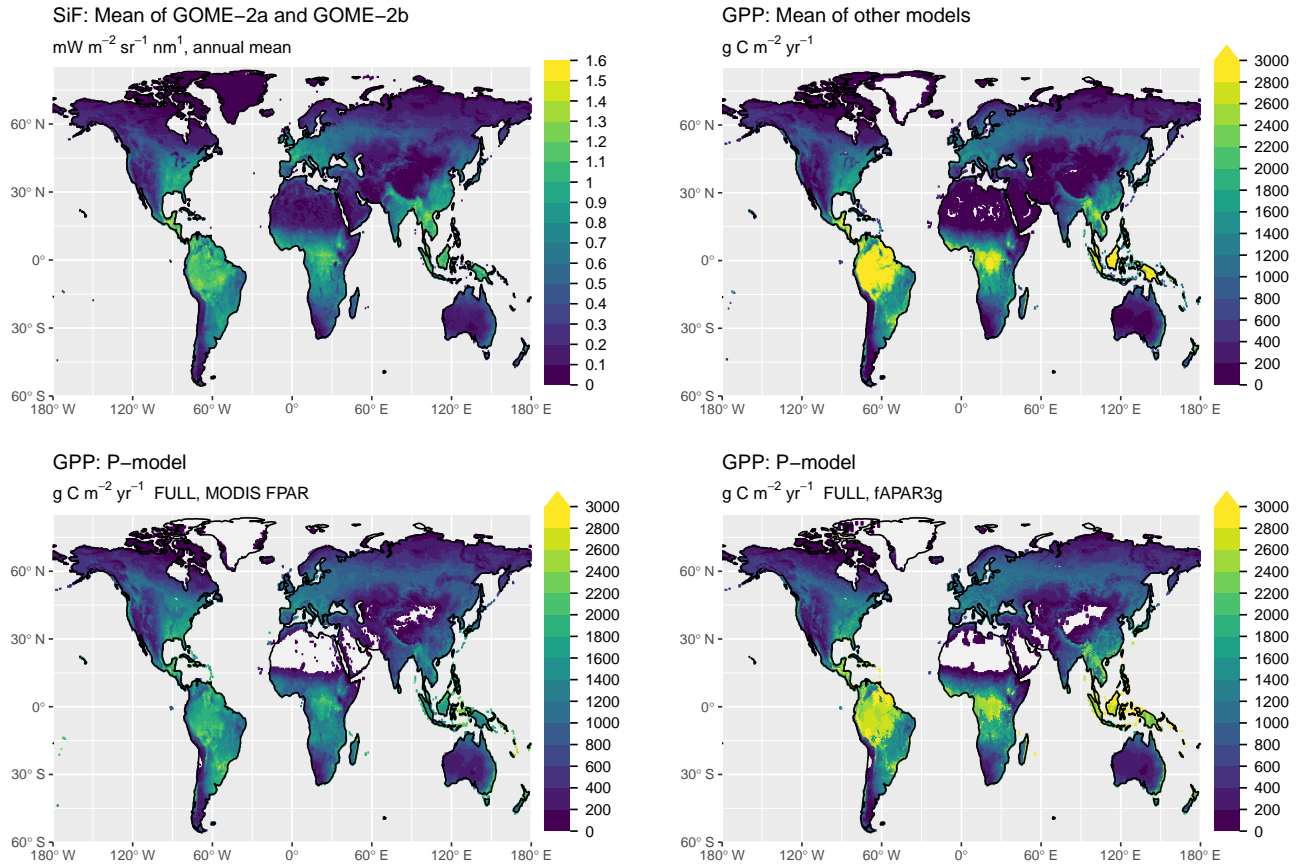


**Figure 10.** Global distribution of GPP. Shown are the mean annual values, averaged over years 2000 to 2016. The GPP shown as “mean of other models” is the average of MTE (Jung et al., 2011), FLUXCOM (‘RS+METEO’ setup) (Tramontana et al., 2016), MODIS GPP (collection 55 and 6) (Running et al., 2004; Zhao et al., 2005), BESS (Jiang and Ryu, 2016), BEPS (He et al., 2018; Chen et al., 2016), and VPM (Zhang et al., 2017b). P-model results are from simulations with the FULL setup and calibrated parameters as given in Table 1.

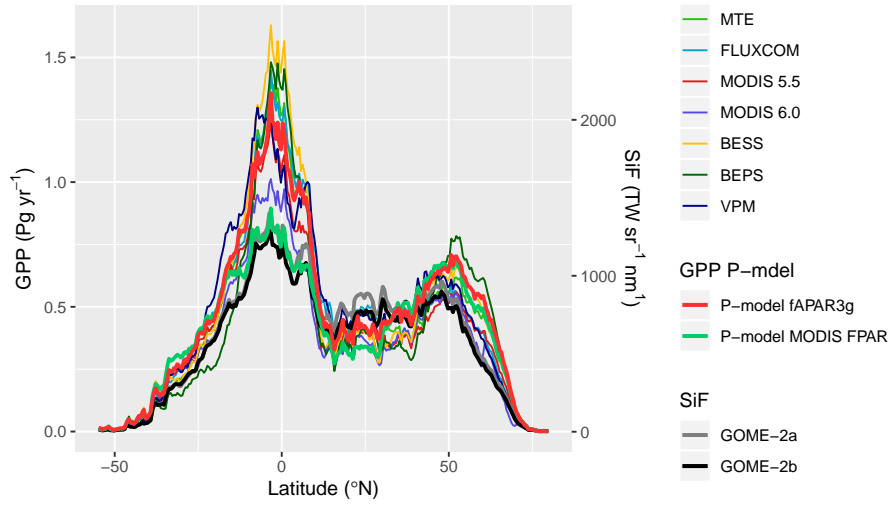


**Figure 11.** Latitudinal distribution of GPP and SiF. Values shown (GPP on the left y-axis, SiF on the right y-axis) are gridcell area-weighted sums along  $0.5^\circ$  latitudinal bands.

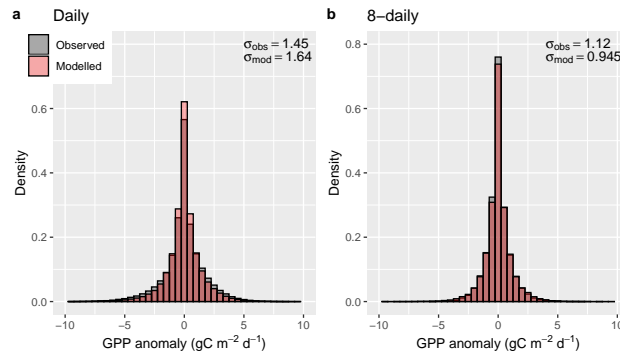


**Figure 12.** Distribution of anomalies from the mean seasonal cycle, evaluated for daily values (a) and 8-day means (b).

## Appendix A: Site information

600 Table A1 provides meata information and references for each site from the FLUXNET2015 Tier 1 dataset, used for model calibration and evaluation in the present study.

## Appendix B: Temperature and pressure dependence of photosynthesis parameters

### B1 Photorespiratory Compensation Point $\Gamma^*$

The temperature and pressure-dependent photorespiratory compensation point in absence of dark respiration  $\Gamma^*(T, p)$  is calcu-  
605 lated from its value at standard temperature ( $T_0 = 25^\circ\text{C}$ ) and atmospheric pressure ( $p_0 = 101325 \text{ Pa}$ ), referred to as  $\Gamma_{25, p_0}^*$ . It is modified by temperature following an Arrhenius-type temperature response function  $f_{\text{Arrh}}(T_K, \Delta H_{\Gamma^*})$  with activation energy  $\Delta H_{\Gamma^*}$ , and is corrected for atmospheric pressure  $p(z)$  at elevation  $z$ .

$$\Gamma^*(T_K, z) = \Gamma_{25, p_0}^* f_{\text{Arrh}}(T_K, \Delta H_{\Gamma^*}) \frac{p(z)}{p_0} \quad (\text{B1})$$

Values of  $\Delta H_{\Gamma^*}$  and  $\Gamma_{25, p_0}^*$  are taken from Bernacchi et al. (2001). The latter is converted to Pa and standardised to  $p_0$   
610 simply by multiplication with  $p_0$  ( $\Gamma_{25, p_0}^* = 42.75 \mu\text{mol mol}^{-1} \cdot 10^{-6} \cdot 101325 \text{ Pa} = 4.332 \text{ Pa}$ ).  $\Delta H_{\Gamma^*}$  is  $37830 \text{ J mol}^{-1}$ . All parameter values are summarised in Tab. A7. The function  $p(z)$  is defined in Sec B4. Note that  $T_K$  indicates that the respective temperature value is given in Kelvin and  $T_{K,0} = 298.15 \text{ K}$ .

To correct for effects by temperature following the Arrhenius Equation with its form  $x(T_K) = \exp(c - \Delta H_a / (T_K R))$ , the temperature-correction function  $f_{\text{Arrh}}(T_K, \Delta H_a)$ , used in Eq. B1 and further equations below, is given by:

$$615 \quad f_{\text{Arrh}}(T_K) = x(T_K) / x(T_{K,0}) = \exp\left(\frac{\Delta H(T_K - T_{K,0})}{T_{K,0} R T_K}\right) \quad (\text{B2})$$

where  $\Delta H$  is the respective activation energy (e.g.,  $\Delta H_{\Gamma^*}$  in Eq. B1), and  $R$  is the universal gas constant ( $8.3145 \text{ J mol}^{-1} \text{ K}^{-1}$ ).

### B2 Deriving $\Gamma^*$

The temperature and pressure dependency of  $\Gamma^*$  follows from the temperature dependencies of  $K_c$ ,  $K_o$ ,  $V_{c,\text{max}}$ , and  $V_{o,\text{max}}$  and  
620 the pressure dependency of  $pO_2(p)$ :

$$\Gamma^*(T_K, p) = \frac{pO_2(p) K_c(T_K) V_{\text{omax}}(T_K)}{2 K_o(T_K) V_{\text{cmax}}(T_K)} \quad (\text{B3})$$

$pO_2(p)$  is the partial pressure of atmospheric oxygen (Pa) and scales linearly with  $p(z)$ .  $K_c$  is the Michaelis-Menten constant for carboxylation (Pa);  $K_o$  is the Michaelis-Menten constant for oxygenation (Pa);  $V_{\text{cmax}}$  is maximum rate of carboxylation ( $\mu\text{mol m}^{-2} \text{ s}^{-1}$ ); and  $V_{\text{omax}}$  is the maximum rate of oxygenation ( $\mu\text{mol m}^{-2} \text{ s}^{-1}$ ). The temperature-dependency equations for  
625 these four terms are given in Table 1 of Bernacchi et al. (2001) with respective scaling constants  $c$  and activation energies  $\Delta H_a$



as :

$$K_c(T_K) = \exp(38.05 - 79.43/(T_K R)) \quad (\text{B4a})$$

$$K_o(T_K) = 1000 \cdot \exp(20.30 - 36.38/(T_K R)) \quad (\text{B4b})$$

$$V_{o,\max}(T_K) = \exp(22.98 - 60.11/(T_K R)) \quad (\text{B4c})$$

$$630 \quad V_{c,\max}(T_K) = \exp(26.35 - 65.33/(T_K R)) \quad (\text{B4d})$$

By substituting the temperature-dependency equations for each term in Eq. B3 and rearranging terms,  $\Gamma^*$  can be written as

$$\Gamma^*(T_K, z) = pO_2(z) \exp(6.779 - 37.83/(T_K R)) . \quad (\text{B5})$$

With  $pO_2(p)$  at standard atmospheric pressure (101325 Pa) taken to be 21000 Pa, and assuming a constant mixing ratio across the troposphere, its pressure dependence can be expressed as

$$635 \quad pO_2(p) = 0.2095 \cdot p(z) \quad (\text{B6})$$

hence

$$\Gamma^*(T_K, p) = p(z) \exp(5.205 - 37.83/(T_K R)) \quad (\text{B7})$$

We can use this to calculate  $\Gamma^*$  at standard temperature ( $T_K = 298.15$  K) and pressure ( $p(z) = 101325$  Pa) as  $\Gamma_{25,p_0}^* = 4.332$  Pa.

640 Note that to convert Eq. B5 to the form corresponding to the one given by Bernacchi et al. (2001), the partial pressure of oxygen ( $pO_2$ ) has to be assumed at standard conditions.  $pO_2$  is approximately 21000 Pa and with the standard atmospheric pressure of 101325 Pa,  $pO_2$  can be converted from Pascals to parts-per-million (ppm) as  $21000/101325 \times 10^6 = 207254$  ppm =  $\exp(12.24)$  ppm. This can be combined with the exponent in Eq. B5 to  $\exp(12.24) \cdot \exp(6.779) = \exp(19.02)$ . This corresponds to the parameter values determining the temperature dependence of  $\Gamma^*$  given by Bernacchi et al. (2001) as  $\Gamma^* =$

645  $\exp(19.02 - 37.83/(T_K R))$ .

### B3 Michaelis-Menten Coefficient of Photosynthesis

The effective Michaelis-Menten coefficient  $K$  (Pa) of Rubisco-limited photosynthesis (Eq. 6) is determined by the Michaelis-Menten constants for the carboxylation and oxygenation reactions (Farquhar et al., 1980):

$$K(T_K, p) = K_c(T_K) \left( 1 + \frac{pO_2(p)}{K_o(T_K)} \right) , \quad (\text{B8})$$

650 where  $K_c$  is the Michaelis-Menten constant for  $\text{CO}_2$  (Pa),  $K_o$  is the Michaelis-Menten constant for the carboxylation and oxygenation reaction, respectively, and  $pO_2$  is the partial pressure of oxygen (Pa).  $K_c$  and  $K_o$  follow a temperature dependence, given by the Arrhenius equation analogously to the temperature dependence of  $\Gamma^*$  (Eq. B1):

$$K_c(T_K) = K_{c25} f_{\text{Arrh}}(T_K, \Delta H_{K_c}) \quad (\text{B9a})$$

$$K_o(T_K) = K_{o25} f_{\text{Arrh}}(T_K, \Delta H_{K_o}) \quad (\text{B9b})$$

655 Values  $\Delta H_{Kc} = 79430 \text{ J mol}^{-1}$ ,  $\Delta H_{Ko} = 36380 \text{ J mol}^{-1}$ ,  $K_{c25} = 39.97 \text{ Pa}$ , and  $K_{o25} = 27480 \text{ Pa}$  are taken from Bernacchi et al. (2001) and (see also Tab. A7). The latter two have been converted from  $\mu\text{mol mol}^{-1}$  in Bernacchi et al. (2001) to units of Pa by multiplication with the standard atmosphere (101325 Pa). Note that  $K_{c25}$  and  $K_{o25}$  are rate constants and are independent of atmospheric pressure. Pressure-dependence of  $K$  is solely in  $pO_2(p)$  (see Eq. B6).

#### B4 Atmospheric pressure

660 The elevation-dependence of atmospheric pressure is computed by assuming a linear decrease in temperature with elevation and a mean adiabatic lapse rate (Berberan-Santos et al., 1997):

$$p(z) = p_0 \left( 1 - \frac{Lz}{T_{K,0}} \right)^{gM_a(RL)^{-1}}, \quad (\text{B10})$$

where  $z$  is the elevation above mean sea level (m),  $g$  is the gravitational constant ( $9.80665 \text{ m s}^{-2}$ ),  $p_0$  is the standard atmospheric pressure at 0 m a.s.l. (101325 Pa),  $L$  is the mean adiabatic lapse rate ( $0.0065 \text{ K m}^{-2}$ ),  $M_a$  is the molecular weight for dry air (0.028963 kg mol<sup>-1</sup>), and  $R$  is the universal gas constant ( $8.3145 \text{ J mol}^{-1} \text{ K}^{-1}$ ). All parameter values that are held fixed in the model (not calibrated) are summarised in Tab. A7.

### Appendix C: Corollary of the $\chi$ prediction

#### C1 Stomatal conductance

Stomatal conductance  $g_s$  (mol C Pa<sup>-1</sup>) follows from the prediction of  $\chi$  given by Eq. 8 and  $g_s = A/(c_a(1 - \chi))$  (from Eq. 5).  
670 Stomatal conductance can thus be written as

$$g_s = \left( 1 + \frac{\xi}{\sqrt{D}} \right) \frac{A}{c_a - \Gamma^*}. \quad (\text{C1})$$

This has a similar form as the solution for  $g_s$  derived from a different optimality principle by Medlyn et al. (2011) (their Eq. 11). Differences are that an additional term  $g_0$  is missing here and that  $\Gamma^*$  does not appear in Medlyn et al. (2011). The theory presented by Prentice et al. (2014) provides a theoretical interpretation for the parameter  $g_1$  in Medlyn et al. (2011): It is given  
675 by  $\xi$  (Eq. 9) and can thus be predicted from the environment. However, it is notable that the underlying optimality criterion used by Medlyn et al. (2011), as proposed by Cowan and Farquhar (1977), is one that maintains a constant marginal water cost of carbon gain  $\lambda = \partial E / \partial A$ . It thus describes an instantaneous  $g_s$  adjustment, e.g., to diurnal variations in  $D$  and has been adopted into DVMs and ESMs for respective predictions (with a given  $V_{\text{cmax}}$ ). In contrast, the theory presented here and underlying the P-model predicts  $\chi$  which is jointly controlled by  $g_s$  and  $V_{\text{cmax}}$ . In other words, it predicts a  $g_s$  that is coordinated with  $V_{\text{cmax}}$   
680 and thus acclimates at a similar time scale (which is on the order of days to weeks). This  $\chi$  can be understood as a “set-point” for an average  $\chi$  with actual  $\chi$  varying around it at a daily to sub-daily time scale.

## C2 Intrinsic water use efficiency

The intrinsic water use efficiency (iWUE, in Pa) has been defined as the ratio of assimilation over stomatal conductance (to water) (Beer et al., 2009) as  $iWUE = A/(1.6g_s)$ . The factor 1.6 accounts for the difference in diffusivity between CO<sub>2</sub> and H<sub>2</sub>O. Using Fick's Law (Eq. 5), this is simply

$$iWUE = \frac{c_a(1 - \chi)}{1.6}, \quad (C2)$$

or, using the prediction of optimal  $\chi$  given by Eq. 8, this can be expressed as

$$iWUE = \frac{1}{1.6 \left(1 + \frac{\xi}{\sqrt{D}}\right)} (c_a - \Gamma^*) \quad (C3)$$

## C3 Maximum carboxylation capacity

690  $V_{\text{cmax}}$  With  $A_J = A_C$ ,  $V_{\text{cmax}}$  can directly be derived as

$$V_{\text{cmax}} = \varphi_0 I_{\text{abs}} \frac{c_i + K}{c_i + 2\Gamma^*} = \varphi_0 I_{\text{abs}} \frac{m}{m_C}, \quad (C4)$$

$c_i$  is given by  $c_a\chi$ . The second part of the equation follows from the definitions of  $m$  (Eq. 11) and  $m_C$  (Eq. 7). Normalising  $V_{\text{cmax}}$  to standard temperature (25°C) following a modified Arrhenius function based on Kattge and Knorr (2007) gives  $V_{\text{cmax}25}$  as

$$695 \quad V_{\text{cmax}25} = V_{\text{cmax}}/f_V(T_K, T_{K,0}) \quad (C5)$$

$$f_V(T_K, T_{K,0}) = f_{\text{Arrh}}(T_K, \Delta H_V) \cdot \frac{1 + \exp((T_{K,0}\Delta S - H_d)/(T_{K,0}R))}{1 + \exp((T_K\Delta S - H_d)/(T_K R))} \quad (C6)$$

with  $H_V$  being the activation energy (71513 J mol<sup>-1</sup>),  $H_d$  is the deactivation energy (200000 J mol<sup>-1</sup>), and  $\Delta S$  is an entropy term (J mol<sup>-1</sup> K<sup>-1</sup>) calculated using a linear relationship with  $T$  from Kattge and Knorr (2007), with a slope of  $b_S = 1.07$  J mol<sup>-1</sup> K<sup>-2</sup> and intercept of  $a_S = 668.39$  J mol<sup>-1</sup> K<sup>-1</sup>:

$$700 \quad \Delta S = a_S - b_S T \quad (C7)$$

Note that  $T$  is in units of °C in above equation. Equation C6 describes the *instantaneous* response to temperature and is not the same as the optimality-driven *acclimation* to temperature predicted by the P-model.

## C4 Dark respiration $R_d$

Dark respiration at standard temperature  $R_{d25}$  is calculated as being proportional to  $V_{\text{cmax}25}$ :

$$705 \quad R_{d25} = b_0 V_{\text{cmax}25} \quad (C8)$$

where  $b_0 = 0.015$  (Atkin et al., 2015). Dark respiration follows a slightly different instantaneous temperature sensitivity than  $V_{\text{cmax}}$  following Heskell et al. (2016):

$$R_d = R_{d25} f_R \quad (\text{C9})$$

$$f_R = \exp(0.1012(T_{K,0} - T_K) - 0.0005(T_{K,0}^2 - T_K^2)) \quad (\text{C10})$$

710 By combining Eqs. C6, C8, and C9,  $R_d$  at growth temperature  $T$  can directly be calculated from  $V_{\text{cmax}}$  as

$$R_d = b_0 \frac{f_R}{f_V} V_{\text{cmax}} \quad (\text{C11})$$

#### Appendix D: Soil water holding capacity

The soil water balance is solved following the SPLASH model but with the total soil water holding capacity per unit ground area ( $\theta_{\text{WHC}}$ , in mm) calculated as a function of the soil texture. Precipitation in the form of rain ( $P_{\text{rain}}$ ) and snow ( $P_{\text{snow}}$ ) are taken from WATCH-WFDEI (Weedon et al., 2014) and are summed and converted from  $\text{kg m}^{-2} \text{s}^{-1}$  to  $\text{mm d}^{-1}$  by multiplication with  $(60 \cdot 60 \cdot 24) \text{ s d}^{-1}$ . To obtain  $\theta_{\text{WHC}}$ , we use soil depth-to-bedrock and texture data from SoilGrids (Hengl et al., 2014), extracted around the FLUXNET sites. We assumed that the plant-available WHC is determined by the WHC down to a maximum depth of 2 m and is limited by the depth to bedrock. The water holding capacity ( $w_{\text{WHC}}$ , in mm) was defined as the difference in volumetric soil water storage at field capacity ( $W_{\text{FC}}$ , in  $\text{m}^3 \text{m}^{-3}$ ) and the permanent wilting point

720 ( $W_{\text{PWP}}$ , in  $\text{m}^3 \text{m}^{-3}$ ):

$$\theta_{\text{WHC}} = (W_{\text{FC}} - W_{\text{PWP}}) (1 - f_{\text{gravel}}) \cdot \min(z_{\text{bedrock}}, z_{\text{max}}) \quad (\text{D1})$$

$f_{\text{gravel}}$  is the gravel fraction,  $z_{\text{bedrock}}$  is the depth to bedrock (in mm), and  $z_{\text{max}}$  is 2000 mm. The volumetric soil water storage at field capacity and wilting point were derived from texture and organic matter content data through pedotransfer functions, as described by Saxton and Rawls (2006).  $W_{\text{FC}}$  is calculated as:

$$725 \quad W_{\text{FC}} = k_{\text{FC}} + (1.283 \cdot k_{\text{FC}}^2 - 0.374 \cdot k_{\text{FC}} - 0.015), \quad (\text{D2})$$

where

$$k_{\text{FC}} = -0.251 \cdot f_{\text{sand}} + 0.195 \cdot f_{\text{clay}} + 0.011 \cdot f_{\text{OM}} \quad (\text{D3})$$

$$+ 0.006 \cdot (f_{\text{sand}} f_{\text{OM}}) \quad (\text{D4})$$

$$- 0.027 \cdot (f_{\text{clay}} f_{\text{OM}}) \quad (\text{D5})$$

$$730 \quad + 0.452 \cdot (f_{\text{sand}} f_{\text{clay}}) \quad (\text{D6})$$

$$+ 0.299 \quad (\text{D7})$$

$f_{\text{sand}}$ ,  $f_{\text{clay}}$ ,  $f_{\text{OM}}$  are the sand, clay and organic matter contents in percent by weight.  $W_{\text{PWP}}$  is calculated as:

$$W_{\text{PWP}} = k_{\text{PWP}} + (0.14 \cdot k_{\text{PWP}} - 0.02), \quad (\text{D8})$$

where

$$k_{\text{PWP}} = -0.024 \cdot f_{\text{sand}} + 0.487 \cdot f_{\text{clay}} + 0.006 \cdot f_{\text{OM}} \quad (\text{D9})$$

$$+ 0.005 \cdot (f_{\text{sand}} f_{\text{OM}}) \quad (\text{D10})$$

$$- 0.013 \cdot (f_{\text{clay}} f_{\text{OM}}) \quad (\text{D11})$$

$$+ 0.068 \cdot (f_{\text{sand}} f_{\text{clay}}) \quad (\text{D12})$$

$$+ 0.031 \quad (\text{D13})$$

## 740 Appendix E: Vapour pressure Deficit

Vapour pressure deficit ( $D$ ) is calculated from specific humidity ( $q_{\text{air}}$ ) as:

$$D = e_{\text{sat}} - e_{\text{act}} , \quad (\text{E1})$$

with

$$e_{\text{sat}} = 611.0 \cdot \exp\left(\frac{17.27 T}{T + 237.3}\right) \quad (\text{E2})$$

745 and

$$e_{\text{act}} = \frac{p(z) w_{\text{air}} R_v}{R_d + w_{\text{air}} R_v} . \quad (\text{E3})$$

$p(z)$  is atmospheric pressure, taken here as a constant function of elevation  $z$  (Sec. B4),  $w_{\text{air}}$  is the mass mixing ratio of water vapor to dry air (dimensionless) and derived from specific humidity as  $w_{\text{air}} = q_{\text{air}}/(1 - q_{\text{air}})$ .  $R_d$  and  $R_v$  are the specific gas constants of dry air and water vapour, respectively and are given by  $R/M_d$  and  $R/M_v$ , respectively; where  $R$  is the universal gas constant (8.314 J mol<sup>-1</sup> K<sup>-1</sup>) and  $M_d$  (28.963 g mol<sup>-1</sup>) and  $M_v$  (18.02 g mol<sup>-1</sup>) are the molecular mass of dry air of water vapour, respectively.  $T$  is air temperature in °C.

## Appendix F: Extended theory

### F1 Deriving $\chi$

Using Eqs. 4 and 5, the term on the left-hand side of Eq. 3 can thus be written as

$$755 \quad \frac{\partial(E/A)}{\partial\chi} = \frac{1.6 D}{c_a (1 - \chi)^2} . \quad (\text{F1})$$

Using Equation 6 and the simplification  $\Gamma^* = 0$ , the derivative term on the right-hand-side of Eq.3 can be written as

$$\frac{\partial(V_{\text{cmax}}/A)}{\partial\chi} = -\frac{K}{c_a \chi^2} . \quad (\text{F2})$$

Eq. 3 can thus be written as

$$a \frac{1.6 D}{c_a (1 - \chi)^2} = b \frac{K}{c_a \chi^2} \quad (\text{F3})$$

760 and solved for  $\chi$ :

$$\chi = \frac{\xi}{\xi + \sqrt{D}} \quad (\text{F4})$$

$$\xi = \sqrt{\frac{\beta K}{1.6 \eta^*}} \quad (\text{F5})$$

Where  $b/a = \beta/\eta^*$ . The exact solution, without the simplification  $\Gamma^* = 0$ , and following analogous steps, is

$$\chi = \frac{\Gamma^*}{c_a} + \left(1 - \frac{\Gamma^*}{c_a}\right) \frac{\xi}{\xi + \sqrt{D}} \quad (\text{F6})$$

$$765 \quad \xi = \sqrt{\frac{b(K + \Gamma^*)}{1.6 a}} \quad (\text{F7})$$

This can also be written as

$$c_i = \frac{\Gamma^* \sqrt{D} + \xi c_a}{\xi + \sqrt{D}} . \quad (\text{F8})$$

## F2 Deriving the $J_{\max}$ limitation factor

By taking the derivative of  $A_J$  with respect to  $J_{\max}$ , Eq. 14 can be expressed as

$$770 \quad c = \frac{m(\varphi_0 I_{\text{abs}})^3}{4 \sqrt{[(\varphi_0 I_{\text{abs}})^2 + (\frac{J_{\max}}{4})^2]^3}} \quad (\text{F9})$$

This can be re-arranged to

$$\left(\frac{4c}{m}\right)^{2/3} = \frac{1}{1 + \left(\frac{J_{\max}}{4\varphi_0 I_{\text{abs}}}\right)^2} \quad (\text{F10})$$

For simplification, we can substitute

$$k = \frac{4\varphi_0 I_{\text{abs}}}{J_{\max}} \quad (\text{F11})$$

775 and

$$u = \left(\frac{4c}{m}\right)^{2/3} \quad (\text{F12})$$

With this, we can write

$$\frac{1}{1 + k^{-2}} = u . \quad (\text{F13})$$

This can be re-arranged to

$$(1 - u)^{1/2} = \frac{1}{\sqrt{1 + k^2}} \quad (F14)$$

The right-hand term now corresponds to the  $J_{\max}$  limitation factor  $L$  in Eq. 13, and we get Eq. 15.

To sum up, the P-model calculates GPP as

$$\text{GPP} = I_{\text{abs}} \varphi_0(T) \beta(\theta) m' M_C, \quad (F15)$$

where

$$m' = m \sqrt{1 - \left(\frac{c^*}{m}\right)^{2/3}} \quad (F16)$$

and

$$m = \frac{c_a - \Gamma^*}{c_a + 2\Gamma^* + 3\Gamma^* \sqrt{\frac{1.6\eta^* D}{\beta(K + \Gamma^*)}}} . \quad (F17)$$

$I_{\text{abs}}$  is the absorbed light (taken as fAPAR·PPFD, mol m<sup>-2</sup>),  $\varphi_0(T)$  is the temperature-dependent intrinsic quantum yield,  $\beta(\theta)$  is the soil moisture stress factor, and  $M_C$  is the molar mass of carbon (g mol<sup>-1</sup>).

### 790 F3 An alternative method for introducing the $J_{\max}$ limitation

Sect. 2.2 introduced the effect of a finite  $J_{\max}$  leading to a saturating relationship between absorbed light and the light-limited assimilation rate  $A_J$ . An alternative method was presented by Smith et al. (2019) and is implemented in *rpmodel* as an optional method (argument `method_jmaxlim = "smith19"`). Following their approach, the light-limited assimilation rate is described as

$$A_J = \left(\frac{J}{4}\right) m. \quad (F18)$$

$m$  is the CO<sub>2</sub> limitation factor (Eq. 11), and  $J$  is a saturating function of absorbed light, approaching  $J_{\max}$  for high light levels, following Farquhar et al. (1980):

$$\theta J^2 - (\varphi_0 I_{\text{abs}} + J_{\max}) J + \varphi_0 I_{\text{abs}} J_{\max} = 0. \quad (F19)$$

$\theta$  is a unitless parameter determining the curvature of the response of  $J$  to  $I_{\text{abs}}$ , here taken as 0.85, based on Smith et al. (2019)

800 and references therein. Eq. F19 can be substituted into Eq. F18 to yield

$$A_J = \left(\frac{m}{4}\right) \frac{\varphi_0 I_{\text{abs}} + J_{\max} \pm \sqrt{(\varphi_0 I_{\text{abs}} + J_{\max})^2 - 4\theta \varphi_0 I_{\text{abs}} J_{\max}}}{2\theta}, \quad (F20)$$

from which the smaller root is used to derive  $A_J$ . Similar as in the method used by Wang et al. (2017a) and outlined in Sect. 2.2, a proportionality between  $A_J$  and  $J_{\max}$  is assumed ( $\partial A / \partial J_{\max} = c$ ; Eq. 14). Taking the derivative of Eq. F20 with respect to  $J_{\max}$  and setting equal to  $c$  leads to

$$805 J_{\max} = \varphi_0 I_{\text{abs}} \omega \quad (F21)$$

with

$$\omega = -(1 - 2\theta) + \sqrt{(1 - \theta) \left( \frac{1}{\frac{4c}{m} (1 - \theta \frac{4c}{m})} - 4\theta \right)}. \quad (\text{F22})$$

Using this,  $A_J$  can be written analogously to Eq. 16, but with

$$m' = m \frac{\omega^*}{8\theta}, \quad (\text{F23})$$

810 and

$$\omega^* = 1 + \omega - \sqrt{(1 + \omega)^2 - 4\theta\omega}. \quad (\text{F24})$$

The cost parameter  $c$  was assumed to be non-varying. Under standard conditions of 25 °C, 101325 Pa atmospheric pressure, 1000 Pa vapor pressure deficit, and 360 ppm CO<sub>2</sub>, at which the ratio of  $J_{\max}$  to  $V_{\text{cmax}}$  was assumed to be 2.07 (Smith and Dukes, 2017),  $c$  was derived as 0.053 (Smith et al., 2019).

815 Using the definition of  $V_{\text{cmax}}$  from Eq. C4,  $m$  can be replaced by  $m'$  from Eq. F23 to calculate an “intermediate rate of  $V_{\text{cmax}}$ ” (Smith et al., 2019) as

$$V_{\text{cmax}} = \varphi_0 I_{\text{abs}} \frac{m'}{m_C} \quad (\text{F25})$$

## Appendix G: The `rpmodel()` function of the *rpmodel* R package

The *rpmodel* R package provides an implementation of the P-model as described here. The main function is `rpmodel()` which returns a list of variables that are mutually consistent within the theory of the P-model (Sect. 2) and based on calculations defined in this paper. References for the returned list of variables are given in Tab. A8



**Table A1.** Sites used for evaluation. Lon. is longitude, negative values indicate west longitude; Lat. is latitude, positive values indicate north latitude; Veg. is vegetation type: deciduous broadleaf forest (DBF); evergreen broadleaf forest (EBF); evergreen needleleaf forest (ENF); grassland (GRA); mixed deciduous and evergreen needleleaf forest (MF); savanna ecosystem (SAV); shrub ecosystem (SHR); wetland (WET).

Site	Lon.	Lat.	Period	Veg.	Clim.	N	Calib.	Reference
AR-SLu	-66.46	-33.46	2009-2011	MF	Bwk	448		Ulke et al. (2015)
AR-Vir	-56.19	-28.24	2009-2012	ENF	Csb	747	Y	Posse et al. (2016)
AT-Neu	11.32	47.12	2002-2012	GRA	Dfc	3709		Wohlfahrt et al. (2008)
AU-Ade	131.12	-13.08	2007-2009	WSA	Aw	532	Y	Beringer et al. (2011a)
AU-ASM	133.25	-22.28	2010-2013	ENF	BSh	953	Y	Cleverly et al. (2013)
AU-Cpr	140.59	-34.00	2010-2014	SAV	BSk	1412		Meyer et al. (2015)
AU-Cum	150.72	-33.61	2012-2014	EBF	Cfa	744		Beringer et al. (2016)
AU-DaP	131.32	-14.06	2007-2013	GRA	Aw	1820	Y	Beringer et al. (2011b)
AU-DaS	131.39	-14.16	2008-2014	SAV	Aw	2230	Y	Hutley et al. (2011)
AU-Dry	132.37	-15.26	2008-2014	SAV	Aw	1600	Y	Cernusak et al. (2011)
AU-Emr	148.47	-23.86	2011-2013	GRA	Bwk	812		Schroder et al. (2014)
AU-Gin	115.71	-31.38	2011-2014	WSA	Csa	942	Y	Beringer et al. (2016)
AU-GWW	120.65	-30.19	2013-2014	SAV	Bwk	664		Prober et al. (2012)
AU-Lox	140.66	-34.47	2008-2009	DBF	Bsh	273		Stevens et al. (2011)
AU-RDF	132.48	-14.56	2011-2013	WSA	Bwh	571		Bristow et al. (2016)
AU-Rig	145.58	-36.65	2011-2014	GRA	Cfb	1130		Beringer et al. (2016)
AU-Rob	145.63	-17.12	2014-2014	EBF	Csb	337		Beringer et al. (2016)
AU-Stp	133.35	-17.15	2008-2014	GRA	BSh	1951	Y	Beringer et al. (2011c)
AU-TTE	133.64	-22.29	2012-2013	OSH	BWh	475		Cleverly et al. (2016)
AU-Tum	148.15	-35.66	2001-2014	EBF	Cfb	4346		Leuning et al. (2005)
AU-Wac	145.19	-37.43	2005-2008	EBF	Cfb	976		Kilinc et al. (2013)
AU-Whr	145.03	-36.67	2011-2014	EBF	Cfb	1064	Y	McHugh et al. (2017)
AU-Wom	144.09	-37.42	2010-2012	EBF	Cfb	935	Y	Hinko-Najera et al. (2017)
AU-Ync	146.29	-34.99	2012-2014	GRA	BSk	475		Yee et al. (2015)
BE-Vie	6.00	50.31	1996-2014	MF	Cfb	4910	Y	Aubinet et al. (2001)
BR-Sa3	-54.97	-3.02	2000-2004	EBF	Am	1192		Wick et al. (2005)
CA-Man	-98.48	55.88	1994-2008	ENF	Dfc	1910		Dunn et al. (2007)

**Table A2.** Continued from Table A1

Site	Lon.	Lat.	Period	Veg.	Clim.	N	Calib.	Reference
CA-NS1	-98.48	55.88	2001-2005	ENF	Dfc	1067		NA
CA-NS2	-98.52	55.91	2001-2005	ENF	Dfc	1123		NA
CA-NS3	-98.38	55.91	2001-2005	ENF	Dfc	1395		NA
CA-NS4	-98.38	55.91	2002-2005	ENF	Dfc	756		NA
CA-NS5	-98.48	55.86	2001-2005	ENF	Dfc	1245		NA
CA-NS6	-98.96	55.92	2001-2005	OSH	Dfc	1190		NA
CA-NS7	-99.95	56.64	2002-2005	OSH	Dfc	929		NA
CA-Qfo	-74.34	49.69	2003-2010	ENF	Dfc	2416		Bergeron et al. (2007)
CA-SF1	-105.82	54.48	2003-2006	ENF	Dfc	526		NA
CA-SF2	-105.88	54.25	2001-2005	ENF	Dfc	676		NA
CA-SF3	-106.01	54.09	2001-2006	OSH	Dfc	660		NA
CH-Cha	8.41	47.21	2005-2014	GRA	Cfb	2944		Merbold et al. (2014)
CH-Dav	9.86	46.82	1997-2014	ENF	ET	4973		Zielis et al. (2014)
CH-Fru	8.54	47.12	2005-2014	GRA	Cfb	2861	Y	Imer et al. (2013)
CH-Lae	8.37	47.48	2004-2014	MF	Cfb	3551	Y	Etzold et al. (2011)
CH-Oel	7.73	47.29	2002-2008	GRA	Cfb	2184	Y	Ammann et al. (2009)
CN-Cha	128.10	42.40	2003-2005	MF	Dwb	1019		Guan et al. (2006)
CN-Cng	123.51	44.59	2007-2010	GRA	Bsh	1071	Y	NA
CN-Dan	91.07	30.50	2004-2005	GRA	ET	680		Shi et al. (2006)
CN-Din	112.54	23.17	2003-2005	EBF	Cfa	921		Yan et al. (2013)
CN-Du2	116.28	42.05	2006-2008	GRA	Dwb	595		Chen et al. (2009)
CN-HaM	101.18	37.37	2002-2004	GRA		949		Kato et al. (2006)
CN-Qia	115.06	26.74	2003-2005	ENF	Cfa	995	Y	Wen et al. (2010)
CN-Sw2	111.90	41.79	2010-2012	GRA	Bsh	382		Shao et al. (2017)
CZ-BK1	18.54	49.50	2004-2008	ENF	Dfb	1185		Acosta et al. (2013)
CZ-BK2	18.54	49.49	2004-2006	GRA	Dfb	163		NA
DE-Gri	13.51	50.95	2004-2014	GRA	Cfb	3642	Y	Prescher et al. (2010)
DE-Hai	10.45	51.08	2000-2012	DBF	Cfb	4247	Y	Knohl et al. (2003)
DE-Lkb	13.30	49.10	2009-2013	ENF	Cfb	1214		Lindauer et al. (2014)
DE-Obe	13.72	50.78	2008-2014	ENF	Cfb	2260	Y	NA
DE-RuR	6.30	50.62	2011-2014	GRA	Cfb	1227	Y	Post et al. (2015)

**Table A3.** Continued from Table A1

Site	Lon.	Lat.	Period	Veg.	Clim.	N	Calib.	Reference
DE-Tha	13.57	50.96	1996-2014	ENF	Cfb	5141	Y	Grünwald and Bernhofer (2007)
DK-Sor	11.64	55.49	1996-2014	DBF	Cfb	4936	Y	Pilegaard et al. (2011)
ES-LgS	-2.97	37.10	2007-2009	OSH	Csa	833		Reverter et al. (2010)
ES-Ln2	-3.48	36.97	2009-2009	OSH	Csa	182		Serrano-Ortiz et al. (2011)
FI-Hyy	24.30	61.85	1996-2014	ENF	Dfc	4857	Y	Suni et al. (2003)
FR-Fon	2.78	48.48	2005-2014	DBF	Cfb	3262	Y	Delpierre et al. (2015)
FR-LBr	-0.77	44.72	1996-2008	ENF	Cfb	2814	Y	Berbigier et al. (2001)
FR-Pue	3.60	43.74	2000-2014	EBF	Csa	4722	Y	Rambal et al. (2004)
GF-Guy	-52.92	5.28	2004-2014	EBF	Af	3609		Bonal et al. (2008)
IT-CA1	12.03	42.38	2011-2014	DBF	Csa	1036		Sabbatini et al. (2016)
IT-CA3	12.02	42.38	2011-2014	DBF	Csa	913		Sabbatini et al. (2016)
IT-Col	13.59	41.85	1996-2014	DBF	Cfa	3350	Y	Valentini et al. (1996)
IT-Cp2	12.36	41.70	2012-2014	EBF	Csa	764	Y	Fares et al. (2014)
IT-Isp	8.63	45.81	2013-2014	DBF	Cfb	641	Y	Ferréa et al. (2012)
IT-La2	11.29	45.95	2000-2002	ENF	Cfb	513		Marcolla et al. (2003a)
IT-Lav	11.28	45.96	2003-2014	ENF	Cfb	3947	Y	Marcolla et al. (2003b)
IT-MBo	11.05	46.01	2003-2013	GRA	Dfb	3682	Y	Marcolla et al. (2011)
IT-Noe	8.15	40.61	2004-2014	CSH	Cwb	3070	Y	Papale et al. (2014)
IT-PT1	9.06	45.20	2002-2004	DBF	Cfa	891	Y	Migliavacca et al. (2009)
IT-Ren	11.43	46.59	1998-2013	ENF	Dfc	3405	Y	Montagnani et al. (2009)
IT-Ro2	11.92	42.39	2002-2012	DBF	Csa	3113		Tedeschi et al. (2006)
IT-SR2	10.29	43.73	2013-2014	ENF	Csa	675	Y	Hoshika et al. (2017)
IT-SRo	10.28	43.73	1999-2012	ENF	Csa	3797	Y	Chiesi et al. (2005)
IT-Tor	7.58	45.84	2008-2014	GRA	Dfc	2172	Y	Galvagno et al. (2013)

**Table A4.** Continued from Table A1

Site	Lon.	Lat.	Period	Veg.	Clim.	N	Calib.	Reference
JP-MBF	142.32	44.39	2003-2005	DBF	Dfb	471		Matsumoto et al. (2008)
JP-SMF	137.08	35.26	2002-2006	MF	Cfa	1288	Y	Matsumoto et al. (2008)
NL-Hor	5.07	52.24	2004-2011	GRA	Cfb	2188	Y	Jacobs et al. (2007)
NL-Loo	5.74	52.17	1996-2013	ENF	Cfb	4671	Y	Moors (2012)
RU-Fyo	32.92	56.46	1998-2014	ENF	Dfb	4635	Y	Kurbatova et al. (2008)
RU-Ha1	90.00	54.73	2002-2004	GRA	Dfc	567		Marchesini et al. (2007)
SD-Dem	30.48	13.28	2005-2009	SAV	BWh	770	Y	Ardo et al. (2008)
SN-Dhr	-15.43	15.40	2010-2013	SAV	BWh	688	Y	Tagesson et al. (2014)
US-AR1	-99.42	36.43	2009-2012	GRA	Cfa	1060		NA
US-AR2	-99.60	36.64	2009-2012	GRA	Cfa	981		NA
US-ARb	-98.04	35.55	2005-2006	GRA	Cfa	542		NA
US-ARc	-98.04	35.55	2005-2006	GRA	Cfa	582		NA
US-Blo	-120.63	38.90	1997-2007	ENF	Csb	1859		Goldstein et al. (2000)
US-Cop	-109.39	38.09	2001-2007	GRA	BSk	1186		Bowling et al. (2010)
US-GBT	-106.24	41.37	1999-2006	ENF	Dfc	615		Zeller and Nikolov (2000)
US-GLE	-106.24	41.37	2004-2014	ENF	Dfb	3134	Y	Frank et al. (2014)
US-Ha1	-72.17	42.54	1991-2012	DBF	Dfb	3932	Y	Urbanski et al. (2007a)
US-KS2	-80.67	28.61	2003-2006	CSH	Cfa	1254		Powell et al. (2006)
US-Me1	-121.50	44.58	2004-2005	ENF	Csb	284		Irvine et al. (2007)
US-Me2	-121.56	44.45	2002-2014	ENF	Csb	3581	Y	Irvine et al. (2008)
US-Me6	-121.61	44.32	2010-2014	ENF	Csb	1298		Ruehr et al. (2012)
US-MMS	-86.41	39.32	1999-2014	DBF	Cfa	4865	Y	Dragoni et al. (2011)
US-NR1	-105.55	40.03	1998-2014	ENF	Dfc	5115		Monson et al. (2002)
US-PFa	-90.27	45.95	1995-2014	MF	Dfb	4749		Desai et al. (2015)
US-Prr	-147.49	65.12	2010-2013	ENF	Dfc	811		Nakai et al. (2013)

**Table A5.** Continued from Table A1

Site	Lon.	Lat.	Period	Veg.	Clim.	N	Calib.	Reference
US-SRG	-110.83	31.79	2008-2014	GRA	BSk	2117	Y	Scott et al. (2015a)
US-SRM	-110.87	31.82	2004-2014	WSA	BSk	3354	Y	Scott et al. (2009)
US-Syv	-89.35	46.24	2001-2014	MF	Dfb	2365	Y	Desai et al. (2005)
US-Ton	-120.97	38.43	2001-2014	WSA	Csa	4336	Y	Baldocchi et al. (2010)
US-UMB	-84.71	45.56	2000-2014	DBF	Dfb	4015	Y	Gough et al. (2013)
US-UMd	-84.70	45.56	2007-2014	DBF	Dfb	2050	Y	Gough et al. (2013)
US-Var	-120.95	38.41	2000-2014	GRA	Csa	4356	Y	Ma et al. (2007)
US-WCr	-90.08	45.81	1999-2014	DBF	Dfb	3425	Y	Cook et al. (2004)
US-Whs	-110.05	31.74	2007-2014	OSH	BSk	2233		Scott et al. (2015b)
US-Wi0	-91.08	46.62	2002-2002	ENF	Dfb	228		Noormets et al. (2007)
US-Wi3	-91.10	46.63	2002-2004	DBF	Dfb	415		Noormets et al. (2007)
US-Wi4	-91.17	46.74	2002-2005	ENF	Dfb	712	Y	Noormets et al. (2007)
US-Wi6	-91.30	46.62	2002-2003	OSH	Dfb	351		Noormets et al. (2007)
US-Wi9	-91.08	46.62	2004-2005	ENF	Dfb	302		Noormets et al. (2007)
US-Wkg	-109.94	31.74	2004-2014	GRA	BSk	3198		Scott et al. (2010)
ZA-Kru	31.50	-25.02	2000-2010	SAV	BSh	2439		Archibald et al. (2009)
ZM-Mon	23.25	-15.44	2000-2009	DBF	Aw	645	Y	Merbold et al. (2009)

**Table A6.** Fixed parameters. 'SC' stands for 'at standard conditions' (25 °C, 101325 Pa). 'MM coef.' refers to 'Michaelis Menten coefficient'.

Symbol	Value	Units	Description	Reference
$\beta$	146.0	1	Unit cost ratio, Eq. 3	This study
$\Gamma_{25,p_0}^*$	4.332	Pa	Photorespiratory compensation point, SC	Bernacchi et al. (2001)
$K_{c25}$	39.97	Pa	MM coef. for CO <sub>2</sub> , SC	Bernacchi et al. (2001)
$K_{o25}$	27480	Pa	MM coef. for O <sub>2</sub> , SC	Bernacchi et al. (2001)
$\Delta H_{\Gamma^*}$	37830	J mol <sup>-1</sup>	Activation energy for $\Gamma^*$	Bernacchi et al. (2001)
$\Delta H_{K_c}$	79430	J mol <sup>-1</sup>	Activation energy for $K_c$	Bernacchi et al. (2001)
$\Delta H_{K_o}$	36380	J mol <sup>-1</sup>	Activation energy for $K_o$	Bernacchi et al. (2001)
$H_V$	71513	J mol <sup>-1</sup>	Activation energy for $V_{\text{cmax}}$	Kattge and Knorr (2007)
$H_d$	200000	J mol <sup>-1</sup>	Deactivation energy for $V_{\text{cmax}}$	Kattge and Knorr (2007)
$p_0$	101325	Pa	Standard atmosphere	–
$g$	9.80665	m s <sup>-2</sup>	Gravitation constant	–
$L$	0.0065	K m <sup>-2</sup>	Adiabatic lapse rate	–
$R$	8.3145	J mol <sup>-1</sup> K <sup>-1</sup>	Universal gas constant	–
$M_a$	28.963	g mol <sup>-1</sup>	Molecular mass of dry air	–
$M_C$	12.0107	g mol <sup>-1</sup>	Molecular mass of carbon	–
$a_S$	668.39	J mol <sup>-1</sup> K <sup>-1</sup>	Intercept for entropy term in Eq. C6	Kattge and Knorr (2007)
$b_S$	1.07	J mol <sup>-1</sup> K <sup>-2</sup>	Slope for entropy term in Eq. C6	Kattge and Knorr (2007)

**Table A7.** Fixed parameters. 'SC' stands for 'at standard conditions' (25 °C, 101325 Pa). 'MM coef.' refers to 'Michaelis Menten coefficient'.

**Table A8.** Variables returned by the function `rpmodel()`. Variable names correspond to the named elements of the list returned by the `rpmodel()` function call. Symbols correspond to their use in this paper.

Variable name	Symbol	Description	Units	Reference
<code>ca</code>	$c_a$	Ambient CO <sub>2</sub> partial pressure	Pa	Sect. 2.1
<code>gammastar</code>	$\Gamma^*$	Photorespiratory compensation point	Pa	Sect. B1
<code>kmm</code>	$K$	Michaelis-Menten coefficient for photosynthesis	Pa	Sect. B3
<code>ns_star</code>	$\eta^*$	Change in the viscosity of water, relative to its value at 25 °C	unitless	Huber et al. (2009)
<code>chi</code>	$\chi$	Ratio of leaf internal-to-ambient CO <sub>2</sub>	unitless	Sect. 2.1
<code>ci</code>	$c_i$	Leaf internal CO <sub>2</sub> partial pressure	Pa	Eq. F8
<code>lue</code>	LUE	Light use efficiency	$\text{g C mol}^{-1}$	Eq. 19
<code>mj</code>	$m$	CO <sub>2</sub> limitation factor for light-limited assimilation	unitless	Eq. 11
<code>mc</code>	$m_C$	CO <sub>2</sub> limitation factor for Rubisco-limited assimilation	unitless	Eq. 7
<code>gpp</code>	GPP	Gross primary production	$\text{g C m}^{-2} \text{d}^{-1}$	Eqs. 2 and 19
<code>iwue</code>	iWUE	Intrinsic water use efficiency	Pa	Eq. C2
<code>gs</code>	$g_s$	Stomatal conductance	$\text{mol C m}^{-2} \text{d}^{-1} \text{Pa}^{-1}$	Sect. C1
<code>vcmax</code>	$V_{\text{cmax}}$	Maximum rate of carboxylation	$\text{mol C m}^{-2} \text{d}^{-1}$	Eq. C4
<code>vcmax25</code>	$V_{\text{cmax25}}$	Maximum rate of carboxylation, normalised to 25 °C	$\text{mol C m}^{-2} \text{d}^{-1}$	Eq. C5
<code>rd</code>	$R_d$	Dark respiration	$\text{mol C m}^{-2} \text{d}^{-1}$	Eq. C11

*Author contributions.* B.D.S. designed the study, wrote the model code, conducted the analysis, and wrote the paper. H. W. developed the model and wrote the an initial version of the model description. N.G.S. developed the model and implemented model code. S.P.H. contributed to designing the study and writing the manuscript. T.K. contributed to study design, model implementation and manuscript writing. D.S. implemented the water holding capacity model. T.D. wrote an initial version of the model code and model documentation. I.C.P. developed the model and contributed to designing the study.

*Competing interests.* The authors have no competing interests.

*Acknowledgements.* B.D.S. was funded by ERC H2020-MSCA-IF-2015, grant number 701329 and the Swiss National Science Foundation grant no. PCEFP2\_181115. N.G.S. acknowledges support from Texas Tech University. T.F.K. acknowledges support from the Laboratory Directed Research and Development (LDRD) fund under the auspices of DOE, BER Office of Science at Lawrence Berkeley National Laboratory, and the NASA Terrestrial Ecology Program IDS Award NNH17AE86I. S.P.H. acknowledges support from the ERC-funded project GC 2.0 (Global Change 2.0: Unlocking the past for a clearer future, grant number 694481). I.C.P. acknowledges support from the ERC under the European Union’s Horizon 2020 research and innovation programme (grant agreement no: 787203 REALM).



## References

- 835 Acosta, M., Pavelka, M., Montagnani, L., Kutsch, W., Lindroth, A., Juszczak, R., and Janouš, D.: Soil surface CO<sub>2</sub> efflux measurements in Norway spruce forests: Comparison between four different sites across Europe — from boreal to alpine forest, *Geoderma*, 192, 295–303, <https://doi.org/10.1016/j.geoderma.2012.08.027>, <https://doi.org/10.1016%2Fj.geoderma.2012.08.027>, 2013.
- Adams, W. W., Zarter, C. R., Ebbert, V., and Demmig-Adams, B.: Photoprotective Strategies of Overwintering Evergreens, *Bioscience*, 54, 41–49, 2004.
- 840 Ammann, C., Spirig, C., Leifeld, J., and Neftel, A.: Assessment of the nitrogen and carbon budget of two managed temperate grassland fields, *Agriculture, Ecosystems & Environment*, 133, 150–162, <https://doi.org/10.1016/j.agee.2009.05.006>, <https://doi.org/10.1016%2Fj.agee.2009.05.006>, 2009.
- Archibald, S. A., Kirton, A., van der Merwe, M. R., Scholes, R. J., Williams, C. A., and Hanan, N.: Drivers of inter-annual variability in Net Ecosystem Exchange in a semi-arid savanna ecosystem, South Africa, *Biogeosciences*, 6, 251–266, [https://doi.org/10.5194/bg-6-251-](https://doi.org/10.5194/bg-6-251-2009)
- 845 2009, <https://doi.org/10.5194%2Fbg-6-251-2009>, 2009.
- Ardo, J., Molder, M., El-Tahir, B. A., and Elkhidir, H. A. M.: Seasonal variation of carbon fluxes in a sparse savanna in semi arid Sudan, *Carbon Balance and Management*, 3, 7, <https://doi.org/10.1186/1750-0680-3-7>, <https://doi.org/10.1186%2F1750-0680-3-7>, 2008.
- Atkin, O. K., Bloomfield, K. J., Reich, P. B., Tjoelker, M. G., Asner, G. P., Bonal, D., Bönisch, G., Bradford, M. G., Cernusak, L. A., Cosio, E. G., Creek, D., Crous, K. Y., Domingues, T. F., Dukes, J. S., Egerton, J. J. G., Evans, J. R., Farquhar, G. D., Fyllas, N. M., Gauthier, P. P. G., Gloor, E., Gimeno, T. E., Griffin, K. L., Guerrieri, R., Heskell, M. A., Huntingford, C., Ishida, F. Y., Kattge, J., Lambers, H.,
- 850 Liddell, M. J., Lloyd, J., Lusk, C. H., Martin, R. E., Maksimov, A. P., Maximov, T. C., Malhi, Y., Medlyn, B. E., Meir, P., Mercado, L. M., Mirotchnick, N., Ng, D., Niinemets, U., O’Sullivan, O. S., Phillips, O. L., Poorter, L., Poot, P., Prentice, I. C., Salinas, N., Rowland, L. M., Ryan, M. G., Sitch, S., Slot, M., Smith, N. G., Turnbull, M. H., VanderWel, M. C., Valladares, F., Veneklaas, E. J., Weerasinghe, L. K., Wirth, C., Wright, I. J., Wythers, K. R., Xiang, J., Xiang, S., and Zaragoza-Castells, J.: Global variability in leaf respiration
- 855 in relation to climate, plant functional types and leaf traits, *New Phytologist*, 206, 614–636, <https://doi.org/10.1111/nph.13253>, <https://nph.onlinelibrary.wiley.com/doi/abs/10.1111/nph.13253>, 2015.
- Aubinet, M., Chermanne, B., Vandenhaute, M., Longdoz, B., Yernaux, M., and Laitat, E.: Long term carbon dioxide exchange above a mixed forest in the Belgian Ardennes, *Agricultural and Forest Meteorology*, 108, 293–315, [https://doi.org/10.1016/s0168-1923\(01\)00244-1](https://doi.org/10.1016/s0168-1923(01)00244-1), <https://doi.org/10.1016%2Fs0168-1923%2801%2900244-1>, 2001.
- 860 Badgley, G., Field, C. B., and Berry, J. A.: Canopy near-infrared reflectance and terrestrial photosynthesis, *Sci Adv*, 3, e1602 244, 2017.
- Baldocchi, D., Chen, Q., Chen, X., Ma, S., Miller, G., Ryu, Y., Xiao, J., Wenk, R., and Battles, J.: The Dynamics of Energy, Water, and Carbon Fluxes in a Blue Oak (*Quercus douglasii*) Savanna in California, in: *Ecosystem Function in Savannas*, pp. 135–151, CRC Press, <https://doi.org/10.1201/b10275-10>, <https://doi.org/10.1201%2Fb10275-10>, 2010.
- Ball, J. T., Timothy Ball, J., Woodrow, I. E., and Berry, J. A.: A Model Predicting Stomatal Conductance and its Contribution to the Control
- 865 of Photosynthesis under Different Environmental Conditions, in: *Progress in Photosynthesis Research*, pp. 221–224, 1987.
- Beck, H. E., Zimmermann, N. E., McVicar, T. R., Vergopolan, N., Berg, A., and Wood, E. F.: Present and future Köppen-Geiger climate classification maps at 1-km resolution, *Scientific Data*, 5, 180 214, <https://doi.org/10.1038/sdata.2018.214>, <https://doi.org/10.1038/sdata.2018.214>, 2018.
- Beer, C., Ciais, P., Reichstein, M., Baldocchi, D., Law, B. E., Papale, D., Soussana, J.-F., Ammann, C., Buchmann, N., Frank, D., Gi-
- 870 anelle, D., Janssens, I. A., Knohl, A., Köstner, B., Moors, E., Rouspard, O., Verbeeck, H., Vesala, T., Williams, C. A., and Wohlfahrt,

- G.: Temporal and among-site variability of inherent water use efficiency at the ecosystem level, *Global Biogeochemical Cycles*, 23, <https://doi.org/10.1029/2008GB003233>, <https://agupubs.onlinelibrary.wiley.com/doi/abs/10.1029/2008GB003233>, 2009.
- Berberan-Santos, M. N., Bodunov, E. N., and Pogliani, L.: On the barometric formula, *American Journal of Physics*, 65, 404–412, 1997.
- Berbigier, P., Bonnefond, J.-M., and Mellmann, P.: CO<sub>2</sub> and water vapour fluxes for 2 years above Euroflux forest site, *Agricultural and Forest Meteorology*, 108, 183–197, [https://doi.org/10.1016/s0168-1923\(01\)00240-4](https://doi.org/10.1016/s0168-1923(01)00240-4), <https://doi.org/10.1016%2Fs0168-1923%2801%2900240-4>, 2001.
- Bergeron, O., Margolis, H. A., Black, T. A., Coursolle, C., Dunn, A. L., Barr, A. G., and Wofsy, S. C.: Comparison of carbon dioxide fluxes over three boreal black spruce forests in Canada, *Global Change Biology*, 13, 89–107, <https://doi.org/10.1111/j.1365-2486.2006.01281.x>, <https://doi.org/10.1111%2Fj.1365-2486.2006.01281.x>, 2007.
- 880 Beringer, J., Hacker, J., Hutley, L. B., Leuning, R., Arndt, S. K., Amiri, R., Bannehr, L., Cernusak, L. A., Grover, S., Hensley, C., Hocking, D., Isaac, P., Jamali, H., Kanniah, K., Livesley, S., Neininger, B., U, K. T. P., Sea, W., Straten, D., Tapper, N., Weinmann, R., Wood, S., and Zegelin, S.: SPECIAL—Savanna Patterns of Energy and Carbon Integrated across the Landscape, *Bulletin of the American Meteorological Society*, 92, 1467–1485, <https://doi.org/10.1175/2011bams2948.1>, <https://doi.org/10.1175%2F2011bams2948.1>, 2011a.
- Beringer, J., Hutley, L. B., Hacker, J. M., Neininger, B., and U, K. T. P.: Patterns and processes of carbon, water and energy cycles across northern Australian landscapes: From point to region, *Agricultural and Forest Meteorology*, 151, 1409–1416, <https://doi.org/10.1016/j.agrformet.2011.05.003>, <https://doi.org/10.1016%2Fj.agrformet.2011.05.003>, 2011b.
- 885 Beringer, J., Hutley, L. B., Hacker, J. M., Neininger, B., and U, K. T. P.: Patterns and processes of carbon, water and energy cycles across northern Australian landscapes: From point to region, *Agricultural and Forest Meteorology*, 151, 1409–1416, <https://doi.org/10.1016/j.agrformet.2011.05.003>, <https://doi.org/10.1016%2Fj.agrformet.2011.05.003>, 2011c.
- 890 Beringer, J., Hutley, L. B., McHugh, I., Arndt, S. K., Campbell, D., Cleugh, H. A., Cleverly, J., De Dios, V. R., Eamus, D., Evans, B., Ewenz, C., Grace, P., Griebel, A., Haverd, V., Hinko-Najera, N., Huete, A., Isaac, P., Kanniah, K., Leuning, R., Liddell, M. J., MacFarlane, C., Meyer, W., Moore, C., Pendall, E., Phillips, A., Phillips, R. L., Prober, S. M., Restrepo-Coupe, N., Rutledge, S., Schroder, I., Silberstein, R., Southall, P., Sun Yee, M., Tapper, N. J., Van Gorsel, E., Vote, C., Walker, J., and Wardlaw, T.: An introduction to the Australian and New Zealand flux tower network - OzFlux, *Biogeosciences*, 13, 5895–5916, <https://doi.org/10.5194/bg-13-5895-2016>, <http://www.biogeosciences.net/13/5895/2016/><https://doi.org/10.5194https://doi.org/10.5194%2Fbg-13-5895-2016>, 2016.
- 895 Bernacchi, C. J., Singsaas, E. L., Pimentel, C., Portis, A. R. J., and Long, S. P.: Improved temperature response functions for models of Rubisco-limited photosynthesis, *Plant, Cell and Environment*, 24, 253–259, 2001.
- Bernacchi, C. J., Pimentel, C., and Long, S. P.: In vivo temperature response functions of parameters required to model RuBP-limited photosynthesis, *Plant Cell Environ.*, 26, 1419–1430, 2003.
- 900 Biederman, J. A., Scott, R. L., Goulden, M. L., Vargas, R., Litvak, M. E., Kolb, T. E., Yepez, E. A., Oechel, W. C., Blanken, P. D., Bell, T. W., Garatuza-Payan, J., Maurer, G. E., Dore, S., and Burns, S. P.: Terrestrial carbon balance in a drier world: the effects of water availability in southwestern North America, *Global Change Biology*, 22, 1867–1879, <https://doi.org/10.1111/gcb.13222>, <http://dx.doi.org/10.1111/gcb.13222>, 2016.
- Bonal, D., Bosc, A., Ponton, S., Goret, J.-Y., Burban, B., Gross, P., Bonnefond, J.-M., Elbers, J., Longdoz, B., Epron, D., Guehl, J.-M., and Granier, A.: Impact of severe dry season on net ecosystem exchange in the Neotropical rainforest of French Guiana, *Global Change Biology*, 14, 1917–1933, <https://doi.org/10.1111/j.1365-2486.2008.01610.x>, <https://doi.org/10.1111%2Fj.1365-2486.2008.01610.x>, 2008.

- Bowling, D. R., Bethers-Marchetti, S., Lunch, C. K., Grote, E. E., and Belnap, J.: Carbon, water, and energy fluxes in a semiarid cold desert grassland during and following multiyear drought, *Journal of Geophysical Research*, 115, <https://doi.org/10.1029/2010jg001322>, <https://doi.org/10.1029%2F2010jg001322>, 2010.
- 910 Bristow, M., Hutley, L. B., Beringer, J., Livesley, S. J., Edwards, A. C., and Arndt, S. K.: Quantifying the relative importance of greenhouse gas emissions from current and future savanna land use change across northern Australia, *Biogeosciences Discussions*, pp. 1–47, <https://doi.org/10.5194/bg-2016-191>, <https://doi.org/10.5194%2Fbg-2016-191>, 2016.
- Cernusak, L. A., Hutley, L. B., Beringer, J., Holtum, J. A., and Turner, B. L.: Photosynthetic physiology of eucalypts along a sub-continental rainfall gradient in northern Australia, *Agricultural and Forest Meteorology*, 151, 1462–1470, <https://doi.org/10.1016/j.agrformet.2011.01.006>, <https://doi.org/10.1016%2Fj.agrformet.2011.01.006>, 2011.
- 915 Chen, B., Liu, J., Chen, J. M., Croft, H., Gonsamo, A., He, L., and Luo, X.: Assessment of foliage clumping effects on evapotranspiration estimates in forested ecosystems, *Agricultural and Forest Meteorology*, 216, 82 – 92, <https://doi.org/https://doi.org/10.1016/j.agrformet.2015.09.017>, <http://www.sciencedirect.com/science/article/pii/S0168192315007236>, 2016.
- 920 Chen, J.-L., Reynolds, J. F., Harley, P. C., and Tenhunen, J. D.: Coordination theory of leaf nitrogen distribution in a canopy, *Oecologia*, 93, 63–69, 1993.
- Chen, S., Chen, J., Lin, G., Zhang, W., Miao, H., Wei, L., Huang, J., and Han, X.: Energy balance and partition in Inner Mongolia steppe ecosystems with different land use types, *Agricultural and Forest Meteorology*, 149, 1800–1809, <https://doi.org/10.1016/j.agrformet.2009.06.009>, <https://doi.org/10.1016%2Fj.agrformet.2009.06.009>, 2009.
- 925 Chiesi, M., Maselli, F., Bindi, M., Fibbi, L., Cherubini, P., Arlotta, E., Tirone, G., Matteucci, G., and Seufert, G.: Modelling carbon budget of Mediterranean forests using ground and remote sensing measurements, *Agricultural and Forest Meteorology*, 135, 22–34, <https://doi.org/10.1016/j.agrformet.2005.09.011>, <https://doi.org/10.1016%2Fj.agrformet.2005.09.011>, 2005.
- Cleverly, J., Boulain, N., Villalobos-Vega, R., Grant, N., Faux, R., Wood, C., Cook, P. G., Yu, Q., Leigh, A., and Eamus, D.: Dynamics of component carbon fluxes in a semi-arid Acacia woodland, central Australia, *Journal of Geophysical Research: Biogeosciences*, 118, 1168–1185, <https://doi.org/10.1002/jgrg.20101>, <https://doi.org/10.1002%2Fjgrg.20101>, 2013.
- 930 Cleverly, J., Eamus, D., Van Gorsel, E., Chen, C., Rumman, R., Luo, Q., Coupe, N. R., Li, L., Kljun, N., Faux, R., Yu, Q., and Huete, A.: Productivity and evapotranspiration of two contrasting semiarid ecosystems following the 2011 global carbon land sink anomaly, *Agricultural and Forest Meteorology*, 220, 151–159, <https://doi.org/10.1016/j.agrformet.2016.01.086>, <http://linkinghub.elsevier.com/retrieve/pii/S0168192316300971>, 2016.
- 935 Cook, B. D., Davis, K. J., Wang, W., Desai, A., Berger, B. W., Teclaw, R. M., Martin, J. G., Bolstad, P. V., Bakwin, P. S., Yi, C., and Heilman, W.: Carbon exchange and venting anomalies in an upland deciduous forest in northern Wisconsin, USA, *Agricultural and Forest Meteorology*, 126, 271–295, <https://doi.org/10.1016/j.agrformet.2004.06.008>, <https://doi.org/10.1016%2Fj.agrformet.2004.06.008>, 2004.
- Cowan, I. R. and Farquhar, G. D.: Stomatal function in relation to leaf metabolism and environment, *Symp. Soc. Exp. Biol.*, 31, 471–505, 1977.
- 940 Davis, T. W., Prentice, I. C., Stocker, B. D., Thomas, R. T., Whitley, R. J., Wang, H., Evans, B. J., Gallego-Sala, A. V., Sykes, M. T., and Cramer, W.: Simple process-led algorithms for simulating habitats (SPLASH v.1.0): robust indices of radiation, evapotranspiration and plant-available moisture, *Geoscientific Model Development*, 10, 689–708, <https://doi.org/10.5194/gmd-10-689-2017>, <http://www.geosci-model-dev.net/10/689/2017/>, 2017.

- Delpierre, N., Berveiller, D., Granda, E., and Dufrêne, E.: Wood phenology, not carbon input, controls the interannual variability of wood growth in a temperate oak forest, *New Phytologist*, 210, 459–470, <https://doi.org/10.1111/nph.13771>, <https://doi.org/10.1111%2Fnph.13771>, 2015.
- Desai, A. R., Bolstad, P. V., Cook, B. D., Davis, K. J., and Carey, E. V.: Comparing net ecosystem exchange of carbon dioxide between an old-growth and mature forest in the upper Midwest, USA, *Agricultural and Forest Meteorology*, 128, 33–55, <https://doi.org/10.1016/j.agrformet.2004.09.005>, <https://doi.org/10.1016%2Fj.agrformet.2004.09.005>, 2005.
- Desai, A. R., Xu, K., Tian, H., Weishampel, P., Thom, J., Baumann, D., Andrews, A. E., Cook, B. D., King, J. Y., and Kolka, R.: Landscape-level terrestrial methane flux observed from a very tall tower, *Agricultural and Forest Meteorology*, 201, 61–75, <https://doi.org/10.1016/j.agrformet.2014.10.017>, <https://doi.org/10.1016%2Fj.agrformet.2014.10.017>, 2015.
- Didan, K.: MOD13Q1 MODIS/Terra Vegetation Indices 16-Day L3 Global 250m SIN Grid V006, <https://doi.org/10.5067/MODIS/MOD13Q1.006>, <https://doi.org/doi.org/10.5067/MODIS/MOD13Q1.006>, 2015.
- Dragonì, D., Schmid, H. P., Wayson, C. A., Potter, H., Grimmond, C. S. B., and Randolph, J. C.: Evidence of increased net ecosystem productivity associated with a longer vegetated season in a deciduous forest in south-central Indiana, USA, *Global Change Biology*, 17, 886–897, <https://doi.org/10.1111/j.1365-2486.2010.02281.x>, <https://doi.org/10.1111%2Fj.1365-2486.2010.02281.x>, 2011.
- Dunn, A. L., Barford, C. C., Wofsy, S. C., Goulden, M. L., and Daube, B. C.: A long-term record of carbon exchange in a boreal black spruce forest: means, responses to interannual variability, and decadal trends, *Global Change Biology*, 13, 577–590, <https://doi.org/10.1111/j.1365-2486.2006.01221.x>, <https://doi.org/10.1111%2Fj.1365-2486.2006.01221.x>, 2007.
- Egea, G., Verhoef, A., and Vidale, P. L.: Towards an improved and more flexible representation of water stress in coupled photosynthesis–stomatal conductance models, *Agric. For. Meteorol.*, 151, 1370–1384, 2011.
- Ensminger, I., Sveshnikov, D., Campbell, D. A., Funk, C., Jansson, S., Lloyd, J., Shibistova, O., and Öquist, G.: Intermittent low temperatures constrain spring recovery of photosynthesis in boreal Scots pine forests, *Global Change Biology*, 10, 995–1008, <https://doi.org/10.1111/j.1365-2486.2004.00781.x>, <https://onlinelibrary.wiley.com/doi/abs/10.1111/j.1365-2486.2004.00781.x>, 2004.
- Etzold, S., Ruehr, N. K., Zweifel, R., Dobbertin, M., Zingg, A., Pluess, P., Häsler, R., Eugster, W., and Buchmann, N.: The Carbon Balance of Two Contrasting Mountain Forest Ecosystems in Switzerland: Similar Annual Trends, but Seasonal Differences, *Ecosystems*, 14, 1289–1309, <https://doi.org/10.1007/s10021-011-9481-3>, <https://doi.org/10.1007%2Fs10021-011-9481-3>, 2011.
- Falge, E., Aubinet, M., Bakwin, P. S., Baldocchi, D., Berbigier, P., Bernhofer, C., Black, T. A., Ceulemans, R., Davis, K. J., Dolman, A. J., Goldstein, A., Goulden, M. L., Granier, A., Hollinger, D. Y., Jarvis, P. G., Jensen, N., Pilegaard, K., Katul, G., Kyaw Tha Paw, P., Law, B. E., Lindroth, A., Loustau, D., Mahli, Y., Monson, R., Moncrieff, P., Moors, E., Munger, J. W., Meyers, T., Oechel, W., Schulze, E. d., Thorgeirsson, H., Tenhunen, J., Valentini, R., Verma, S. B., Vesala, T., and Wofsy, S. C.: FLUXNET Research Network Site Characteristics, Investigators, and Bibliography, 2016, <https://doi.org/10.3334/ornldaac/1530>, [https://daac.ornl.gov/cgi-bin/dsvviewer.pl?ds\\_id=1530](https://daac.ornl.gov/cgi-bin/dsvviewer.pl?ds_id=1530), 2017.
- Fan, Y., Li, H., and Miguez-Macho, G.: Global Patterns of Groundwater Table Depth, *Science*, 339, 940–943, <https://doi.org/10.1126/science.1229881>, <http://science.sciencemag.org/content/339/6122/940>, 2013.
- Fan, Y., Miguez-Macho, G., Jobbágy, E. G., Jackson, R. B., and Otero-Casal, C.: Hydrologic regulation of plant rooting depth, *Proceedings of the National Academy of Sciences*, 114, 10 572–10 577, <https://doi.org/10.1073/pnas.1712381114>, <https://www.pnas.org/content/114/40/10572>, 2017.

- 980 Fares, S., Savi, F., Muller, J., Matteucci, G., and Paoletti, E.: Simultaneous measurements of above and below canopy ozone fluxes help partitioning ozone deposition between its various sinks in a Mediterranean Oak Forest, *Agricultural and Forest Meteorology*, 198–199, 181–191, <https://doi.org/10.1016/j.agrformet.2014.08.014>, <https://doi.org/10.1016%2Fj.agrformet.2014.08.014>, 2014.
- Farquhar, G. D. and Wong, S. C.: An Empirical Model of Stomatal Conductance, *Functional Plant Biology*, 11, 191–210, <https://doi.org/10.1071/PP9840191>, 1984.
- 985 Farquhar, G. D., von Caemmerer, S., and Berry, J. A.: A biochemical model of photosynthetic CO<sub>2</sub> assimilation in leaves of C<sub>3</sub> species, *Planta*, 149, 78–90, 1980.
- Ferréa, C., Zenone, T., Comolli, R., and Seufert, G.: Estimating heterotrophic and autotrophic soil respiration in a semi-natural forest of Lombardy, Italy, *Pedobiologia*, 55, 285–294, <https://doi.org/10.1016/j.pedobi.2012.05.001>, <https://doi.org/10.1016%2Fj.pedobi.2012.05.001>, 2012.
- 990 Fick, A.: Ueber Diffusion, *Annalen der Physik*, 170, 59–86, <https://doi.org/10.1002/andp.18551700105>, <https://onlinelibrary.wiley.com/doi/abs/10.1002/andp.18551700105>, 1855.
- Field, C. B., Randerson, J. T., and Malmström, C. M.: Global net primary production: Combining ecology and remote sensing, *Remote Sensing of Environment*, 51, 74 – 88, [https://doi.org/http://dx.doi.org/10.1016/0034-4257\(94\)00066-V](https://doi.org/http://dx.doi.org/10.1016/0034-4257(94)00066-V), <http://www.sciencedirect.com/science/article/pii/003442579400066V>, 1995.
- 995 Frank, J. M., Massman, W. J., Ewers, B. E., Huckaby, L. S., and Negrón, J. F.: Ecosystem CO<sub>2</sub>/H<sub>2</sub>O fluxes are explained by hydraulically limited gas exchange during tree mortality from spruce bark beetles, *Journal of Geophysical Research: Biogeosciences*, 119, 1195–1215, <https://doi.org/10.1002/2013jg002597>, <https://doi.org/10.1002%2F2013jg002597>, 2014.
- Frankenberg, C., Köhler, P., Magney, T. S., Geier, S., Lawson, P., Schwochert, M., McDuffie, J., Drewry, D. T., Pavlick, R., and Kuhnert, A.: The Chlorophyll Fluorescence Imaging Spectrometer (CFIS), mapping far red fluorescence from aircraft, *Remote Sens. Environ.*, 217, 523–536, 2018.
- 1000 Galvagno, M., Wohlfahrt, G., Cremonese, E., Rossini, M., Colombo, R., Filippa, G., Julitta, T., Manca, G., Siniscalco, C., di Cella, U. M., and Migliavacca, M.: Phenology and carbon dioxide source/sink strength of a subalpine grassland in response to an exceptionally short snow season, *Environmental Research Letters*, 8, 025 008, <https://doi.org/10.1088/1748-9326/8/2/025008>, <https://doi.org/10.1088%2F1748-9326%2F8%2F2%2F025008>, 2013.
- 1005 Gamon, J., Peñuelas, J., and Field, C.: A narrow-waveband spectral index that tracks diurnal changes in photosynthetic efficiency, *Remote Sensing of Environment*, 41, 35 – 44, [https://doi.org/http://dx.doi.org/10.1016/0034-4257\(92\)90059-S](https://doi.org/http://dx.doi.org/10.1016/0034-4257(92)90059-S), <http://www.sciencedirect.com/science/article/pii/003442579290059S>, 1992.
- Gamon, J. A., Huemmrich, K. F., Wong, C. Y. S., Ensminger, I., Garrity, S., Hollinger, D. Y., Noormets, A., and Peñuelas, J.: A remotely sensed pigment index reveals photosynthetic phenology in evergreen conifers, *Proceedings of the National Academy of Sciences*, 113, 13 087–13 092, <https://doi.org/10.1073/pnas.1606162113>, <http://www.pnas.org/content/113/46/13087.abstract>, 2016.
- 1010 Goldstein, A., Hultman, N., Fracheboud, J., Bauer, M., Panek, J., Xu, M., Qi, Y., Guenther, A., and Baugh, W.: Effects of climate variability on the carbon dioxide, water, and sensible heat fluxes above a ponderosa pine plantation in the Sierra Nevada (CA), *Agricultural and Forest Meteorology*, 101, 113–129, [https://doi.org/10.1016/s0168-1923\(99\)00168-9](https://doi.org/10.1016/s0168-1923(99)00168-9), <https://doi.org/10.1016%2Fs0168-1923%2899%2900168-9>, 2000.
- 1015 Gough, C. M., Hardiman, B. S., Nave, L. E., Bohrer, G., Maurer, K. D., Vogel, C. S., Nadelhoffer, K. J., and Curtis, P. S.: Sustained carbon uptake and storage following moderate disturbance in a Great Lakes forest, *Ecological Applications*, 23, 1202–1215, <https://doi.org/10.1890/12-1554.1>, <https://doi.org/10.1890%2F12-1554.1>, 2013.

- Greve, P., Orlowsky, B., Mueller, B., Sheffield, J., Reichstein, M., and Seneviratne, S. I.: Global assessment of trends in wetting and drying over land, *Nature Geosci*, 7, 716–721, <http://dx.doi.org/10.1038/ngeo2247>, 2014.
- 1020 Grünwald, T. and Bernhofer, C.: A decade of carbon, water and energy flux measurements of an old spruce forest at the Anchor Station Tharandt, *Tellus B*, 59, <https://doi.org/10.3402/tellusb.v59i3.17000>, <https://doi.org/10.3402%2Ftellusb.v59i3.17000>, 2007.
- Guan, D.-X., Wu, J.-B., Zhao, X.-S., Han, S.-J., Yu, G.-R., Sun, X.-M., and Jin, C.-J.: CO<sub>2</sub> fluxes over an old, temperate mixed forest in northeastern China, *Agricultural and Forest Meteorology*, 137, 138–149, <https://doi.org/10.1016/j.agrformet.2006.02.003>, <https://doi.org/10.1016%2Fj.agrformet.2006.02.003>, 2006.
- 1025 Guanter, L., Zhang, Y., Jung, M., Joiner, J., Voigt, M., Berry, J. A., Frankenberg, C., Huete, A. R., Zarco-Tejada, P., Lee, J.-E., Susan Moran, M., Ponce-Campos, G., Beer, C., Camps-Valls, G., Buchmann, N., Gianelle, D., Klumpp, K., Cescatti, A., Baker, J. M., and Griffis, T. J.: Global and time-resolved monitoring of crop photosynthesis with chlorophyll fluorescence, *Proc. Natl. Acad. Sci. U. S. A.*, 111, E1327–E1333, 2014.
- Harris, I., Jones, P., Osborn, T., and Lister, D.: Updated high-resolution grids of monthly climatic observations – the CRU TS3.10 Dataset, *International Journal of Climatology*, 34, 623–642, <https://doi.org/10.1002/joc.3711>, <http://dx.doi.org/10.1002/joc.3711>, 2014.
- 1030 Haxeltine, A. and Prentice, I. C.: A General Model for the Light-Use Efficiency of Primary Production, *Funct. Ecol.*, 10, 551, 1996.
- He, L., Chen, J. M., Gonsamo, A., Luo, X., Wang, R., Liu, Y., and Liu, R.: Changes in the Shadow: The Shifting Role of Shaded Leaves in Global Carbon and Water Cycles Under Climate Change, *Geophysical Research Letters*, 45, 5052–5061, <https://doi.org/10.1029/2018GL077560>, <https://agupubs.onlinelibrary.wiley.com/doi/abs/10.1029/2018GL077560>, 2018.
- 1035 Heinsch, F. A., Running, S. W., Kimball, J. S., Nemani, R. R., Davis, K. J., Bolstad, P. V., Cook, B. D., Desai, A. R., Ricciuto, D. M., Law, B. E., Oechel, W. C., Wofsy, S. C., Dunn, A. L., Munger, J. W., Baldocchi, D. D., Hollinger, D. Y., Richardson, A. D., Stoy, P. C., Siqueira, M. B. S., Monson, R. K., Burns, S. P., and Flanagan, L. B.: Evaluation of remote sensing based terrestrial productivity from MODIS using regional tower eddy flux network observations, *IEEE Transactions on Geoscience and Remote Sensing*, 44, 1908–1925, <https://doi.org/10.1109/TGRS.2005.853936>, 2006.
- 1040 Hengl, T., de Jesus, J. M., MacMillan, R. A., Batjes, N. H., Heuvelink, G. B. M., Ribeiro, E., Samuel-Rosa, A., Kempen, B., Leenaars, J. G. B., Walsh, M. G., and Gonzalez, M. R.: SoilGrids1km–global soil information based on automated mapping, *PLoS One*, 9, e105992, 2014.
- Heskel, M., O’Sullivan, O., Reich, P., Tjoelker, M., Weerasinghe, L., Penillard, A., Egerton, J., Creek, D., Bloomfield, K., Xiang, J., Sinca, F., Stangl, Z., Martinez-De La Torre, A., Griffin, K., Huntingford, C., Hurry, V., Meir, P., Turnbull, M., and Atkin, O.: Convergence in the temperature response of leaf respiration across biomes and plant functional types, *Proceedings of the National Academy of Sciences of the United States of America*, 113, 3832–3837, <https://doi.org/10.1073/pnas.1520282113>, 2016.
- 1045 Hinko-Najera, N., Isaac, P., Beringer, J., van Gorsel, E., Ewenz, C., McHugh, I., Exbrayat, J.-F., Livesley, S. J., and Arndt, S. K.: Net ecosystem carbon exchange of a dry temperate eucalypt forest, *Biogeosciences*, 14, 3781–3800, <https://doi.org/10.5194/bg-14-3781-2017>, <https://www.biogeosciences.net/14/3781/2017/>, 2017.
- 1050 Hoshika, Y., Fares, S., Savi, F., Gruening, C., Goded, I., De Marco, A., Sicard, P., and Paoletti, E.: Stomatal conductance models for ozone risk assessment at canopy level in two Mediterranean evergreen forests, *Agricultural and Forest Meteorology*, 234–235, 212–221, <https://doi.org/10.1016/j.agrformet.2017.01.005>, 2017.
- Huber, M. L., Perkins, R. A., Laesecke, A., Friend, D. G., Sengers, J. V., Assael, M. J., Metaxa, I. N., Vogel, E., Mareš, R., and Miyagawa, K.: New international formulation for the viscosity of H<sub>2</sub>O, *Journal of Physical and Chemical Reference Data*, 38, 101–125, 2009.
- 1055 Hufkens, K.: khufkens/gee\_subset: Google Earth Engine subset script and library, <https://doi.org/10.5281/zenodo.833789>, 2017.

- Huner, N. P., Oquist, G., Hurry, V. M., Krol, M., Falk, S., and Griffith, M.: Photosynthesis, photoinhibition and low temperature acclimation in cold tolerant plants, *Photosynth. Res.*, 37, 19–39, 1993.
- Hutley, L. B., Beringer, J., Isaac, P. R., Hacker, J. M., and Cernusak, L. A.: A sub-continental scale living laboratory: Spatial patterns of savanna vegetation over a rainfall gradient in northern Australia, *Agricultural and Forest Meteorology*, 151, 1417–1428, <https://doi.org/10.1016/j.agrformet.2011.03.002>, <https://doi.org/10.1016%2Fj.agrformet.2011.03.002>, 2011.
- Imer, D., Merbold, L., Eugster, W., and Buchmann, N.: Temporal and spatial variations of soil CO<sub>2</sub>, CH<sub>4</sub> and N<sub>2</sub>O fluxes at three differently managed grasslands, *Biogeosciences*, 10, 5931–5945, <https://doi.org/10.5194/bg-10-5931-2013>, <https://doi.org/10.5194%2Fbg-10-5931-2013>, 2013.
- Irvine, J., Law, B. E., and Hibbard, K. A.: Postfire carbon pools and fluxes in semiarid ponderosa pine in Central Oregon, *Global Change Biology*, 13, 1748–1760, <https://doi.org/10.1111/j.1365-2486.2007.01368.x>, <https://doi.org/10.1111%2Fj.1365-2486.2007.01368.x>, 2007.
- Irvine, J., Law, B. E., Martin, J. G., and Vickers, D.: Interannual variation in soil CO<sub>2</sub> efflux and the response of root respiration to climate and canopy gas exchange in mature ponderosa pine, *Global Change Biology*, 14, 2848–2859, <https://doi.org/10.1111/j.1365-2486.2008.01682.x>, <https://doi.org/10.1111%2Fj.1365-2486.2008.01682.x>, 2008.
- Jacobs, C. M. J., Jacobs, A. F. G., Bosveld, F. C., Hendriks, D. M. D., Hensen, A., Kroon, P. S., Moors, E. J., Nol, L., Schrier-Uijl, A., and Veenendaal, E. M.: Variability of annual CO<sub>2</sub> exchange from Dutch grasslands, *Biogeosciences*, 4, 803–816, <https://doi.org/10.5194/bg-4-803-2007>, <https://doi.org/10.5194%2Fbg-4-803-2007>, 2007.
- Jiang, C. and Ryu, Y.: Multi-scale evaluation of global gross primary productivity and evapotranspiration products derived from Breathing Earth System Simulator (BESS), *Remote Sens. Environ.*, 186, 528–547, 2016.
- Joiner, J., Guanter, L., Lindstrot, R., Voigt, M., Vasilkov, A. P., Middleton, E. M., Huemmrich, K. F., Yoshida, Y., and Frankenberg, C.: Global monitoring of terrestrial chlorophyll fluorescence from moderate-spectral-resolution near-infrared satellite measurements: methodology, simulations, and application to GOME-2, *Atmospheric Measurement Techniques*, 6, 2803–2823, <https://doi.org/10.5194/amt-6-2803-2013>, <https://www.atmos-meas-tech.net/6/2803/2013/>, 2013.
- Joiner, J., Yoshida, Y., Guanter, L., and Middleton, E. M.: New methods for the retrieval of chlorophyll red fluorescence from hyperspectral satellite instruments: simulations and application to GOME-2 and SCIAMACHY, *Atmospheric Measurement Techniques*, 9, 3939–3967, <https://doi.org/10.5194/amt-9-3939-2016>, <https://www.atmos-meas-tech.net/9/3939/2016/>, 2016.
- Jung, M., Reichstein, M., Margolis, H. A., Cescatti, A., Richardson, A. D., Arain, M. A., Arneth, A., Bernhofer, C., Bonal, D., Chen, J., Gianelle, D., Gobron, N., Kiely, G., Kutsch, W., Lasslop, G., Law, B. E., Lindroth, A., Merbold, L., Montagnani, L., Moors, E. J., Papale, D., Sottocornola, M., Vaccari, F., and Williams, C.: Global patterns of land-atmosphere fluxes of carbon dioxide, latent heat, and sensible heat derived from eddy covariance, satellite, and meteorological observations, *Journal of Geophysical Research: Biogeosciences*, 116, n/a–n/a, <https://doi.org/10.1029/2010JG001566>, <http://dx.doi.org/10.1029/2010JG001566>, g00J07, 2011.
- Kato, T., Tang, Y., Gu, S., Hirota, M., Du, M., Li, Y., and Zhao, X.: Temperature and biomass influences on interannual changes in CO<sub>2</sub> exchange in an alpine meadow on the Qinghai-Tibetan Plateau, *Global Change Biology*, 12, 1285–1298, <https://doi.org/10.1111/j.1365-2486.2006.01153.x>, <https://doi.org/10.1111%2Fj.1365-2486.2006.01153.x>, 2006.
- Kattge, J. and Knorr, W.: Temperature acclimation in a biochemical model of photosynthesis: a reanalysis of data from 36 species, *Plant, Cell and Environment*, 30, 1176–1190, 2007.
- Keenan, T., Sabate, S., and Gracia, C.: Soil water stress and coupled photosynthesis–conductance models: Bridging the gap between conflicting reports on the relative roles of stomatal, mesophyll conductance and biochemical limitations to photosynthesis, *Agric. For. Meteorol.*, 150, 443–453, 2010.

- Keenan, T., Baker, I., Barr, A., Ciais, P., Davis, K., Dietze, M., Dragoni, D., Gough, C. M., Grant, R., Hollinger, D., Hufkens, K., Poulter, B., McCaughey, H., Raczka, B., Ryu, Y., Schaefer, K., Tian, H., Verbeeck, H., Zhao, M., and Richardson, A. D.: Terrestrial biosphere model performance for inter-annual variability of land-atmosphere CO<sub>2</sub> exchange, *Global Change Biology*, 18, 1971–1987, <https://doi.org/10.1111/j.1365-2486.2012.02678.x>, <https://onlinelibrary.wiley.com/doi/abs/10.1111/j.1365-2486.2012.02678.x>, 2012.
- Keenan, T. F., Colin Prentice, I., Canadell, J. G., Williams, C. A., Wang, H., Raupach, M., and James Collatz, G.: Corrigendum: Recent pause in the growth rate of atmospheric CO<sub>2</sub> due to enhanced terrestrial carbon uptake, *Nat. Commun.*, 8, 16 137, 2017.
- Keenan, T. F., Migliavacca, M., Papale, D., Baldocchi, D., Reichstein, M., Torn, M., and Wutzler, T.: Widespread inhibition of daytime ecosystem respiration, *Nature Ecology & Evolution*, <https://doi.org/10.1038/s41559-019-0809-2>, <https://doi.org/10.1038/s41559-019-0809-2>, 2019.
- Kilinc, M., Beringer, J., Hutley, L. B., Tapper, N. J., and McGuire, D. A.: Carbon and water exchange of the world's tallest angiosperm forest, *Agricultural and Forest Meteorology*, 182–183, 215–224, <https://doi.org/10.1016/j.agrformet.2013.07.003>, <https://doi.org/10.1016%2Fj.agrformet.2013.07.003>, 2013.
- Knohl, A., Schulze, E.-D., Kolle, O., and Buchmann, N.: Large carbon uptake by an unmanaged 250-year-old deciduous forest in Central Germany, *Agricultural and Forest Meteorology*, 118, 151–167, [https://doi.org/10.1016/s0168-1923\(03\)00115-1](https://doi.org/10.1016/s0168-1923(03)00115-1), <https://doi.org/10.1016%2Fs0168-1923%2803%2900115-1>, 2003.
- Kok, B.: On the interrelation of respiration and photosynthesis in green plants, *Biochimica et Biophysica Acta*, 3, 625 – 631, [https://doi.org/10.1016/0006-3002\(49\)90136-5](https://doi.org/10.1016/0006-3002(49)90136-5), <http://www.sciencedirect.com/science/article/pii/0006300249901365>, 1949.
- Kurbatova, J., Li, C., Varlagin, A., Xiao, X., and Vygodskaya, N.: Modeling carbon dynamics in two adjacent spruce forests with different soil conditions in Russia, *Biogeosciences*, 5, 969–980, <https://doi.org/10.5194/bg-5-969-2008>, <https://doi.org/10.5194%2Fbg-5-969-2008>, 2008.
- Landsberg, J. J. and Waring, R. H.: A generalised model of forest productivity using simplified concepts of radiation-use efficiency, carbon balance and partitioning, *For. Ecol. Manage.*, 95, 209–228, 1997.
- Lasslop, G., Reichstein, M., Papale, D., Richardson, A., Arneeth, A., Barr, A., Stoy, P., and Wohlfahrt, G.: Separation of net ecosystem exchange into assimilation and respiration using a light response curve approach: critical issues and global evaluation, *Global Change Biology*, 16, 187–208, <https://doi.org/10.1111/j.1365-2486.2009.02041.x>, 2010.
- Leuning, R.: A critical appraisal of a combined stomatal-photosynthesis model for C<sub>3</sub> plants, *Plant Cell Environ.*, 18, 339–355, 1995.
- Leuning, R., Cleugh, H. A., Zegelin, S. J., and Hughes, D.: Carbon and water fluxes over a temperate Eucalyptus forest and a tropical wet/dry savanna in Australia: measurements and comparison with MODIS remote sensing estimates, *Agricultural and Forest Meteorology*, 129, 151–173, <https://doi.org/10.1016/j.agrformet.2004.12.004>, <https://doi.org/10.1016%2Fj.agrformet.2004.12.004>, 2005.
- Li, X., Xiao, J., He, B., Altaf Arain, M., Beringer, J., Desai, A. R., Emmel, C., Hollinger, D. Y., Krasnova, A., Mammarella, I., Noe, S. M., Ortiz, P. S., Rey-Sanchez, A. C., Rocha, A. V., and Varlagin, A.: Solar-induced chlorophyll fluorescence is strongly correlated with terrestrial photosynthesis for a wide variety of biomes: First global analysis based on OCO-2 and flux tower observations, *Glob. Chang. Biol.*, 2018.
- Lindauer, M., Schmid, H., Grote, R., Mauder, M., Steinbrecher, R., and Wolpert, B.: Net ecosystem exchange over a non-cleared wind-throw-disturbed upland spruce forest—Measurements and simulations, *Agricultural and Forest Meteorology*, 197, 219–234, <https://doi.org/10.1016/j.agrformet.2014.07.005>, <https://doi.org/10.1016%2Fj.agrformet.2014.07.005>, 2014.



- Lloyd, J. and Farquhar, G. D.:  $^{13}\text{C}$  discrimination during  $\text{CO}_2$  assimilation by the terrestrial biosphere, *Oecologia*, 99, 201–215, <https://doi.org/10.1007/BF00627732>, <https://doi.org/10.1007/BF00627732>, 1994.
- Long, S. P., Postl, W. F., and Bolhár-Nordenkamp, H. R.: Quantum yields for uptake of carbon dioxide in  $\text{C}_3$  vascular plants of contrasting habitats and taxonomic groupings, *Planta*, 189, 226–234, 1993.
- 1135 Luo, X., Keenan, T. F., Fisher, J. B., Jiménez-Muñoz, J.-C., Chen, J. M., Jiang, C., Ju, W., Perakalapudi, N.-V., Ryu, Y., and Tadić, J. M.: The impact of the 2015/2016 El Niño on global photosynthesis using satellite remote sensing, *Philosophical Transactions of the Royal Society B: Biological Sciences*, 373, 20170 409, <https://doi.org/10.1098/rstb.2017.0409>, <https://royalsocietypublishing.org/doi/abs/10.1098/rstb.2017.0409>, 2018.
- Ma, S., Baldocchi, D. D., Xu, L., and Hehn, T.: Inter-annual variability in carbon dioxide exchange of an oak/grass savanna and open  
1140 grassland in California, *Agricultural and Forest Meteorology*, 147, 157–171, <https://doi.org/10.1016/j.agrformet.2007.07.008>, <https://doi.org/10.1016%2Fj.agrformet.2007.07.008>, 2007.
- MacFarling Meure, C., Etheridge, D., Trudinger, C., Steele, P., Langenfelds, R., van Ommen, T., Smith, A., and Elkins, J.: Law Dome  $\text{CO}_2$ ,  $\text{CH}_4$  and  $\text{N}_2\text{O}$  ice core records extended to 2000 years BP, *Geophys. Res. Lett.*, 33, <https://doi.org/10.1029/2006GL026152>, 2006.
- Maire, V., Martre, P., Kattge, J., Gastal, F., Esser, G., Fontaine, S., and Soussana, J.-F.: The coordination of leaf photosynthesis links C and  
1145 N fluxes in  $\text{C}_3$  plant species, *PLoS One*, 7, e38 345, 2012.
- Mäkelä, A., Hari, P., Berninger, F., Hänninen, H., and Nikinmaa, E.: Acclimation of photosynthetic capacity in Scots pine to the annual cycle of temperature, *Tree Physiol.*, 24, 369–376, 2004.
- Marchesini, L. B., Papale, D., Reichstein, M., Vuichard, N., Tchebakova, N., and Valentini, R.: Carbon balance assessment of a natural steppe of southern Siberia by multiple constraint approach, *Biogeosciences Discussions*, 4, 165–208, <https://doi.org/10.5194/bgd-4-165-2007>,  
1150 2007, <https://doi.org/10.5194%2Fbgd-4-165-2007>, 2007.
- Marcolla, B., Pitacco, A., and Cescatti, A.: Canopy Architecture and Turbulence Structure in a Coniferous Forest, *Boundary-Layer Meteorology*, 108, 39–59, <https://doi.org/10.1023/a:1023027709805>, <https://doi.org/10.1023%2Fa%3A1023027709805>, 2003a.
- Marcolla, B., Pitacco, A., and Cescatti, A.: Canopy Architecture and Turbulence Structure in a Coniferous Forest, *Boundary-Layer Meteorology*, 108, 39–59, <https://doi.org/10.1023/a:1023027709805>, <https://doi.org/10.1023%2Fa%3A1023027709805>, 2003b.
- 1155 Marcolla, B., Cescatti, A., Manca, G., Zorer, R., Cavagna, M., Fiora, A., Gianelle, D., Rodeghiero, M., Sottocornola, M., and Zampedri, R.: Climatic controls and ecosystem responses drive the inter-annual variability of the net ecosystem exchange of an alpine meadow, *Agricultural and Forest Meteorology*, 151, 1233–1243, <https://doi.org/10.1016/j.agrformet.2011.04.015>, <https://doi.org/10.1016%2Fj.agrformet.2011.04.015>, 2011.
- Matsumoto, K., Ohta, T., Nakai, T., Kuwada, T., Daikoku, K., Iida, S., Yabuki, H., Kononov, A. V., van der Molen, M. K., Kodama, Y.,  
1160 Maximov, T. C., Dolman, A. J., and Hattori, S.: Energy consumption and evapotranspiration at several boreal and temperate forests in the Far East, *Agricultural and Forest Meteorology*, 148, 1978–1989, <https://doi.org/10.1016/j.agrformet.2008.09.008>, <https://doi.org/10.1016%2Fj.agrformet.2008.09.008>, 2008.
- McHugh, I. D., Beringer, J., Cunningham, S. C., Baker, P. J., Cavagnaro, T. R., Nally, R. M., and Thompson, R. M.: Interactions between nocturnal turbulent flux, storage and advection at an “ideal” eucalypt woodland site, *Biogeosciences*, 14, 3027–3050, <https://doi.org/10.5194/bg-14-3027-2017>, <https://doi.org/10.5194%2Fbg-14-3027-2017>, 2017.
- 1165 McNevin, D., von Caemmerer, S., and Farquhar, G.: Determining RuBisCO activation kinetics and other rate and equilibrium constants by simultaneous multiple non-linear regression of a kinetic model, *J. Exp. Bot.*, 57, 3883–3900, 2006.
- Medlyn, B. E.: Physiological basis of the light use efficiency model, *Tree Physiol.*, 18, 167–176, 1998.

- Medlyn, B. E., Duursma, R. A., Eamus, D., Ellsworth, D. S., Colin Prentice, I., Barton, C. V. M., Crous, K. Y., de Angelis, P., Freeman, M., and Wingate, L.: Reconciling the optimal and empirical approaches to modelling stomatal conductance, *Glob. Chang. Biol.*, 17, 2134–2144, 2011.
- Meek, D. W., Hatfield, J. L., Howell, T. A., Idso, S. B., and Reginato, R. J.: A Generalized Relationship between Photosynthetically Active Radiation and Solar Radiation<sup>1</sup>, *Agron. J.*, 76, 939–945, 1984.
- Merbold, L., Ardö, J., Arneth, A., Scholes, R. J., Nouvellon, Y., de Grandcourt, A., Archibald, S., Bonnefond, J. M., Boulain, N., Brueggemann, N., Bruemmer, C., Cappelaere, B., Ceschia, E., El-Khidir, H. A. M., El-Tahir, B. A., Falk, U., Lloyd, J., Kergoat, L., Dantec, V. L., Mougin, E., Muchinda, M., Mukelabai, M. M., Ramier, D., Roupsard, O., Timouk, F., Veenendaal, E. M., and Kutsch, W. L.: Precipitation as driver of carbon fluxes in 11 African ecosystems, *Biogeosciences*, 6, 1027–1041, <https://doi.org/10.5194/bg-6-1027-2009>, <https://doi.org/10.5194%2Fbg-6-1027-2009>, 2009.
- Merbold, L., Eugster, W., Stieger, J., Zahniser, M., Nelson, D., and Buchmann, N.: Greenhouse gas budget (CO<sub>2</sub>, CH<sub>4</sub> and N<sub>2</sub>O) of intensively managed grassland following restoration, *Global Change Biology*, 20, 1913–1928, <https://doi.org/10.1111/gcb.12518>, <https://doi.org/10.1111%2Fgcb.12518>, 2014.
- Meyer, W. S., Kondrlovà, E., and Koerber, G. R.: Evaporation of perennial semi-arid woodland in southeastern Australia is adapted for irregular but common dry periods, *Hydrological Processes*, 29, 3714–3726, <https://doi.org/10.1002/hyp.10467>, <https://doi.org/10.1002%2Fhyp.10467>, 2015.
- Michaletz, S. T., Weiser, M. D., Zhou, J., Kaspari, M., Helliker, B. R., and Enquist, B. J.: Plant Thermoregulation: Energetics, Trait-Environment Interactions, and Carbon Economics, *Trends Ecol. Evol.*, 30, 714–724, 2015.
- Migliavacca, M., Meroni, M., Busetto, L., Colombo, R., Zenone, T., Matteucci, G., Manca, G., and Seufert, G.: Modeling Gross Primary Production of Agro-Forestry Ecosystems by Assimilation of Satellite-Derived Information in a Process-Based Model, *Sensors*, 9, 922–942, <https://doi.org/10.3390/s90200922>, <https://doi.org/10.3390%2Fs90200922>, 2009.
- Monson, R. K., Turnipseed, A. A., Sparks, J. P., Harley, P. C., Scott-Denton, L. E., Sparks, K., and Huxman, T. E.: Carbon sequestration in a high-elevation, subalpine forest, *Global Change Biology*, 8, 459–478, <https://doi.org/10.1046/j.1365-2486.2002.00480.x>, <https://doi.org/10.1046%2Fj.1365-2486.2002.00480.x>, 2002.
- Montagnani, L., Manca, G., Canepa, E., Georgieva, E., Acosta, M., Feigenwinter, C., Janous, D., Kerschbaumer, G., Lindroth, A., Minach, L., Minerbi, S., Mölder, M., Pavelka, M., Seufert, G., Zeri, M., and Ziegler, W.: A new mass conservation approach to the study of CO<sub>2</sub> advection in an alpine forest, *Journal of Geophysical Research*, 114, <https://doi.org/10.1029/2008jd010650>, <https://doi.org/10.1029%2F2008jd010650>, 2009.
- Monteith, J. L.: Solar Radiation and Productivity in Tropical Ecosystems, *Journal of Applied Ecology*, 9, 747–766, <http://www.jstor.org/stable/2401901>, 1972.
- Moors, E.: Water Use of Forests in The Netherlands, Ph.D. thesis, Vrije Universiteit Amsterdam, 2012.
- Myneni, R., Knyazikhin, Y., and Park, T.: MOD15A2H MODIS/Terra Leaf Area Index/FPAR 8-Day L4 Global 500m SIN Grid V006, <https://doi.org/10.5067/MODIS/MOD15A2H.006>, <https://doi.org/10.5067/MODIS/MOD15A2H.006>, distributed by NASA EOSDIS Land Processes DAAC.
- Myneni, R., Knyazikhin, Y., and Park, T.: MOD15A3H MODIS/Combined Terra+Aqua Leaf Area Index/FPAR Daily L4 Global 500m SIN Grid, <http://doi.org/10.5067/MODIS/MOD15A3H.006>, <https://doi.org/10.5067/MODIS/MOD15A3H.006>, 2015.

- 1205 Nakai, T., Kim, Y., Busey, R. C., Suzuki, R., Nagai, S., Kobayashi, H., Park, H., Sugiura, K., and Ito, A.: Characteristics of evapotranspiration from a permafrost black spruce forest in interior Alaska, *Polar Science*, 7, 136–148, <https://doi.org/10.1016/j.polar.2013.03.003>, <https://doi.org/10.1016%2Fj.polar.2013.03.003>, 2013.
- Noormets, A., Chen, J., and Crow, T. R.: Age-Dependent Changes in Ecosystem Carbon Fluxes in Managed Forests in Northern Wisconsin, USA, *Ecosystems*, 10, 187–203, <https://doi.org/10.1007/s10021-007-9018-y>, <https://doi.org/10.1007%2Fs10021-007-9018-y>, 2007.
- 1210 Oquist, G. and Huner, N. P. A.: Photosynthesis of overwintering evergreen plants, *Annu. Rev. Plant Biol.*, 54, 329–355, 2003.
- Papale, D., Migliavacca, M., Cremonese, E., Cescatti, A., Alberti, G., Balzarolo, M., Marchesini, L. B., Canfora, E., Casa, R., Duce, P., Facini, O., Galvagno, M., Genesio, L., Gianelle, D., Magliulo, V., Matteucci, G., Montagnani, L., Petrella, F., Pitacco, A., Seufert, G., Spano, D., Stefani, P., Vaccari, F. P., and Valentini, R.: Carbon, Water and Energy Fluxes of Terrestrial Ecosystems in Italy, in: *The Greenhouse Gas Balance of Italy*, pp. 11–45, Springer Berlin Heidelberg, [https://doi.org/10.1007/978-3-642-32424-6\\_2](https://doi.org/10.1007/978-3-642-32424-6_2), [https://doi.org/10.1007%2F978-3-642-32424-6\\_2](https://doi.org/10.1007%2F978-3-642-32424-6_2), 2014.
- 1215 Pelkonen, P. and Hari, P.: The Dependence of the Springtime Recovery of CO<sub>2</sub> Uptake in Scots Pine on Temperature and Internal Factors, *Flora*, 169, 398–404, 1980.
- Pilegaard, K., Ibrom, A., Courtney, M. S., Hummelshøj, P., and Jensen, N. O.: Increasing net CO<sub>2</sub> uptake by a Danish beech forest during the period from 1996 to 2009, *Agricultural and Forest Meteorology*, 151, 934–946, <https://doi.org/10.1016/j.agrformet.2011.02.013>, <https://doi.org/10.1016%2Fj.agrformet.2011.02.013>, 2011.
- 1220 Porcar-Castell, A., Tyystjärvi, E., Atherton, J., van der Tol, C., Flexas, J., Pfündel, E. E., Moreno, J., Frankenberg, C., and Berry, J. A.: Linking chlorophyll a fluorescence to photosynthesis for remote sensing applications: mechanisms and challenges, *J. Exp. Bot.*, 65, 4065–4095, 2014.
- Posse, G., Lewczuk, N., Richter, K., and Cristiano, P.: Carbon and water vapor balance in a subtropical pine plantation, *iForest - Biogeosciences and Forestry*, 9, 736–742, <https://doi.org/10.3832/for1815-009>, <https://doi.org/10.3832%2Ffor1815-009>, 2016.
- 1225 Post, H., Franssen, H. J. H., Graf, A., Schmidt, M., and Vereecken, H.: Uncertainty analysis of eddy covariance CO<sub>2</sub> flux measurements for different EC tower distances using an extended two-tower approach, *Biogeosciences*, 12, 1205–1221, <https://doi.org/10.5194/bg-12-1205-2015>, <https://doi.org/10.5194%2FBg-12-1205-2015>, 2015.
- Powell, T. L., Bracho, R., Li, J., Dore, S., Hinkle, C. R., and Drake, B. G.: Environmental controls over net ecosystem carbon exchange of scrub oak in central Florida, *Agricultural and Forest Meteorology*, 141, 19–34, <https://doi.org/10.1016/j.agrformet.2006.09.002>, <https://doi.org/10.1016%2Fj.agrformet.2006.09.002>, 2006.
- 1230 Prentice, I. C., Dong, N., Gleason, S. M., Maire, V., and Wright, I. J.: Balancing the costs of carbon gain and water transport: testing a new theoretical framework for plant functional ecology, *Ecology Letters*, 17, 82–91, <https://doi.org/10.1111/ele.12211>, <http://dx.doi.org/10.1111/ele.12211>, 2014.
- 1235 Prentice, I. C., Liang, X., Medlyn, B. E., and Wang, Y.-P.: Reliable, robust and realistic: the three R's of next-generation land-surface modelling, *Atmos. Chem. Phys.*, 15, 5987–6005, 2015.
- Prescher, A.-K., Grünwald, T., and Bernhofer, C.: Land use regulates carbon budgets in eastern Germany: From NEE to NBP, *Agricultural and Forest Meteorology*, 150, 1016–1025, <https://doi.org/10.1016/j.agrformet.2010.03.008>, <https://doi.org/10.1016%2Fj.agrformet.2010.03.008>, 2010.
- 1240 Priestley, C. H. B. and Taylor, R. J.: On the Assessment of Surface Heat Flux and Evaporation Using Large-Scale Parameters, *Mon. Weather Rev.*, 100, 81–92, 1972.

- Prober, S. M., Thiele, K. R., Rundel, P. W., Yates, C. J., Berry, S. L., Byrne, M., Christidis, L., Gosper, C. R., Grierson, P. F., Lemson, K., Lyons, T., Macfarlane, C., O'Connor, M. H., Scott, J. K., Standish, R. J., Stock, W. D., van Etten, E. J., Wardell-Johnson, G. W., and Watson, A.: Facilitating adaptation of biodiversity to climate change: A conceptual framework applied to the world's largest Mediterranean-climate woodland, *Climatic Change*, 110, 227–248, <https://doi.org/10.1007/s10584-011-0092-y>, <http://link.springer.com/10.1007/s10584-011-0092-y>, 2012.
- R Core Team: R: A Language and Environment for Statistical Computing, R Foundation for Statistical Computing, Vienna, Austria, <https://www.R-project.org/>, 2016.
- Rambal, S., Joffre, R., Ourcival, J. M., Cavender-Bares, J., and Rocheteau, A.: The growth respiration component in eddy CO<sub>2</sub> flux from a *Quercus ilex* mediterranean forest, *Global Change Biology*, 10, 1460–1469, <https://doi.org/10.1111/j.1365-2486.2004.00819.x>, <https://doi.org/10.1111%2Fj.1365-2486.2004.00819.x>, 2004.
- Reichstein, M., Falge, E., Baldocchi, D., Papale, D., Aubinet, M., Berbigier, P., Bernhofer, C., Buchmann, N., Gilmanov, T., Granier, A., Grunwald, T., Havrankova, K., Ilvesniemi, H., Janous, D., Knohl, A., Laurila, T., Lohila, A., Loustau, D., Matteucci, G., Meyers, T., Miglietta, F., Ourcival, J.-M., Pumpanen, J., Rambal, S., Rotenberg, E., Sanz, M., Tenhunen, J., Seufert, G., Vaccari, F., Vesala, T., Yakir, D., and Valentini, R.: On the separation of net ecosystem exchange into assimilation and ecosystem respiration: review and improved algorithm, *Glob. Chang. Biol.*, 11, 1424–1439, 2005.
- Reverter, B. R., Sánchez-Cañete, E. P., Resco, V., Serrano-Ortiz, P., Oyonarte, C., and Kowalski, A. S.: Analyzing the major drivers of NEE in a Mediterranean alpine shrubland, *Biogeosciences*, 7, 2601–2611, <https://doi.org/10.5194/bg-7-2601-2010>, <https://doi.org/10.5194%2Fbg-7-2601-2010>, 2010.
- Richardson, A. D., Hollinger, D. Y., Aber, J. D., Ollinger, S. V., and Braswell, B. H.: Environmental variation is directly responsible for short-but not long-term variation in forest-atmosphere carbon exchange, *Global Change Biology*, 13, 788–803, <https://doi.org/10.1111/j.1365-2486.2007.01330.x>, <https://onlinelibrary.wiley.com/doi/abs/10.1111/j.1365-2486.2007.01330.x>, 2007.
- Rogers, A.: The use and misuse of V<sub>c,max</sub> in Earth System Models, *Photosynthesis Research*, 119, 15–29, <https://doi.org/10.1007/s11120-013-9818-1>, <https://doi.org/10.1007/s11120-013-9818-1>, 2014.
- Rogers, A., Medlyn, B. E., Dukes, J. S., Bonan, G., von Caemmerer, S., Dietze, M. C., Kattge, J., Leakey, A. D. B., Mercado, L. M., Niinemets, U., Prentice, I. C., Serbin, S. P., Sitch, S., Way, D. A., and Zaehle, S.: A roadmap for improving the representation of photosynthesis in Earth system models, *New Phytologist*, 213, 22–42, <https://doi.org/10.1111/nph.14283>, <http://dx.doi.org/10.1111/nph.14283>, 2016-22284, 2017.
- Ruehr, N. K., Martin, J. G., and Law, B. E.: Effects of water availability on carbon and water exchange in a young ponderosa pine forest: Above- and belowground responses, *Agricultural and Forest Meteorology*, 164, 136–148, <https://doi.org/10.1016/j.agrformet.2012.05.015>, <https://doi.org/10.1016%2Fj.agrformet.2012.05.015>, 2012.
- Running, S. and Mu, Q. and Zhao, M.: MOD17A2H MODIS/Terra Gross Primary Productivity 8-Day L4 Global 500m SIN Grid V006, <https://doi.org/10.5067/MODIS/MOD17A2H.006>, <https://doi.org/10.5067/MODIS/MOD17A2H.006>, distributed by NASA EOSDIS Land Processes DAAC, 2015.
- Running, S. W., Nemani, R. R., Heinsch, F. A., Zhao, M., Reeves, M., and Hashimoto, H.: A Continuous Satellite-Derived Measure of Global Terrestrial Primary Production, *BioScience*, 54, 547–560, [https://doi.org/10.1641/0006-3568\(2004\)054\[0547:ACSMOG\]2.0.CO;2](https://doi.org/10.1641/0006-3568(2004)054[0547:ACSMOG]2.0.CO;2), [https://doi.org/10.1641/0006-3568\(2004\)054\[0547:ACSMOG\]2.0.CO;2](https://doi.org/10.1641/0006-3568(2004)054[0547:ACSMOG]2.0.CO;2), 2004.
- Ryu, Y., Baldocchi, D. D., Kobayashi, H., van Ingen, C., Li, J., Black, T. A., Beringer, J., van Gorsel, E., Knohl, A., Law, B. E., and Rouspard, O.: Integration of MODIS land and atmosphere products with a coupled-process model to estimate gross primary productivity

- and evapotranspiration from 1 km to global scales, *Global Biogeochemical Cycles*, 25, <https://doi.org/10.1029/2011GB004053>, <https://agupubs.onlinelibrary.wiley.com/doi/abs/10.1029/2011GB004053>, 2011.
- Ryu, Y., Berry, J. A., and Baldocchi, D. D.: What is global photosynthesis? History, uncertainties and opportunities, *Remote Sens. Environ.*, 223, 95–114, 2019.
- Sabbatini, S., Arriga, N., Bertolini, T., Castaldi, S., Chiti, T., Consalvo, C., Djomo, S. N., Gioli, B., Matteucci, G., and Papale, D.: Greenhouse gas balance of cropland conversion to bioenergy poplar short-rotation coppice, *Biogeosciences*, 13, 95–113, <https://doi.org/10.5194/bg-13-95-2016>, <https://doi.org/10.5194%2Fbg-13-95-2016>, 2016.
- Saxton, K. E. and Rawls, W. J.: Soil Water Characteristic Estimates by Texture and Organic Matter for Hydrologic Solutions, *Soil Sci. Soc. Am. J.*, 70, 1569–1578, 2006.
- Schroder, I., Kuske, T., and Zegelin, S.: Eddy Covariance Dataset for Arcturus (2011-2013), Geoscience Australia, Canberra, Tech. rep., <https://doi.org/10.1001/14249>, 2014.
- Scott, R. L., Jenerette, G. D., Potts, D. L., and Huxman, T. E.: Effects of seasonal drought on net carbon dioxide exchange from a woody-plant-encroached semiarid grassland, *Journal of Geophysical Research*, 114, <https://doi.org/10.1029/2008jg000900>, <https://doi.org/10.1029%2F2008jg000900>, 2009.
- Scott, R. L., Hamerlynck, E. P., Jenerette, G. D., Moran, M. S., and Barron-Gafford, G. A.: Carbon dioxide exchange in a semidesert grassland through drought-induced vegetation change, *Journal of Geophysical Research*, 115, <https://doi.org/10.1029/2010jg001348>, <https://doi.org/10.1029%2F2010jg001348>, 2010.
- Scott, R. L., Biederman, J. A., Hamerlynck, E. P., and Barron-Gafford, G. A.: The carbon balance pivot point of southwestern U.S. semiarid ecosystems: Insights from the 21st century drought, *Journal of Geophysical Research: Biogeosciences*, 120, 2612–2624, <https://doi.org/10.1002/2015jg003181>, <https://doi.org/10.1002%2F2015jg003181>, 2015a.
- Scott, R. L., Biederman, J. A., Hamerlynck, E. P., and Barron-Gafford, G. A.: The carbon balance pivot point of southwestern U.S. semiarid ecosystems: Insights from the 21st century drought, *Journal of Geophysical Research: Biogeosciences*, 120, 2612–2624, <https://doi.org/10.1002/2015jg003181>, <https://doi.org/10.1002%2F2015jg003181>, 2015b.
- Serrano-Ortiz, P., Marañón-Jiménez, S., Reverter, B. R., Sánchez-Cañete, E. P., Castro, J., Zamora, R., and Kowalski, A. S.: Post-fire salvage logging reduces carbon sequestration in Mediterranean coniferous forest, *Forest Ecology and Management*, 262, 2287–2296, <https://doi.org/10.1016/j.foreco.2011.08.023>, <http://linkinghub.elsevier.com/retrieve/pii/S0378112711005159>, 2011.
- Shao, C., Chen, J., Li, L., Dong, G., Han, J., Abraha, M., and John, R.: Grazing effects on surface energy fluxes in a desert steppe on the Mongolian Plateau, *Ecological Applications*, 27, 485–502, <https://doi.org/10.1002/eap.1459>, 2017.
- Shi, P., Sun, X., Xu, L., Zhang, X., He, Y., Zhang, D., and Yu, G.: Net ecosystem CO<sub>2</sub> exchange and controlling factors in a steppe—Kobresia meadow on the Tibetan Plateau, *Science in China Series D: Earth Sciences*, 49, 207–218, <https://doi.org/10.1007/s11430-006-8207-4>, <https://doi.org/10.1007%2Fs11430-006-8207-4>, 2006.
- Singsaas, E. L., Ort, D. R., and DeLucia, E. H.: Variation in measured values of photosynthetic quantum yield in ecophysiological studies, *Oecologia*, 128, 15–23, <https://doi.org/10.1007/s004420000624>, <https://doi.org/10.1007/s004420000624>, 2001.
- Smith, E. L.: THE INFLUENCE OF LIGHT AND CARBON DIOXIDE ON PHOTOSYNTHESIS, *J. Gen. Physiol.*, 20, 807–830, 1937.
- Smith, N. G. and Dukes, J. S.: Plant respiration and photosynthesis in global-scale models: incorporating acclimation to temperature and CO<sub>2</sub>, *Glob. Chang. Biol.*, 19, 45–63, 2013.
- Smith, N. G. and Dukes, J. S.: Short-term acclimation to warmer temperatures accelerates leaf carbon exchange processes across plant types, *Glob. Chang. Biol.*, 23, 4840–4853, 2017.

- Smith, N. G., Keenan, T. F., Colin Prentice, I., Wang, H., Wright, I. J., Niinemets, U., Crous, K. Y., Domingues, T. F., Guerrieri, R., Yoko Ishida, F., Kattge, J., Kruger, E. L., Maire, V., Rogers, A., Serbin, S. P., Tarvainen, L., Togashi, H. F., Townsend, P. A., Wang, M., Weerasinghe, L. K., and Zhou, S.-X.: Global photosynthetic capacity is optimized to the environment, *Ecol. Lett.*, 2019.
- 1320 Stevens, R. M., Ewenz, C. M., Grigson, G., and Conner, S. M.: Water use by an irrigated almond orchard, *Irrigation Science*, 30, 189–200, <https://doi.org/10.1007/s00271-011-0270-8>, <https://doi.org/10.1007%2Fs00271-011-0270-8>, 2011.
- Stocker, B.: fLUE, <https://doi.org/10.5281/zenodo.1158524>, <https://doi.org/10.5281/zenodo.1158524>, 2018.
- Stocker, B.: rpmodel: v1.0.4, <https://doi.org/10.5281/zenodo.3560169>, <https://doi.org/10.5281/zenodo.3560169>, 2019a.
- 1325 Stocker, B.: sofun: v1.2.0, <https://doi.org/10.5281/zenodo.3529466>, <https://doi.org/10.5281/zenodo.3529466>, 2019b.
- Stocker, B.: eval\_pmodel, <https://doi.org/10.5281/zenodo.3632308>, <https://doi.org/10.5281/zenodo.3632308>, 2020a.
- Stocker, B.: rsfun, <https://doi.org/10.5281/zenodo.3632328>, <https://doi.org/10.5281/zenodo.3632328>, 2020b.
- Stocker, B. D.: GPP at FLUXNET Tier 1 sites from P-model, <https://doi.org/10.5281/zenodo.3559850>, <https://doi.org/10.5281/zenodo.3559850>, 2019c.
- 1330 Stocker, B. D., Zscheischler, J., Keenan, T. F., Prentice, I. C., Peñuelas, J., and Seneviratne, S. I.: Quantifying soil moisture impacts on light use efficiency across biomes, *New Phytologist*, 218, 1430–1449, 2018.
- Stocker, B. D., Zscheischler, J., Keenan, T. F., Prentice, I. C., Seneviratne, S. I., and Peñuelas, J.: Drought impacts on terrestrial primary production underestimated by satellite monitoring, *Nature Geoscience*, 12, 264–270, <https://doi.org/10.1038/s41561-019-0318-6>, <https://doi.org/10.1038/s41561-019-0318-6>, 2019.
- 1335 Suni, T., Rinne, J., Reissel, A., Altimir, N., Keronen, P., Rannik, Ü., Maso, M., Kulmala, M., and Vesala, T.: Long-term measurements of surface fluxes above a Scots pine forest in Hyytiälä, southern Finland, *Boreal Environ. Res.*, 4, 287–301, 2003.
- Suzuki, Y., Makino, A., and Mae, T.: Changes in the turnover of Rubisco and levels of mRNAs of *rbcL* and *rbcS* in rice leaves from emergence to senescence, *Plant Cell Environ.*, 24, 1353–1360, 2001.
- Tagesson, T., Fensholt, R., Guiro, I., Rasmussen, M. O., Huber, S., Mbow, C., Garcia, M., Horion, S., Sandholt, I., Holm-Rasmussen, B., Göttsche, F. M., Ridler, M.-E., Olén, N., Olsen, J. L., Ehammer, A., Madsen, M., Olesen, F. S., and Ardo, J.: Ecosystem properties of semiarid savanna grassland in West Africa and its relationship with environmental variability, *Global Change Biology*, 21, 250–264, <https://doi.org/10.1111/gcb.12734>, <https://doi.org/10.1111%2Fgcb.12734>, 2014.
- 1340 Tanja, S., Berninger, F., Vesala, T., Markkanen, T., Hari, P., Mäkelä, A., Ilvesniemi, H., Hänninen, H., Nikinmaa, E., Huttula, T., Laurila, T., Aurela, M., Grelle, A., Lindroth, A., Arneth, A., Shibistova, O., and Lloyd, J.: Air temperature triggers the recovery of evergreen boreal forest photosynthesis in spring, *Global Change Biology*, 9, 1410–1426, <https://doi.org/10.1046/j.1365-2486.2003.00597.x>, <https://onlinelibrary.wiley.com/doi/abs/10.1046/j.1365-2486.2003.00597.x>, 2003.
- 1345 Tedeschi, V., Rey, A., Manca, G., Valentini, R., Jarvis, P. G., and Borghetti, M.: Soil respiration in a Mediterranean oak forest at different developmental stages after coppicing, *Global Change Biology*, 12, 110–121, <https://doi.org/10.1111/j.1365-2486.2005.01081.x>, <https://doi.org/10.1111%2Fj.1365-2486.2005.01081.x>, 2006.
- 1350 Tramontana, G., Jung, M., Schwalm, C. R., Ichii, K., Camps-Valls, G., Ráduly, B., Reichstein, M., Arain, M. A., Cescatti, A., Kiely, G., Merbold, L., Serrano-Ortiz, P., Sickert, S., Wolf, S., and Papale, D.: Predicting carbon dioxide and energy fluxes across global FLUXNET sites with regression algorithms, *Biogeosciences*, 13, 4291–4313, <https://doi.org/10.5194/bg-13-4291-2016>, <https://www.biogeosciences.net/13/4291/2016/>, 2016.

- Ulke, A. G., Gattinoni, N. N., and Posse, G.: Analysis and modelling of turbulent fluxes in two different ecosystems in Argentina, International Journal of Environment and Pollution, 58, 52, <https://doi.org/10.1504/ijep.2015.076583>, <https://doi.org/10.1504%2Fijep.2015.076583>, 2015.
- Urbanski, S., Barford, C., Wofsy, S., Kucharik, C., Pyle, E., Budney, J., McKain, K., Fitzjarrald, D., Czikowsky, M., and Munger, J. W.: Factors controlling CO<sub>2</sub> exchange on timescales from hourly to decadal at Harvard Forest, Journal of Geophysical Research, 112, <https://doi.org/10.1029/2006jg000293>, <https://doi.org/10.1029%2F2006jg000293>, 2007a.
- Urbanski, S., Barford, C., Wofsy, S., Kucharik, C., Pyle, E., Budney, J., McKain, K., Fitzjarrald, D., Czikowsky, M., and Munger, J. W.: Factors controlling CO<sub>2</sub> exchange on timescales from hourly to decadal at Harvard Forest, Journal of Geophysical Research: Biogeosciences, 112, <https://doi.org/10.1029/2006JG000293>, <https://agupubs.onlinelibrary.wiley.com/doi/abs/10.1029/2006JG000293>, 2007b.
- Valentini, R., Angelis, P., Matteucci, G., Monaco, R., Dore, S., and Mucnozza, G. E. S.: Seasonal net carbon dioxide exchange of a beech forest with the atmosphere, Global Change Biology, 2, 199–207, <https://doi.org/10.1111/j.1365-2486.1996.tb00072.x>, <https://doi.org/10.1111%2Fj.1365-2486.1996.tb00072.x>, 1996.
- Veres, J. S. and Williams, III, G. J.: Time course of photosynthetic temperature acclimation in *Carex eleocharis* Bailey, Plant Cell Environ., 7, 545–547, 1984.
- Verhoeven, A.: Sustained energy dissipation in winter evergreens, New Phytol., 201, 57–65, 2014.
- von Caemmerer, S. and Farquhar, G. D.: Some relationships between the biochemistry of photosynthesis and the gas exchange of leaves, Planta, 153, 376–387, 1981.
- Wang, H., Prentice, I. C., Keenan, T. F., Davis, T. W., Wright, I. J., Cornwell, W. K., Evans, B. J., and Peng, C.: Towards a universal model for carbon dioxide uptake by plants, Nat Plants, 3, 734–741, 2017a.
- Wang, L., Zhu, H., Lin, A., Zou, L., Qin, W., and Du, Q.: Evaluation of the Latest MODIS GPP Products across Multiple Biomes Using Global Eddy Covariance Flux Data, Remote Sensing, 9, <https://doi.org/10.3390/rs9050418>, <http://www.mdpi.com/2072-4292/9/5/418>, 2017b.
- Way, D. A. and Yamori, W.: Thermal acclimation of photosynthesis: on the importance of adjusting our definitions and accounting for thermal acclimation of respiration, Photosynth. Res., 119, 89–100, 2014.
- Weedon, G. P., Balsamo, G., Bellouin, N., Gomes, S., Best, M. J., and Viterbo, P.: The WFDEI meteorological forcing data set: WATCH Forcing Data methodology applied to ERA-Interim reanalysis data, Water Resour. Res., 50, 7505–7514, 2014.
- Wehr, R., Munger, J. W., McManus, J. B., Nelson, D. D., Zahniser, M. S., Davidson, E. A., Wofsy, S. C., and Saleska, S. R.: Seasonality of temperate forest photosynthesis and daytime respiration, Nature, 534, 680 EP –, <https://doi.org/10.1038/nature17966>, 2016.
- Wen, X. F., Wang, H. M., Wang, J. L., Yu, G. R., and Sun, X. M.: Ecosystem carbon exchanges of a subtropical evergreen coniferous plantation subjected to seasonal drought, 2003–2007, Biogeosciences, 7, 357–369, <https://doi.org/10.5194/bg-7-357-2010>, 2010.
- Wick, B., Veldkamp, E., de Mello, W. Z., Keller, M., and Crill, P.: Nitrous oxide fluxes and nitrogen cycling along a pasture chronosequence in Central Amazonia, Brazil, Biogeosciences, 2, 175–187, <https://doi.org/10.5194/bg-2-175-2005>, <https://doi.org/10.5194%2Fbg-2-175-2005>, 2005.
- Wohlfahrt, G., Hammerle, A., Haslwanter, A., Bahn, M., Tappeiner, U., and Cernusca, A.: Seasonal and inter-annual variability of the net ecosystem CO<sub>2</sub> exchange of a temperate mountain grassland: Effects of weather and management, Journal of Geophysical Research, 113, <https://doi.org/10.1029/2007jd009286>, <https://doi.org/10.1029%2F2007jd009286>, 2008.

- 1390 Yan, J., Zhang, Y., Yu, G., Zhou, G., Zhang, L., Li, K., Tan, Z., and Sha, L.: Seasonal and inter-annual variations in net ecosystem exchange of two old-growth forests in southern China, *Agricultural and Forest Meteorology*, 182-183, 257–265, <https://doi.org/10.1016/j.agrformet.2013.03.002>, <http://linkinghub.elsevier.com/retrieve/pii/S0168192313000567>, 2013.
- Yang Xiang, Gubian, S., Suomela, B., and Hoeng, J.: Generalized Simulated Annealing for Efficient Global Optimization: the GenSA Package for R., *The R Journal* Volume 5/1, June 2013, <http://journal.r-project.org/>, 2013.
- 1395 Yee, M. S., Pauwels, V. R., Daly, E., Beringer, J., Rüdiger, C., McCabe, M. F., and Walker, J. P.: A comparison of optical and microwave scintillometers with eddy covariance derived surface heat fluxes, *Agricultural and Forest Meteorology*, 213, 226–239, <https://doi.org/10.1016/j.agrformet.2015.07.004>, <https://doi.org/10.1016%2Fj.agrformet.2015.07.004>, 2015.
- Zeller, K. and Nikolov, N.: Quantifying simultaneous fluxes of ozone, carbon dioxide and water vapor above a subalpine forest ecosystem, *Environmental Pollution*, 107, 1–20, [https://doi.org/10.1016/s0269-7491\(99\)00156-6](https://doi.org/10.1016/s0269-7491(99)00156-6), <https://doi.org/10.1016%2Fs0269-7491%2899%2900156-6>, 2000.
- 1400 Zeng, Y., Badgley, G., Dechant, B., Ryu, Y., Chen, M., and Berry, J.: A practical approach for estimating the escape ratio of near-infrared solar-induced chlorophyll fluorescence, *Remote Sensing of Environment*, 232, 111 209, <https://doi.org/https://doi.org/10.1016/j.rse.2019.05.028>, <http://www.sciencedirect.com/science/article/pii/S0034425719302226>, 2019.
- Zhang, Y., Xiao, X., Wu, X., Zhou, S., Zhang, G., Qin, Y., and Dong, J.: A global moderate resolution dataset of gross primary production of vegetation for 2000–2016, *Scientific Data*, 4, 170 165, 2017a.
- 1405 Zhang, Y., Xiao, X., Wu, X., Zhou, S., Zhang, G., Qin, Y., and Dong, J.: A global moderate resolution dataset of gross primary production of vegetation for 2000-2016, *Scientific Data*, 4, 170 165 EP –, <https://doi.org/10.1038/sdata.2017.165>, data Descriptor, 2017b.
- Zhao, M., Heinsch, F. A., Nemani, R. R., and Running, S. W.: Improvements of the MODIS terrestrial gross and net primary production global data set, *Remote Sensing of Environment*, 95, 164 – 176, <https://doi.org/https://doi.org/10.1016/j.rse.2004.12.011>, <http://www.sciencedirect.com/science/article/pii/S0034425705000106>, 2005.
- 1410 Zhu, Z., Bi, J., Pan, Y., Ganguly, S., Anav, A., Xu, L., Samanta, A., Piao, S., Nemani, R. R., and Myneni, R. B.: Global Data Sets of Vegetation Leaf Area Index (LAI)3g and Fraction of Photosynthetically Active Radiation (FPAR)3g Derived from Global Inventory Modeling and Mapping Studies (GIMMS) Normalized Difference Vegetation Index (NDVI3g) for the Period 1981 to 2011, *Remote Sensing*, 5, 927–948, <https://doi.org/10.3390/rs5020927>, <https://www.mdpi.com/2072-4292/5/2/927>, 2013.
- 1415 Zielis, S., Etzold, S., Zweifel, R., Eugster, W., Haeni, M., and Buchmann, N.: NEP of a Swiss subalpine forest is significantly driven not only by current but also by previous year's weather, *Biogeosciences*, 11, 1627–1635, <https://doi.org/10.5194/bg-11-1627-2014>, <https://doi.org/10.5194%2Fbg-11-1627-2014>, 2014.